Chapter 1

High-energy Nucleus-Nucleus Collision: An Overview

In this chapter we shall briefly review different aspects of AB collision at high-energy, emphasizing the experimental scenario in particular. The prospect of observing a phase transition from normal nuclear matter to the Quark-gluon Plasma (QGP), where colour degrees of freedom become deconfined, followed by a subsequent freeze out to the final state particles, lies at the heart of the subject. In the beginning, kinematics of two body interaction and some general features of AB interaction have been discussed. A brief outline of nuclear matter under extreme conditions of temperature and pressure in the background of the MIT bag model, follows next. Subsequently, the status of major experiments on high-energy AB interaction has been reviewed to the extent possible. Different signatures, that have been proposed to identify a possible formation of QGP like state, have also been summarized qualitatively in terms of the physics problems associated with each of them. Major experimental observations related to these signatures have also been incorporated. A section has been devoted to review the experimental observations on dynamical fluctuations in the density distribution of produced particles. The chapter ends with a brief and qualitative description of some phenomenological models on particle production in high-energy AB interactions.

1.1 Introduction

A high-energy AB collision is a complicated dynamical process, where in present day experiments, the typical number of nucleons involved is $10^2 - 10^3$, and where the nucleon-nucleon (NN) center of mass energy, denoted by $\sqrt{s_{NN}}$, typically lies within a range of $10^1 - 10^2$ GeV. This particular area of research has already a more than three decade old history behind it. It all started in the early 1970's with an objective to study the shock compression wave in extended nuclear matter at the Lawrence Berkeley Laboratory. At that time the topic could inspire only about 30 odd physicists. Since then this number has grown by a factor $\sim 10^2$ in this particular area of research, and at present high-energy AB interaction deserves the status of a separate subject [1, 2].

The processes through which an AB collision evolves in space-time have till date remained a debatable issue, because everything happens at a typical space-time scale of $\sim$ 10 fm. A nucleus is an extended object, and one can expect that the geometry more specifically the impact parameter of a collision, plays a crucial role in deciding this evolution process. In general it may however be speculated that, depending on the collision energy involved, as the two colliding nuclei meet they would try to stop each other with varying degrees. Because of this stopping, the colliding nucleons suffer substantial loss in their kinetic energies, that gives rise to new degrees of freedom [3]. The constituents of normal nuclear matter, the valence quarks and the wee partons, are compressed very hard. As a result a region of very high-energy / matter density, sometimes called a 'fireball', is formed [4]. Depending on the initial conditions, this fireball may subsequently come to a local thermal and/or a chemical equilibrium. If the energy density and/or the matter density exceeds certain critical values, one expects a transition [5, 6] from the normal nuclear matter to a colour deconfined state containing quarks and gluons moving freely within a region, that is several to many times larger than the confinement of a typical hadron ($\sim$ 1 fm). It is generally believed that a few microseconds after the initial 'big bang', the universe was filled up with such a state of matter. Since the high-energy AB interactions can possibly replicate that state of the universe under controlled conditions of a laboratory, it is tempting to call such AB interactions as 'little bang'. After the initial compression and subsequent equilibration, the fireball probably undergoes an isentropic expansion stage [7], that is accompanied with an obvious loss in the temperature. Ultimately, a freeze out

temperature is reached when another phase transition leads the fireball to fragment into the final state particles, mostly hadrons. As mentioned above, the number of hadrons emanating from a typical AB interaction in present day experiments is $\sim 10^2 - 10^3$ per event. From the debris of hundreds (even thousands on some occasions) of produced particles it is therefore, not a very easy task to trace back the correct signals for any kind of phase transition, that may not or may have taken place during the course of evolution of the collision process. Often the signal is lost into a large number of unwanted background particles and radiation [8].

In this chapter we have briefly reviewed the current scenario of high-energy AB interaction with an emphasis on the experimental aspects of the subject. The natural unit system ($\hbar = c = k_B = 1$) has been used. Chapter I has been organized in the following way. The kinematics pertaining to a two body high-energy interaction and emission of final state particles have been described. Some of the general characteristics of AB interaction along with the effects of collision geometry have been discussed. The transition from normal nuclear matter to a colour unconfined state under extreme conditions of pressure and temperature have been outlined in the framework of the MIT bag model [9]. Within the limited scope of the present thesis, experimental investigations on high-energy AB interaction performed in the recent past have been reviewed. Different signatures proposed to identify the formation of a QGP like state have been qualitatively explained, where mathematical intricacies have been avoided. The present status of experimental observations against each such signature has also been described. As the present thesis primarily deals with nonstatistical fluctuation in the density of produced particles, we have therefore, incorporated a separate section to review the experimental results on this particular topic. Finally, several models of particle production in high-energy AB interactions have also been briefly outlined.

1.2 Kinematics of Two Body Interaction

The collision between two objects (nuclei) may be analyzed either in the target rest frame (equivalent to the laboratory frame for a target fixed in the laboratory), or in the center of mass frame, where total momentum of the colliding objects is equal to zero. Therefore,

at the very beginning it is necessary to identify the kinematic variables relevant to the two body interaction, and also to find out relationships between these variables in both frames of reference mentioned above [1, 10]. Let us consider a collision between two nuclei A and B, respectively, of mass numbers A and B and masses m_1 and m_2. Let us also define a Lorentz invariant (scalar) quantity s one of the Mandelstam variables as,

$$s = (P_1 + P_2)^2 = (P_1 + P_2)^\mu (P_1 + P_2)_\mu,$$

where $P_1(P_2)$ is the four-momentum of A(B) in the laboratory system (ls). They can also be denoted by, $P_1 = (E_1, \mathbf{P_1})$ and $P_2 = (E_2, \mathbf{P_2})$, where $E_1(E_2)$ and $\mathbf{P_1}(\mathbf{P_2})$ are respectively, the energy and ordinary three momentum of A(B). The relativistic energy-momentum relation $E_2^2 = |\mathbf{P_2}|^2 + m_2^2$ holds for B, which one may consider to be the projectile. If A is considered to be the target fixed in the ls, then $\mathbf{P_1} = \mathbf{0}$ and $E_1 = m_1$. Thus, $P_2 = (E_2, \mathbf{P_2})$ and $P_1 = (m_1, \mathbf{0})$. The Mandelstam variable s in ls is therefore,

$$s = (P_1 + P_2)^2 = (E_2 + m_1)^2 - |\mathbf{P_2}|^2 = {m_1}^2 + {m_2}^2 + 2m_1 E_2.$$

Variables in the center of mass system (cms) should be distinguished from those in the ls. This is done by using an extra superscript c with each variable. According to the definition of the cms $\mathbf{P_1^c} + \mathbf{P_2^c} = \mathbf{0}$. Hence, $-\mathbf{P_1^c} = \mathbf{P_2^c} = \mathbf{P^c}$ say. The corresponding energy values for A and B are given, respectively by,

$$E_1^c = \sqrt{|\mathbf{P^c}|^2 + m_1^2} \text{ and } E_2^c = \sqrt{|\mathbf{P^c}|^2 + m_2^2}.$$

The individual four-momentum, respectively for A and B are therefore, ${P_1}^c = (E_1^c, -\mathbf{P^c})$ and $P_2^c = (E_2^c, \mathbf{P^c})$. Once again the Mandelstam variable s in the cms will be,

$$s = (P_1^c + P_2^c)^2 = (E_1^c + E_2^c)^2 = (E^{cm})^2, \text{ say.}$$

The total cms energy E^{cm} is thus related to s as, $\sqrt{s} = E^{cm}$. Since s is a Lorentz invariant quantity, ${m_1}^2 + {m_2}^2 + 2m_1 E_2 = (E^{cm})^2$, and at relativistic energies where $E_2 >> m_1, m_2$,

$$E^{cm} \approx \sqrt{2m_1 E_2}.$$

The cms velocity $\beta_{cm} = |\mathbf{P_1} + \mathbf{P_2}|/(E_1 + E_2)$ in the ls can be obtained by using the Lorentz transformation relations. $\mathbf{P_1} = \mathbf{0}$ for a target (A) fixed in the ls, and $\beta_{cm} = |\mathbf{P_2}|/(E_1 + E_2)$. The corresponding Lorentz factor is,

$$\gamma_{cm} = \frac{1}{\sqrt{1 - \beta_{cm}^2}} = \frac{E_1 + E_2}{\sqrt{s}}.$$

Consider now that, a particle of rest mass m is produced in the collision between A and B and it comes out with a four-momentum $p(E, \mathbf{p})$, making an angle θ in the ls with respect to the beam (B) direction. In the *cms* let the corresponding four-momentum be $p^c(E^c, \mathbf{p}^c)$, while the angle of emission is denoted by θ^c. If the longitudinal and the transverse components of the momentum of the particle are denoted respectively, by (p_l, p_t) in the ls, and by (p_l^c, p_t^c) in the *cms*, then once again through Lorentz transformation the following relations can be obtained,

$$p_l^c = \gamma_{cm}(p_l - \beta_{cm} E), \quad E^c = \gamma_{cm}(E - \beta_{cm} p_l),$$
$$p_t = \mathbf{p}\sin\theta = p_t^c = \mathbf{p}^c \sin\theta^c, \quad p_l = \mathbf{p}\cos\theta = \gamma_{cm}\,(\beta_{cm} E^c + p_l^c),$$
$$\text{and } E = \gamma_{cm}\,(E^c + \beta_{cm}\, p_l^c) = \gamma_{cm}\,(E^c + \beta_{cm}\, \mathbf{p}^c \cos\theta^c).$$

The transverse mass of the particle is defined as, $m_t = \sqrt{m^2 + p_t^2}$. In most cases the *cms* is a better choice than the ls to study a two body interaction. Of all reference frames it is the *cms* where the energy available is at its minimum value, and therefore, it can provide the threshold value of production of particle(s). Moreover, as in the *cms* the total momentum of colliding objects is zero, unlike the ls in this frame there is no preferential direction of particle emission other than those imposed by the kinematic conditions. If now any preferential emission pattern is observed in the *cms*, then it must be due to some underlying dynamics. To describe the kinematic conditions of a particle produced in a high-energy interaction, we need suitable variables. Components of the four-momentum $p^\mu = (p^0, p^1, p^2, p^3)$ can serve the purpose. These components are constrained by the relativistic energy-momentum relation, that reduces the number of independent variables from four to three. However, as it is often necessary to compare results in different frames of references, one must always keep track of the proper transformation relations between them. If in a reaction many particles are produced, then one often is actually concerned with the distribution of these particles in terms of one or more variables. Under such a situation it would be convenient to choose the kinematic variables in such a way, that the overall shape of the distribution function remains unchanged as one moves from one frame to the other. The rapidity (y) of a particle, a parameter of finite special Lorentz transformation (also called the Lorentz boost), can be defined in several ways e.g,

$$\text{space-time:} \quad \tanh y = \beta, \quad y = \frac{1}{2}\ln\left(\frac{1+\beta}{1-\beta}\right), \tag{1.1}$$

energy-momentum: $p_l = m_t \sinh y, \quad E = m_t \cosh y, \quad y = \frac{1}{2} \ln \left(\frac{E + p_l}{E - p_l} \right).$ (1.2)

Rapidity is a dimensionless quantity and is related to the longitudinal motion (along the beam axis) of the particle. As one can see from the above relations, at $\beta << 1$ the rapidity of a particle traveling in the longitudinal direction is almost equal to the velocity of the particle. Recall that the total energy in the *cms* is $\sqrt{s}$. The energy and momentum of the *cms* in the *ls* are given, respectively by, $\gamma_{cm} \sqrt{s}$ and $\beta_{cm} \gamma_{cm} \sqrt{s}$. The rapidity of the *cms* in the *ls* is therefore,

$$y_{cm} = \frac{1}{2} \ln \frac{\gamma_{cm} \sqrt{s} + \beta_{cm} \gamma_{cm} \sqrt{s}}{\gamma_{cm} \sqrt{s} - \beta_{cm} \gamma_{cm} \sqrt{s}} = \frac{1}{2} \ln \frac{1 + \beta_{cm}}{1 - \beta_{cm}}. \tag{1.3}$$

The rapidity of a particle in the *cms* is denoted by y^c,

$$y^c = \frac{1}{2} \ln \left(\frac{E^c + p_l^c}{E^c - p_l^c} \right). \tag{1.4}$$

Through Lorentz transformation one can see that,

$$y = \frac{1}{2} \ln \frac{\gamma_{cm}(E^c + \beta_{cm} p_l^c) + \gamma_{cm} (\beta_{cm} E^c + p_c^l)}{\gamma_{cm} (E^c + \beta_{cm} p_l^c) - \gamma_{cm} (\beta_{cm} E^c + p_l^c)}$$

$$y = \frac{1}{2} \ln \frac{E^c + p_l^c}{E^c - p_l^c} + \frac{1}{2} \ln \frac{1 + \beta_{cm}}{1 - \beta_{cm}}$$

Thus under the Lorentz boost one gets a simple additive relation between the rapidities in the *ls* and in the *cms*,

$$y = y^c + y_{cm}. \tag{1.5}$$

This simple additive property of the rapidity variable is of utmost importance, because in both frames the shape of the rapidity distribution remains unaltered in either of the frames. To determine the rapidity of a particle, actually two variables E and $\mathbf{p}$ have to be measured. In some experiments only the angle of emission (θ) of the particle with respect to the beam axis can be measured. In such cases the pseudorapidity (η) variable defined by,

$$\eta = -\ln \left[\tan \left(\frac{\theta}{2} \right) \right] \tag{1.6}$$

is used. At high-energies where $p >> m$ one can see that,

$$y = \frac{1}{2} \ln \left(\frac{E + p_l}{E - p_l} \right) = \frac{1}{2} \ln \left(\frac{\sqrt{p^2 + m^2} + p_l}{\sqrt{p^2 + m^2} - p_l} \right)$$

$$\Longrightarrow y \approx \frac{1}{2}\ln\left(\frac{p+p_l}{p-p_l}\right) = \frac{1}{2}\ln\left(\frac{1+\cos\theta}{1-\cos\theta}\right)$$
$$y \approx -\ln\left[\tan\left(\frac{\theta}{2}\right)\right] = \eta.$$

Pseudorapidity is a very convenient variable because, there is no need to measure the momentum of a particle and therefore, no need to apply a magnetic field. Using the exact relations between y and η it can be shown that, in terms of these two variables the normalized number densities of a particular type of particle (of rest mass m say) are related to each other,

$$\frac{dn}{dy\,dp_t} = \sqrt{1-\frac{m^2}{m_t^2\cosh^2 y}}\,\frac{dn}{d\eta\,dp_t}. \tag{1.7}$$

Any discrepancy in the magnitudes of the density (due to the factor within square root) is insignificant for most of the particles produced in high-energy interactions. The differential cross section for particle production expressed in the form of

$$\frac{d^3\sigma}{dp_x\,dp_y\,dp_z}$$

is not invariant under Lorentz boost. If the longitudinal direction is chosen to coincide with the $z-$direction, then $p_z = m_t \sinh y$ and $dp_z = m_t \cosh y\, dy$. Therefore, $dp_z/E = dy$, which is invariant under Lorentz boost, and one may define the invariant cross section as,

$$E\frac{d^3\sigma}{d^3p} = \frac{d^3\sigma}{dp_x\,dp_y\,dy}.$$

Using, $p_t = \sqrt{p_x^2+p_y^2}$, and $\tan\varphi = p_y/p_x$ the invariant cross section can also be expressed as,

$$E\frac{d^3\sigma}{d^3p} = \frac{d^3\sigma}{p_t\,dp_t\,d\varphi\,dy}.$$

1.3 General Characteristics of AB Interaction

Consider a two body reaction like: $A + B \rightarrow X+$ anything,
where X belongs to a definite species of particles. If one is interested to investigate the issues related only to the production of X, then it is called an inclusive analysis. On the other hand, in a high-energy interaction, e.g, nucleus-nucleus (AB) interaction, one may have different types of particles in the final state e.g, fragments of the incident nucleus (projectile), fragments of the target nucleus, and newly produced particles most of which are different types of mesons. Such a reaction can be expressed as,

Projectile + Target→Fragments of the colliding nuclei + Produced particles.

If without making any distinction among its different constituent species, we concentrate our study to one particular category of particles then the analysis is semi-inclusive in nature. It is to be understood that, each category e.g, the category of produced particles can be further subdivided like, the neutral, positive and negative π-mesons, strange mesons, leptons, photons etc. The number of particles in each category is called the multiplicity of that particular category of particles.

1.3.1 Centrality of Collisions

At high-energy two colliding nuclei look like two Lorentz contracted discs/pancakes in their *cms*, the contraction being along the direction of motion of each nucleus [10]. If the impact parameter (b) of collision is as large as the sum of the radii of two nuclei involved, then such a collision is called an extreme peripheral collision. There will hardly be any nuclear interaction, and the interaction between the two nuclei will predominantly be electromagnetic in nature. Either or both of the nuclei will absorb energy through giant resonances, proton-neutron clusters, $\Delta(1231)$ resonances, higher lying nucleon resonances or through decay by emission of one or more nucleons. Only a small fraction of the total number of nucleons belonging to each nuclei are actually affected in peripheral interactions, while most other remain as spectators. On the other hand, if the nuclei experience a head on collision with an impact parameter $b \approx 0$, then the collision is called a central collision. In such a situation the smaller nucleus actually makes a cylindrical hole into the larger nucleus, and in principle all nucleons of the smaller nucleus and most nucleons of the larger nucleus participate in the reaction. Thus one can see that the range over which b can vary is $0 \leq b \leq (R_1 + R_2)$, where R_1 and R_2 are the radii of two nuclei, and the total geometrical cross-section is given by $\sigma_g = \pi r_0^2 (A^{1/3} + B^{1/3})^2$.

Based on the fact that the number of nucleons actually participating in an interaction depends on the impact parameter, the centrality of a collision is determined following certain assumptions. They are, (i) on an average the energy released in a collision is proportional to the number of participating nucleons, (ii) the average multiplicity of particles produced is proportional to the number of participating nucleons, and (iii) average number of produced particles is proportional to the energy released, and hence proportional to

the impact parameter of the collision. The impact parameter/ the centrality of a nuclear collision however, can be and has been decided from other considerations as well. The energy flow in the forward direction is denoted by E_{ZD} and is often measured by setting a zero degree calorimeter (ZDC). The net charge flow within the extreme forward cone is denoted by Q_{ZD}. Both these quantities can serve the purpose of measuring the centrality of a collision [11]. As the impact parameter decreases, the magnitude of E_{ZD} or Q_{ZD} will be smaller. Correspondingly, the transverse energy E_t defined by,

$$E_t = \sum_{i=1}^{n} E_i \sin\theta_i$$

will be larger in central than in the peripheral collisions. Here n is the number of particles produced in an event, and E_i, θ_i are respectively, the energy and emission angle associated with the ith particle. E_t is a suitable measure of the energy available in the *cms* for production of particles, which increases with increasing centrality of the collision. Therefore, E_t can also be used to determine the centrality of a collision. In chapter two, we shall try to illustrate the issues related to AB collision discussed in this section in detail specifically in terms of nuclear emulsion experiments.

1.3.2 p_t Distribution of Produced Particles

As the nucleons belonging to the two colliding nuclei stop each other they loose substantial fraction of their kinetic energies, creating a central fireball stationary at the *cms* of the colliding nuclei, that subsequently cools down to fragment into new final state particles, most of which ($\sim 80-90\%$) are pions. In the *cms* there should not be any preferential direction of emission of the final state particles, except those restricted by the kinematic conditions, and unless there is some dynamics involved in the particle production process. Any new degree of freedom like for example, the transverse momentum component is therefore, a result of the thermodynamic characteristics of the central fireball. With decreasing impact parameter the longitudinal energy is increasingly converted into transverse energy radiated in a direction transverse to the beam direction in the form of produced particles and their kinetic energies. Hence the p_t or E_t distribution of produced particles belonging to different species from the AB collisions may provide important and useful information, that is necessary for to identify the thermodynamical state of the source from which they

are coming out, particularly so because of a possible phase transition from normal nuclear matter to the QGP [10].

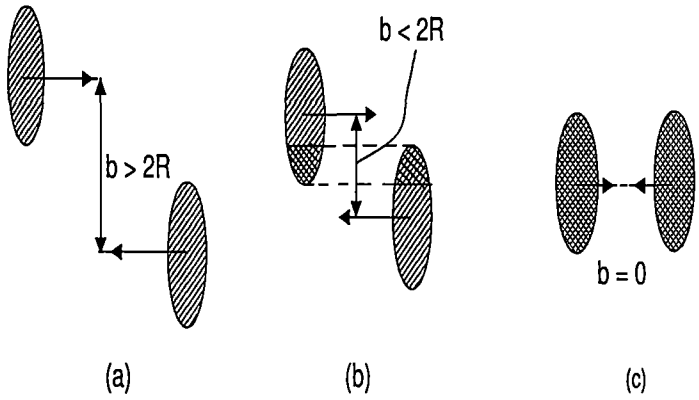

Figure 1.1: The geometry of an AB interaction between two nuclei of same size: (a) extreme peripheral, (b) semi-central and (c) extreme central collision.

The average transverse momentum $< p_t >$ is taken as a measure of the temperature, whereas, the charge particle multiplicity density either globally or restricted to a limited rapidity interval is taken as a measure of entropy and/or energy density. While for most of the pions the $< p_t > \approx 0.35$ GeV/c, in some high-energy cosmic ray interactions and in various high-energy AB interactions carried out in laboratories, it has been found that on some occassions $< p_t >$ is significantly larger than its average value 0.35 GeV/c. $< p_t >$ may be plotted against the energy density ϵ, or the partcle density which is also a measure of entropy density $\left(s_e = A_{part}^{-2/3}\, dn/dy\right)$. If it is observed that after a monotonic rise there is a plateau and again there is sharp increase in the $< p_t >$ value, then the behaviour can be related to some kind of phase transition. It may be speculated that, perhaps the rapid increase of $< p_t >$ after the plateau is due to the formation of QGP and the plateau region indicates the possible phase transition from QGP to normal nuclear matter.

1.3.3 Central and Fragmentation Regions

From simple geometrical considerations it is also possible to estimate the average number of binary collisions (inelastic collisions between two nucleons one each from the A and B),

and the number of participating nucleons in each of the projectile and target nuclei [12]. These numbers are given by,

Average projectile participants $\langle P_B \rangle = B\,\sigma_{pA}/\sigma_{AB}$,
Average target participants $\langle P_A \rangle = A\,\sigma_{pB}/\sigma_{AB}$,
and the average number of binary collisions $\langle N_{BC} \rangle = AB\,\sigma_{pp}/\sigma_{AB}$,

where σ_{pp} is the proton-proton (pp), σ_{pA}, σ_{pB} are the respective proton-nucleus, and σ_{AB} is the AB cross-sections. One can see that the average numbers of participating nucleons for one nucleus can be obtained by taking the ratio of the geometrical cross-section of the other nucleus and σ_g. Therefore, the average number of participating protons for A is,

$$\langle Z_A^{part} \rangle \approx Z_A \frac{\pi r_0^2\, B^{2/3}}{\sigma_g} = \frac{Z_A\, B^{2/3}}{(A^{1/3} + B^{1/3})^2},$$

whereas, the average number of spectator protons in A is,

$$\langle Z_A^{spec} \rangle = Z_A - \langle Z_A^{part} \rangle \approx \frac{Z_A\,(A^{2/3} + 2A^{1/3}\,B^{1/3})}{(A^{1/3} + B^{1/3})^2},$$

with similar expressions for $\langle Z_B^{part} \rangle$ and $\langle Z_B^{spec} \rangle$. The total number of participating protons will therefore be,

$$\langle Z^{part} \rangle = \langle Z_A^{part} \rangle + \langle Z_B^{part} \rangle \approx \frac{Z_A\, B^{2/3} + Z_B\, A^{2/3}}{(A^{1/3} + B^{1/3})^2}.$$

As the two nuclei collide with each other, the incoming nucleons loose their kinetic energies through binary collisions, and new degrees of freedom evolve. The amount of energy lost during such collisions depends on the thickness of the nuclei, and on the collision energy. The degree of energy lost is called the nuclear stopping power. The nuclear stopping results in a shift in the rapidity values of incoming nucleons toward the central or mid-rapidity region. Thus rapidity distribution provides key information regarding the extent of nuclear stopping. At an incident energy of $\sim$ a few tens of GeV/nucleon (typical of BNL AGS), there would be sufficient stopping between the two colliding nuclei, and the central region will be rich in its net baryon content. If a produced particle belongs to the kinematic region, where the target nucleus was initially at rest then it is said to be in the target fragmentation region. Similarly if the produced particle belongs to the kinematic region near that of the projectile, then the particle is said to belong to the projectile fragmentation region. At sufficiently high-energy there is a saturation in the

nuclear stopping, and to a great extent the colliding nuclei are transparent to each other. The two fragmentation regions are then well separated, leaving in between a very hot and dense central region, that is high in energy density and low in its net baryon content. In any high-energy interaction most of the particles produced belong to the central region.

1.3.4 Coherent and Incoherent Collisions

It is difficult to decide whether in an AB interaction each of the colliding nuclei interact as a whole, or the AB collision can be treated as a superposition of a series of independent nucleon-nucleon (NN) collisions [10]. If the two nuclei interact as a whole and there is a collective effect, then the collision is said to be coherent. On the other hand, if the AB collision is a superposition of many independent NN collisions then the collision is said to be incoherent. The total *cms* energy for a coherent collision is not same as that for an incoherent collision. It is therefore, important to find out the degree of coherence, because the way the interaction evolves, depends on the total energy available in the *cms*. Once again in the next chapter we shall see, how the total *cms* energy varies if the events under consideration are assumed to be coherent or incoherent collisions. There are certain theoretical models based on the assumption that the AB collisions are coherent, and there are also models that consider the AB interaction as a combination of series of independent NN interactions. The models based on coherent type of collisions make use of thermodynamics to determine how quantities like energy and temperature are exchanged. They also use hydrodynamics to decide the mechanical compression and expansion of the nuclear matter. The energy density of the hot hadronic matter produced in the central region can be estimated only by assuming that the AB collisions are coherent. Whereas, models based on incoherent type of collisions assume that, through the course of interaction two nucleons are excited, and the excited nucleons exchange a string of quark-antiquark pair, from which hadrons originate.

1.4 AB Interaction and the QGP

The density of normal nuclear matter is, $\rho_0 = \frac{A}{\frac{4}{3}\pi R^3}$ nucleons, where A is the mass number, $R = r_o A^{1/3}$ is the radius of the nucleus, and $r_0 \approx 1.1$ fm is the nuclear radius parameter.

Thus $\rho_0 \approx 0.15$ nucleons/fm^3. The corresponding energy density is,

$$\epsilon_0 \approx 0.15 \times 940\,\text{MeV/fm}^3 \approx 0.14\,\text{GeV/fm}^3.$$

Often the temperature is expressed in units of MeV, the relationship being given by the Boltzmann constant ($k_B = 8.6173 \times 10^{-14}$ GeV/K). Thus, in natural unit system, where $k_B = 1$,

$$1\,\text{GeV} \approx 1.16 \times 10^{13}\,\text{K}.$$

Similarly the time required to travel a distance of 1 fm at the speed of light is often referred to as 1 fm ($\approx 3.3 \times 10^{-24}$ sec).

An important property of the QCD is its large coupling constant at low temperature, which is a result of chiral symmetry breaking, first recognized by Nambu and Jona-Lasinio [13]. Due to this, quarks, antiquarks and gluons are confined inside a nucleon. If the QCD vacuum is heated, then at comparatively lower temperatures new colour neutral hadrons like pions, kaons etc., are thermally excited. As the temperature is further raised, at a certain critical temperature T_c the hadronic matter may start to dissolve or melt down from the individual hadrons into a system of unconfined quarks, antiquarks and gluons filling up a volume, that is several to many units of the characteristic length scale of the hadrons. It is expected that the quarks and antiquarks are excited with equal probability. Therefore, such a state of colour deconfined (gluonic) plasma will be less in its net baryon content. Different model calculations and Monte Carlo lattice QCD simulation indicates that $T_c \geq 150 \sim 200$ MeV. On the other hand, if a large number of baryons are subjected to an extremely high pressure, they can be isothermally compressed to such an extent that, the baryons start to overlap and attain a critical baryon density $\rho_c \approx (5-10)\rho_0$. Under such a situation, one may also expect that the system of baryons will dissolve into a state of deconfined quark matter, which unlike the previous case is rich in its net baryon content. Thus one can see that a new state of coloured plasma consisting of free (weakly coupled) quarks, antiquarks and gluons, called the Quark-gluon plasma (QGP) can be created under a high temperature and/or high pressure situation [15]. One can look for such a state of matter in three possible places.

(i) The entire universe was probably filled up with the QGP just a few to several microseconds after its birth. The universe might have undergone a QCD phase transition at $T = 150 - 200$ MeV at a time scale $\sim 10^{-5}$ sec or so after the big bang.

(ii) At the core of very dense compact stars such as the neutron stars or the strange (quark) stars such a state of matter can be found. If the central density of these compact stars is $> (5-10)\rho_0$, then there is a fair possibility that their constituent hadrons will melt into cold quark matter.

(iii) And lastly, the QGP can possibly be created in laboratory by allowing two heavy nuclei to collide with each other at an extremely high-energy [5], which one may be tempted to call "a little bang".

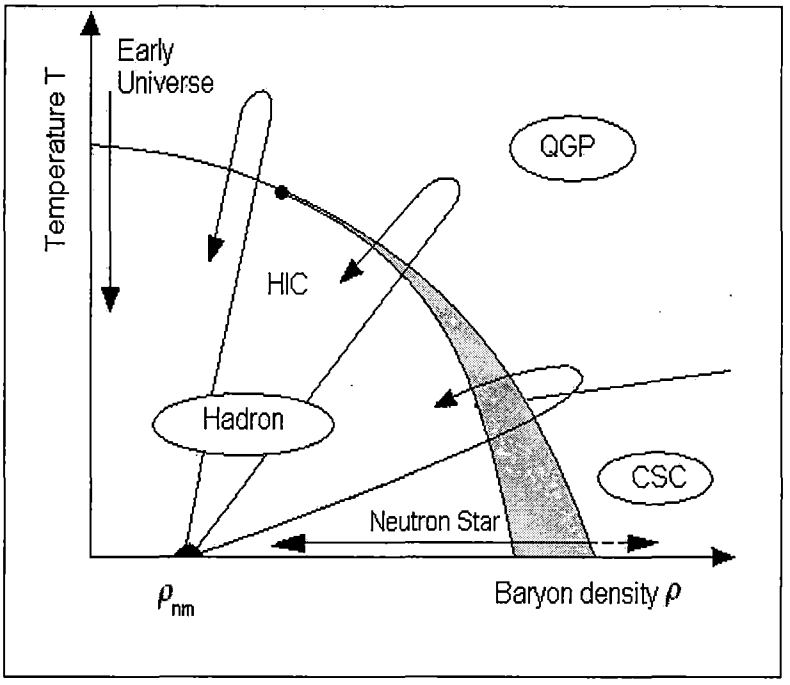

Figure 1.2: Phase diagram showing the hadronic, QGP and colour superconducting (CSC) phases. ρ_{nm} denotes the density of normal nuclear matter. QGP can be created in heavy-ion collisions (HIC).

As mentioned earlier at an incident energy of a few hundred GeV/nucleon one may expect a hot central region of high-energy density filled up predominantly with gluonic plasma, low in net baryon content. Whereas, at a few tens of GeV/nucleon incident energy one expects a high baryon density, high-energy density central region [14]. To produce a well thermalized state of QGP in the laboratory, high-energy collisions between two heavy nuclei have certain advantages over the ordinary hadron-hadron (hh), NN or pA collisions

due to the following reasons:

(i) The average multiplicity of produced particles in high-energy AB collision is larger; hence high-energy density results on the average.

(ii) Larger spatial size of the nuclei enables the produced particles to rescatter several times before being emitted from the collision region. This may allow enough time for thermal and chemical equilibrium to be established in the central region.

(iii) For higher multiplicties statistical fluctuations are smaller and collective phenomena will be easier to observe.

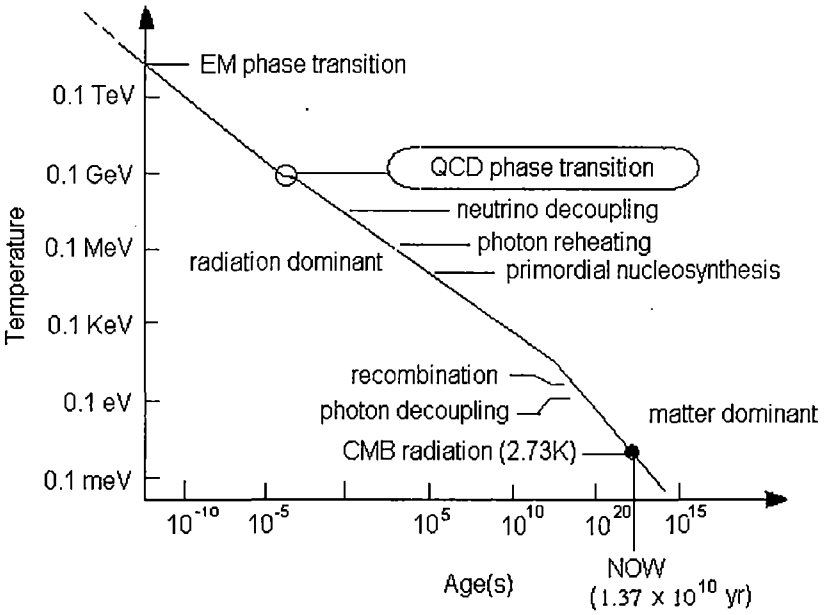

Figure 1.3: Evolution of the universe since electro-weak phase transition. Note the QCD phase transition occurring at a temperature of $\sim 10^2$ MeV.

The exact space-time evolution of a high-energy AB collision is still in a speculative stage. One possible way of looking into the process may be summarized in the following manner. The initial conditions immediately after the first instant of nuclear contact is not precisely known. The colour glass condensate, a coherent, highly excited gluonic configuration, can be a possible candidate for this stage but not the only one. Through frequent interactions among the constituent partons and their rescattering, the excited qunata materialize into new particles. The system evolves through a pre-equilibrium stage to a thermalized era

of QGP. The locally thermalized plasma is treated as a perfect fluid (no viscosity, no thermal conductivity), and the system expands isentropically according to the laws of relativistic hydrodynamics. Eventually it undergoes a chemical and thermal freeze-out producing the final state particles such as, colour neutral hadrons, leptons, photons etc. If we want to know the exact evolution process, then it is necessary to define a few initial parameters such as the initial energy density, thermalization time and freeze-out temperature. Then by solving the hydrodynamical equations it may be possible to relate those initial conditions to the experimentally observed final state particles.

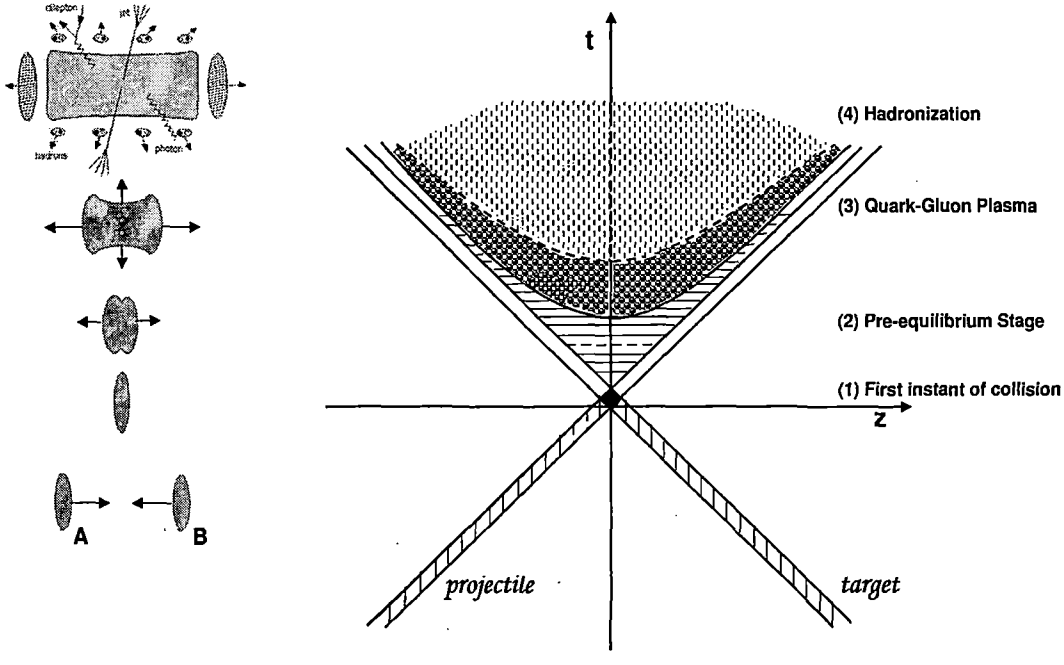

Figure 1.4: A speculative diagram of the space-time evolution of high-energy collision between two nuclei. On the left two Lorentz contracted nuclei meet, collide and then recede from each other leaving a central particle producing region in between. On the right notice the forward and backward light cones and different stages of the evolution.

1.4.1 Landau's Hydrodynamical Picture

As mentioned above, in high-energy AB collisions the baryonic matter is slowed down and looses a large fraction of its initial energy during the collision process. This energy is

deposited around the vicinity of the center of mass of the colliding objects. Considering simple picture of a head-on central collision (zero impact parameter) between two nuclei of equal mass number (say A) in Landau picture [16], where both the nuclei stop each other in the *cms* and as a result loose all their kinetic energies. The resulting energy density at and around the center of mass at the time of collision may be estimated. As discussed above the total energy in the *cms*

$$E^{cm} = \sqrt{s} = 2A\, m_N\, \gamma_{cm},$$

where m_N is the rest mass of individual nucleons. The initial energy density will therefore be,

$$\epsilon = \frac{\sqrt{s}}{V} = \frac{2A\, m_N\, \gamma_{cm}}{V_0/\gamma_{cm}} = 2\epsilon_0\, \gamma_{cm}^2,$$

where V_0 is the volume of the nucleus at rest, and $\epsilon_0 \approx 0.15$ GeV/fm^3 is the energy density of normal nuclear matter. Similarly, the initial baryon number density is,

$$\rho = \frac{2A}{V} = 2\rho_0\, \gamma_{cm},$$

where $\rho_0 \approx 0.16$/fm^3 is the baryon density of normal nuclear matter. Landau and Belensky treated the intermediate expanding state of the matter as a perfect fluid, and applied relativistic hydrodynamics to estimate the initial (shortly after the impact) entropy density (s_e) and the temperature (T) as,

$$s_e \propto \epsilon^{3/4}, \text{ and } T_e \propto \epsilon^{1/4}.$$

Since initial energy density $\epsilon \propto \gamma_{cm}^2 \propto (E^{cm})^2$, the initial entropy density is,

$$s_e \propto \epsilon^{3/4} \propto (E^{cm})^{3/2}.$$

Due to the perfect fluid assumption made by Landau and Belensky, total entropy of the system (S_e) remains constant during hydrodynamical expansion stage, and since the number density of produced pions is proportional to s_e, one can estimate the total number of pions as,

$$N_\pi \propto s_e V \propto (E^{cm})^{3/2} V_0/\gamma_{cm} \propto A\,(E^{cm})^{1/2} \propto A\, E^{1/4},$$

where E is the laboratory energy. Two points can be noted from the hydrodynamical calculation of Landau, (i) one is that, the number of pions scale with the mass number

of the nuclei; hence in comparison with NN interaction in AB interactions more particles result in the final state, and (ii) at ultra-relativistic energies (SPS or RHIC) total stopping of the two colliding nuclei is too unrealistic, and hence untenable.

1.4.2 Bjorken's Estimation of Energy Density

Once again let us consider a head-on collision between two nuclei at ultra-relativistic energy in their *cms*, where each experiences substantial Lorentz contraction. The energy is so high that the longitudinal thickness of each nucleus can be neglected, and to a great extent the nuclei are transparent to each other. It may be assumed that the two nuclei are coming respectively, from $z = +\infty$ and $z = -\infty$, and they meet at $z = 0$ at time $t = 0$. Due to transparency, after the colliding nuclei recede from each other, leaving a region with high-energy density and low net baryon content around $z \sim 0$, which one may call to be the reaction volume. According to Bjorken [17], thereafter, the space-time evolution of the reaction volume is guided by the laws of hydrodynamics. In the first approximation the reaction volume experiences strong expansion in the longitudinal (say z) direction, and one may drop the transverse dimensions to treat the problem in $(1 + 1)$ dimension. Let us recall the definition of the rapidity variable, that allows us to determine the longitudinal velocity near the origin $(z \approx 0, t \approx 0)$ as, $\beta_z = z/t = \tanh y$. The space-time rapidity defined by,

$$z = \tau \sinh y,\ t = \tau \cosh y,\ y = \frac{1}{2} \ln \frac{t+z}{t-z}$$

are now useful. Here τ is the proper time ($\tau = \sqrt{t^2 - z^2}$). Consider a longitudinal length of thickness Δz at $z = 0$ and let the transverse overlapping area of the two colliding nuclei be $\mathcal{A}$. The volume of our interest is therefore, $\mathcal{A}\Delta z$. Fixing our attention to the proper time τ_0 at which the QGP may have been formed and equilibrated, the number density of hadrons produced within the considered volume at $z = 0$ and $\tau = \tau_0$ is,

$$\frac{\Delta n}{\mathcal{A}\,\Delta z} = \frac{1}{\mathcal{A}} \frac{dn}{dy} \frac{dy}{dz}\bigg|_{y=0}.$$

The corresponding energy density at $t = 0$ is therefore,

$$\epsilon = m_t \cosh y \frac{\Delta n}{\mathcal{A}\,\Delta z}.$$

Averaging over the transverse area $\mathcal{A}$ at proper time τ_0 one gets,

$$\epsilon = \frac{m_t}{\tau_0 \mathcal{A}} \left.\frac{dn}{dy}\right|_{y=0} \approx \frac{m_t}{\tau_0 \mathcal{A}} \left.\frac{dn}{d\eta}\right|_{\eta=0},$$

which is the well known Bjorken's estimation of the energy density.

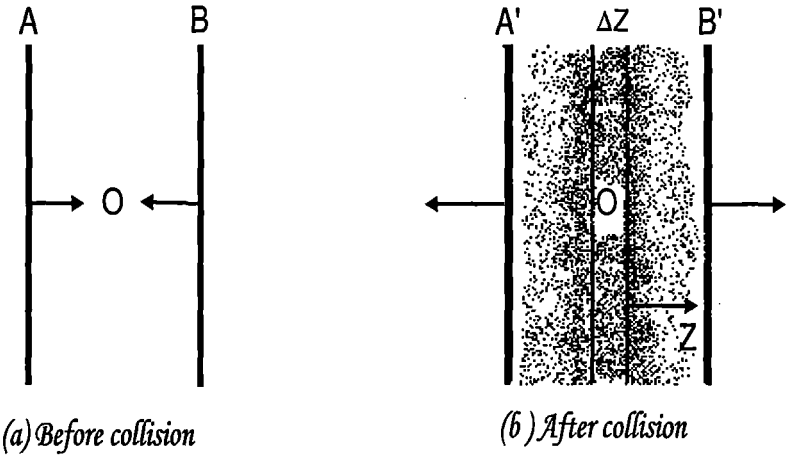

Figure 1.5: Bjorken's estimation of energy density in the central rapidity region.

1.4.3 Deconfinement and the Bag Model

Due to the asymptotic nature of the force that binds the quarks and antiquarks (if any) inside a hadron, it is impossible for the quarks or antiquarks to break free and exist independently. Quarks, gluons and antiquarks are always confined within the hadrons. Values of parameters like the pressure, energy density, temperature etc. at which one may expect a deconfined state like the QGP, may be obtained from different theoretical considerations, one of which is the MIT bag model. The method of calculation within the frame work of this model has been outlined in [1], short summary of which is also presented here. In the MIT bag model the quarks are treated as massless, non-interacting fermions inside a bag of finite dimension, and they are infinitely massive outside the bag. Confinement in this model is a result of the balance between a bag pressure B directed inwards, and an outward stress arising from the kinetic energy of the quarks. Quarks and gluons are confined within the bag, and the total colour charge contained inside the bag

is zero. An estimation of the bag pressure can be made with the help of Dirac equation for massless non-interacting fermions in a spherical cavity of radius R,

$$\gamma^{\mu} p_{\mu} \psi = 0,$$

where ψ is a four component spinor. Confinement of quarks within the bag is described in terms of a vector current, $J_{\mu} = \bar{\psi}\gamma_{\mu}\psi$ the normal component of which vanishes at the bag surface. This condition is same as the requirement that the scalar density $\bar{\psi}\psi$ of the quarks also vanishes at the boundary say, $r = R$. The lowest energy solutions ($s_{1/2}$-state) of the Dirac's equation for massless fermions restricted by the above mentioned boundary conditions will lead to,

$$p_0 = \frac{2.04}{R}.$$

Considering the bag pressure as due to the energy difference between the vacuum inside and outside the bag, the total energy for an N-quark system becomes,

$$E = \frac{2.04N}{R} + \frac{4\pi}{3} R^3 B.$$

The equilibrium radius of the system located at the radius R, is determined by,

$$\left.\frac{dE}{dr}\right|_{r=R} = 0,$$

which leads to a bag pressure constant,

$$B^{1/4} = \left(\frac{2.04N}{4\pi}\right)^{1/4} \frac{1}{R}.$$

Taking $R \approx 0.8$ fm as the radius for a three quark bound system (a baryon), an estimate of the bag pressure constant can be obtained. Generally, the value of the bag pressure $B^{1/4}$ is taken within a range between 145 MeV and 235 MeV. Now it is clear that if the pressure of the quark matter inside the bag is increased, there will be a point when the pressure directing outward will be greater than the inward bag pressure. When this happens, the bag pressure can not balance the outward pressure and the bag can not contain the quark matter inside the baryon. A new phase of matter consisting of quarks, antiquarks and gluons in a deconfined state is then possible. There can be two possibilities when a high pressure is generated, (i) the temperature of the matter is high, and/or (ii) the baryon number density is large.

1.4.4 Quark-Gluon Plasma at High Temperature

Consider the case of a quark-gluon system in thermal equilibrium at a high temperature T, within a volume V. Once again treat the quarks and gluons as non-interacting massless particles. It is also assumed that the total number of quarks and total number of antiquarks are equal so that the net baryon number in the system is zero. Considering the Fermi-Dirac distribution for quarks and antiquarks, and Bose-Einstein distribution for gluons one can estimate the partial pressure arising due to the quarks, the antiquarks and the gluons separately. Taking together all these contributions the total pressure (P) of an ideal QGP comes out as,

$$P = \left[g_g + \frac{7}{8}(g_q + g_{\bar{q}})\right] \frac{\pi^2}{90} T^4 = 37 \frac{\pi^2}{90} T^4,$$

where $g_q (= g_{\bar{q}}$ is the degeneracy factor of the quark (antiquark) states and g_g is the degeneracy factor of the gluonic states. The energy density of the quark-gluon matter at a temperature T is,

$$\epsilon = 37 \frac{\pi^2}{30} T^4.$$

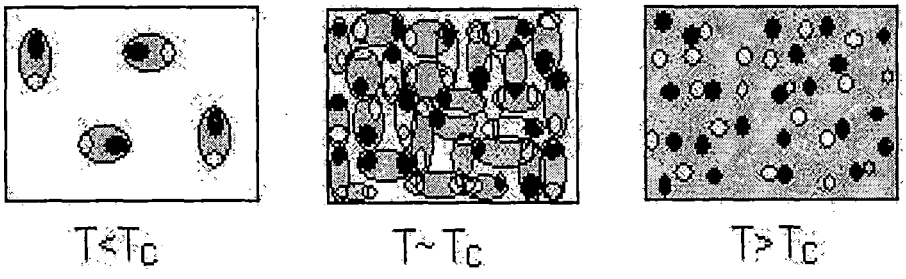

Figure 1.6: A volume enclosing colour neutral hadrons when heated above the critical temperature T_c, undergoes a phase transition to a sate comprising of free quarks, antiquarks and gluons.

As the total internal pressure P due to the quark matter increases with increasing temperature, there exists a critical value of temperature at which the internal pressure will be equal to the bag pressure B. The critical temperature T_c is also related to the bag constant as,

$$T_c = \left(\frac{90}{37\pi^2}\right)^{1/4} B^{1/4}.$$

For $B^{1/4} = 215$ MeV we have $T_c \approx 150$ MeV. If the quark matter in a bag is heated up to a temperature greater than this critical temperature, the quark matter inside the bag will experience a pressure greater than the bag pressure. When this happens the bag will not be able to hold the quark matter within the bag and the quark matter will be deconfined.

1.4.5 Quark-Gluon Plasma at High Baryon Density

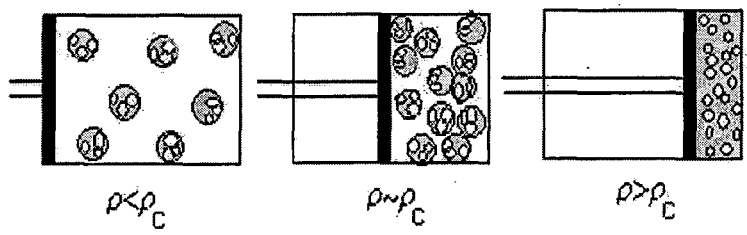

Figure 1.7: A volume enclosing colour neutral hadrons when subjected to extreme pressure, undergoes a similar phase transition beyond the critical density ρ_c.

Let us now look into the possibility of deconfinement at high baryon density at $T = 0$. Because of the Pauli's exclusion principle, an individual quark must populate a single state associated with a definite set of quantum numbers. Due to this, when the number density of quarks increases the quarks must populate states of higher momentum, where the degeneracy of the states are high. Due to this degeneracy the quark gas acquires a pressure, which increases with the increasing quark density. When this pressure exceeds the value of bag pressure, the confinement of quarks within the bag becomes impossible, and a state of deconfined quark matter may then be achieved.

To determine the pressure arising from relativistic quark gas at which the deconfinement occurs at temperature $T = 0$, one may assume for simplicity that the contributions comes only from the quarks. If μ_q is the Fermi momentum i.e. highest possible value of momentum for the quarks at temperature $T = 0$, the energy density of a quark gas can be written as,

$$\epsilon_q = \frac{g_q}{8\pi^2}{\mu_q}^4.$$

Corresponding pressure density is,

$$P_q = \frac{g_q}{24\pi^2}{\mu_q}^4.$$

At critical point this quark pressure will be equal to the bag pressure B. This leads to,

$$\mu_q = \left(\frac{24\pi^2}{g_q}\right)^{1/4},$$

which corresponds to a critical quark number density

$$n_q = 4\left(\frac{g_q}{24\pi^2}\right)^{1/4} B^{3/4}$$

while the corresponding baryon number density is,

$$n_B = \frac{4}{3}\left(\frac{g_q}{24\pi^2}\right)^{1/4} B^{3/4}.$$

For a bag pressure of $B^{1/4} = 215$ MeV, the critical baryon number density at which the hadronic matter becomes a quark-gluon plasma with a high baryon content at $T = 0$ is $n_B = 0.8/fm^3$, which is more than five times larger than the normal nuclear matter density. When the baryon density exceeds the critical value, the bag pressure is not strong enough to withstand the pressure due to the degeneracy of quarks, and the confinement of quarks within the individual baryon bags will not be possible, leading to the formation of a state of deconfined quark matter. From the above discussion it is clear that at high temperature (> 144 MeV) and/or at high baryon density (> 5 times of nuclear matter density), an exotic state like the QGP may be created. It should however be mentioned that the critical values of temperature as well as the baryon density are model dependent, and so they not unique. It is generally accepted that a phase transition should occur if the baryon density becomes $n_B \approx$ (10 to 15) times the normal nuclear density, and the temperature is so high that the energy density reaches a value like $\epsilon \approx$ (2 to 3) GeV/fm^3.

1.5 The Experimental Scenario

To start it is worthwhile to look back into history, and summarily follow how the heavy-ion accelerator facilities has evolved with time (Table 1.1). The first serious attempt to study nuclear matter under extreme conditions was made at the Lawrence Berkeley Laboratory (LBL) by using the Bevalac facility. Heavy nuclei like Iron ($A = 56$), Krypton

($A = 84$) and Uranium ($A = 238$) were accelerated with an incident energy of a few GeV per nucleon for fixed target experiments. Among other observables in the experiments performed at the Bevalac the central aim was to study the shock compression in extended volume of nuclear matter. Soon the Russians also jumped into the fray and established their synchrophasotron facility at the Joint Institute of Nulcear Research (JINR) at Dubna near Moscow. It was possible for them to accelerate lighter ions like Carbon ($A = 12$), Neon ($A = 20$), Magnesium ($A = 24$) and Silicon ($A = 28$), at slightly higher incident momentum per nucleon ($4 - 5$ GeV/c) than that in the Bevalac. The JINR facility became available in the early 1980's. Using this facility various aspects of particle production in AB collisions like for example, the multiplicity distribution, the y/η distribution, a few particle correlation, azimuthal anisotropy etc. were investigated in fixed target experiments.

Table 1.1. History of Heavy-ion Accelerators

Accelerator	Year	Beam species	Circumference	$\sqrt{s_{NN}}$ GeV
Berkeley - Bevalac	1973	^{16}O, ^{56}Fe, ^{84}Kr, ^{238}U	$\sim 10^2$ mt.	2
Synchrophasotron	1985	^{12}C, ^{16}O, ^{20}Ne,	207.3 mt.	3
JINR - Dubna		^{24}Mg, ^{28}Si		
BNL - AGS	1987	^{28}Si	0.8 km.	5
	1992	^{197}Au		4
CERN - SPS	1986	^{16}O	6.9 km.	20
	1987	^{32}S		20
	1994	^{208}Pb		17
BNL - RHIC	2000	^{197}Au + ^{197}Au	3.8 km.	200
CERN - LHC	2008(?)	^{208}Pb + ^{208}Pb	26.7 km.	5600

With the advent of the Super Proton Synchrotron at the CERN and the Alternating Gradient Synchrotron (AGS) at the Brookhaven National Laboratory (BNL), the prospect of achieving a deconfined QGP like state over an extended volume became brighter. These machines at first started producing lighter ions like Oxygen ($A = 16$), Sulfur ($A = 32$) at CERN and Silicon ($A = 28$) at BNL, and at a later stage heavy nuclei like Lead ($A = 208$) at CERN and Gold ($A = 197$) at BNL. The SPS facility for accelerating nuclei

came first at the late 1980's and the AGS in the early 1990's. In both places many fixed target experiments were carried out, with typical incident ion energy $\sim$ a few hundred GeV per nucleon at the SPS, and $\sim$ 10 GeV per nucleon at the AGS. Several indicators to identify a probable phase transition, have been thoroughly examined by analyzing the data available from the experiments performed both at SPS and AGS. They were compared with models based on numerical simulations, the theories were modified and the data were reexamined. But no concrete evidence of a colour deconfined state was available, thus eluding the expectation of a large number of researchers working in this area. In a bid to achieve a higher *cms* energy the Relativistic Heavy-ion Collider (RHIC) was installed at the BNL, that started functioning in the year 2000. Instead of using fixed targets two beams of Gold nuclei with equal momentum were allowed to impinge upon each other from two opposite directions, resulting in a much higher value of *cms* energy, $\sqrt{s_{NN}} = 200$ GeV. New features have been observed in the RHIC data. However, there is enough indication, that some of the signatures proposed during the AGS-SPS era have still stood the test of time. The lesson of RHIC experiments is that, though the development is proceeding in the right direction, to achieve the ultimate goal of creating and identifying a QGP like state, one has to wait until sometime in the current decade, when the Large Hadron Collider (LHC) at CERN starts to accelerate Lead ions at $\sqrt{s_{NN}} = 5600$ GeV. In the next subsection the experimental arrangements of some of the collaborative experiments performed in the BNL AGS, the CERN SPS and also in the BNL RHIC have been briefly outlined [1, 8, 10, 18]. The experimental results obtained from these experiments have been incorporated in section 1.7, where each signature to identify QGP formation has preceded corresponding experimental results. Within the limited scope of the present thesis it is practically impossible to discuss all experiments performed till date, and any omission though unintentional is regretted.

1.5.1 Experiments at the BNL AGS

Since 1960, the Alternating Gradient Synchrotron (AGS) has been one of the world's premiere particle accelerators, well known for three Nobel Prizes won as a result of researches performed there. The AGS name is derived from the concept of alternating gradient focusing, in which the field gradients of the accelerator's 240 magnets are suc-

cessively alternated inward and outward, permitting particles to be propelled and focused both in the horizontal and vertical planes at the same time. Capable of accelerating 25 trillion protons with every pulse, and heavy-ions such as silicon, gold and iron, the AGS during its most productive period (1992-1993) was annually used by 850 users from 180 institutions from around the world. The AGS receives protons from Brookhaven's 200 MeV linear accelerator (LINAC). The AGS Booster, constructed in 1991, further augmented the capabilities of the AGS, enabling it to accelerate protons and heavy-ions to higher energies. ^{28}Si ions at 14.6A GeV in 1987 and ^{197}Au ions at 10.6A GeV in 1993 were available from the BNL AGS for different fixed target experiments. Currently the AGS is being used as an injector for the Relativistic Heavy-Ion Collider (RHIC). Short description of three experiments performed in the BNL-AGS has been given in Table 1.2.

Table 1.2. Three Experiments at BNL AGS

Experiment	Main Detector(s)	Observables
E802	Zero degree calorimeter (ZDC), Pb-glass Calorimeter (PBGL) Target multiplicity array (TMA), Magnetic spectrometer	E_{ZD}, $\rho(\eta)$, p, $\bar{p}$, d, $\pi^{\pm}$, $K^{\pm}$ spectrum
E810	Time projection chamber (TPC)	Momenta and angles of charged particles
E814	NaI + U calorimeter, Target calorimeter (TCAL), Silicon multiplicity counter, Participant calorimeter (PCAL), Forward spectrometer and calorimeter	Transverse energy E_t, multiplicity of n and p in the forward direction

The E802 Experiment: The E802 Experiment experiment is the first heavy-ion programme at BNL. This collaboration studied the production of $K^{\pm}$ and $\pi^{\pm}$ and their ratios, in Si + Au central collisions at 14.5A GeV/c. The layout of the BNL E802 experiment is shown in Fig. 1.8. To identify whether the collisions are central or peripheral, three devices namely Target Multiplicity Array (TMA), Lead Glass Electromagnetic Calorimeter (PBGL) and Zero-degree Hadronic Calorimeter (ZDC) are used. The TMA is made of

tabular counters operated in the proportional mode. In order to determine the tracking of the produced particles two sets of drift chambers (T_1, T_2) are placed in front, and two other sets (T_3, T_4) behind a magnet. This experiment has a powerful identification system for charged particles. The particle identification system consists of 160 flat plastic scintillator time of flight walls (TOF), a 96 segment aerogel Cerenkov counter (AEROC), a 40 segment high pressure gas Cerenkov counter (GASC), and an array of three gas Cerenkov counters (CC) with their associated scintillators (S_1, S_2) and tracking chambers (T_5, T_7).

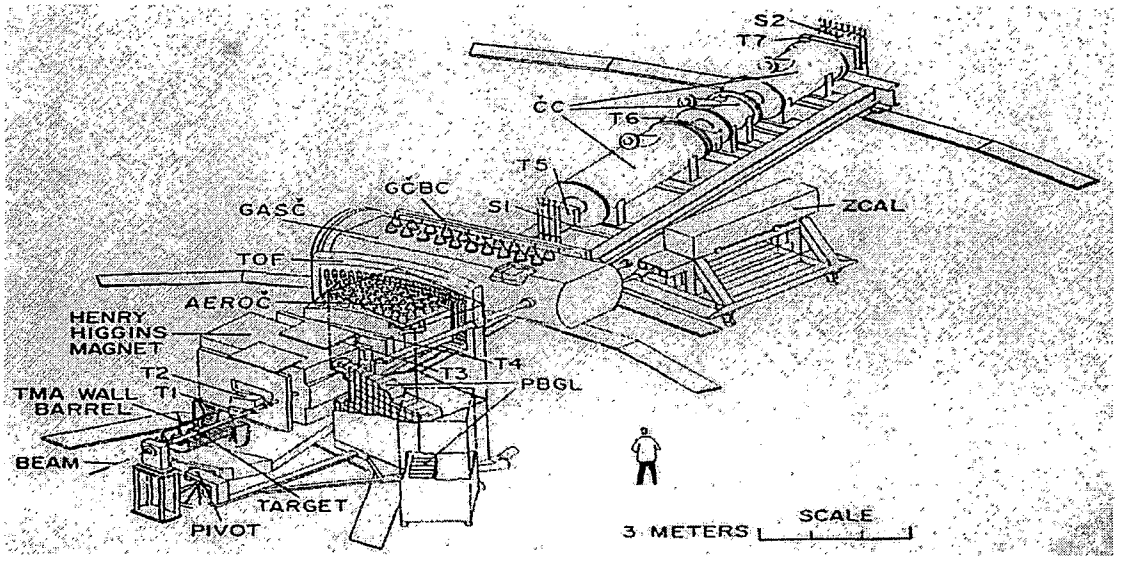

Figure 1.8: The E802 experimental set up.

The E810 Experiment: The main intention of the E810 Experiment was to measure the angles and momenta of charged tracks, using the time projection chambers (TPC's) and trigger detectors. This program allowed the experimenters to look for anomalous behaviour in the y/η, multiplicity, p_t distributions of the produced particle and the participating nucleons. Three TPC modules downstream of the target are used to measure the momenta and angles of the produced charged particles. The ability of the E810 apparatus to detect particles in a relatively large solid angle allowed the researchers to systematically study the correlation among various possible signals. These observations were on an event-by-event basis so that particularly interesting classes of events could be selected and added together to search for new effects (like strangelets) implying a QGP, or

other new states of matter in a manner which tends to maximize signal - to - background ratios.

The E814 Experiment:

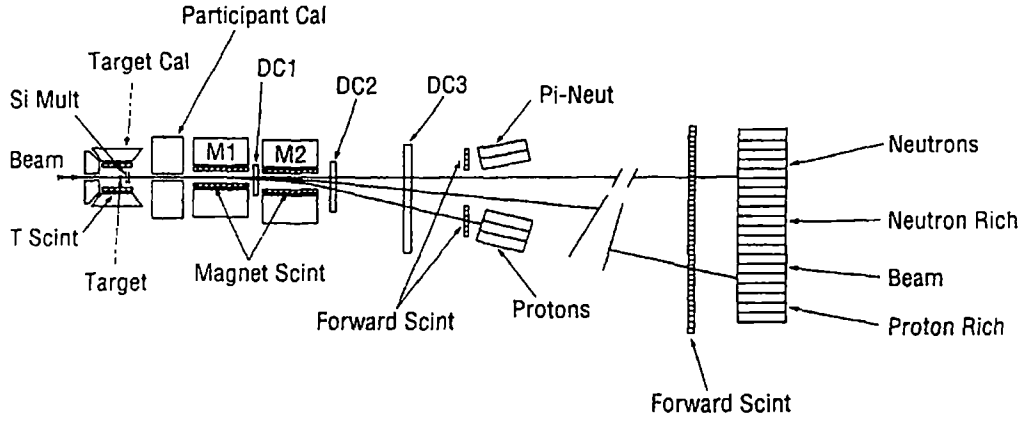

Figure 1.9: The E814 experimental set up.

The E814 collaboration studied ^{28}Si + Al, Cu and Pb collisions at $E_{lab} = 14.6$ GeV/nucleon at the BNL AGS. The experimental setup used in the E814 Experiment is shown in Fig. 1.9. The detectors used in this experiment may be divided into two groups. The upstream set of detectors mainly consists of a target calorimeter, target scintillators, participant calorimeter, and the Silicon multiplicity detector. This set of detectors were mainly designed for detecting the reaction products and target fragments at large angles, such as those produced in more central collisions. A drift chamber, Uranium calorimeters, forward scintillators and magnet scintillators are the constituent components of the downstream detector. The target is surrounded by participant calorimeter (PCAL) and target calorimeter (TCAL). PCAL covers the forward hemisphere ($0.83 \leq \eta \leq 4.20$), and TCAL covers the backward hemisphere ($-0.9 \leq \eta \leq 0.8$). The beam enters through a hole in the back wall of the target calorimeter. Forward going particles pass through the PCAL opening and magnets M1 and M2, which provide the deflection for the forward spectrometer. Track positions are measured in drift chambers DC1, DC2 and DC3. Charge is measured in the forward scintillators and energy is measured in U/Cu calorimeters. The charged

particle multiplicity is measured with the two silicon pad detectors located downstream of the target and inside the TCAL.

1.5.2 Experiments at the CERN-SPS

The Super Proton Synchrotron (SPS) is the second largest of the CERN accelerators, soon going to loose its long lasting glory to the Large hadron Collider, that will start to function sometime in 2008. The SPS has about 7 km circumference, has 1317 conventional (room temperature) electromagnets including 744 dipoles to bend the beams round the ring. A proton beam of 400 GeV energy was first extracted from the SPS in 1976 with a proton flux of $5 \times 10E12$ per pulse. The SPS was later modified to accelerate heavy-ions like ^{16}O at 60 and 200A GeV/c, ^{32}S at 200A GeV/c (year: 1986-'87) and ^{208}Pb at 158A GeV/c (year: 1994). The ions partially stripped of their electrons, originate from an electron cyclotron resonance, pass through a radio frequency quadrupole, and then they are injected to the linear accelerator (LINAC), where they are accelerated to an energy of 4.2A MeV. To get rid of the remaining electrons the ions are then allowed through a stripper foil (0.5 mm thick Al), and then successively accelerated by the proton synchrotron booster (PSB) and proton synchrotron (PS). They come out of the PS with an energy of 4.2A GeV, and then passes through another stripper, that completely ionizes the ions. These ions are then injected into the SPS, where they are accelerated at their highest energies. The ions are extracted at seven different points located at the CERN West and North Area experimental cites. Various experiments were performed in CERN using the accelerator namely Super Proton Synchrotron. Almost 22 years have passed since the CERN ion programme started. All the experiments carried out up to present may be divided into two ages. One is the Oxygen-Sulfur age experiments (1986-1993) and another is the lead age experiments (1994-present). Short summary of some of the CERN heavy-ion experiments is given below with a list of the same in Table 1.3.

The NA34 Experiment: The detector used in the NA34 experiment has two targets. One of them, target 1, consists of the wires of a multiwire proportional chamber. It is surrounded by a Uranium-scintillator calorimeter (U/Sc). Along the beam line there are, a transition radiator detector (TRD) to identify electrons, target 2, a Uranium-liquid Argon calorimeter (U/LA), a Uranium-scintillator calorimeter (U/Sc) followed by a muon

spectrometer consisting of a magnet and multiwire proportional chambers. Another part of the detector called the External Spectrometer sees target 1 through a slit made into the front of U/Sc calorimeter and was designed to detect photons. It consists of a multiwire proportional chamber followed by an iron plate for γ conversion (PC/Conv), and two drift chambers one on each side of a magnet. Photons produced in target 1, when crossing the iron plate, are converted into electron-positron pairs whose trajectories are curved in the magnetic field and detected by the drift chambers.

Table 1.3. Small experiments at CERN SPS: Oxygen - Sulfur age (1986 - 1993)

Experiment	Detector	Observables
EMU01	Nuclear Emulsion, Emulsion Chamber	Shower multiplicity (n_s), Fluctuation, η distribution $\rho(\eta)$, Projectile (target) fragmentation: PF (TF)
EMU02	Plastic	Electromagnetic Dissociation (ED), PF and Fractional charges,
EMU03	Nuclear Emulsion	n_s, PF, $\rho(\eta)$
EMU04	Nuclear Emulsion	Cross-section: direct e^-e^+ pairs
EMU05	Emulsion chamber with magnetic field	n_s, $\rho(\eta)$, K/π ratio, p_t for $\pm$ particles, Boson interferometry
EMU07	Nuclear Emulsion	n_s, $\rho(\eta)$, Fluctuation
EMU08	Nuclear Emulsion	ED, n_s, $\rho(\eta)$, PF and TF, Fluctuation
NA39	Mercury tank	Search for free quarks
NA40	Au-target, γ-spectroscopy	ED, ^{197}Au(B,X)^{196}Au
NA41	Au-target, Si-telescopes	Spallation, Multifragmentation
WA86	Plastic	Calibration for magnetic monopole search at Gran Sasso
WA87	Plastic	ED, Fractional charges
WA88	Plastic	Test of Bubble damage detectors

The NA35 Experiment: The NA35 detector has a streamer chamber placed within a magnetic field, which allows the measurement of charged particles trajectories, momenta,

sign of the charge and multiplicities. It detects also secondary particles coming of some decays, among them the important Λ, $\bar{\Lambda}$ and ${K_s}^0$ decays. A veto calorimeter (a zero-degree calorimeter) placed downstream along the beam line defines central and peripheral collisions. It has an electromagnetic calorimeter (PPD) and a hadronic calorimeter (Ring Cal + Intermediate Cal) both covering the η interval $2.2 \leq \eta \leq 3.9$.

1.4. Large Experiments at CERN SPS: Oxygen - Sulfur age (1986 - 1993)

Experiment	Detector	Observables
NA34	U-calorimeter, Liquid Ar-calorimeter Si-pad detectors, External spectrometer	E_t, $\rho(\eta)$, π^-, γ Low mass muon pairs
NA35	ZDC, Ring calorimeter Photon position detector Streamer chamber, Vertex magnet	E_{ZD}, E_t, $\rho(y)$, π^-, p, K_s^0, Λ, $\bar{\Lambda}$
NA36	TPC	K_s^0, Λ, $\bar{\Lambda}$, Ξ, Ω
NA38	Electromagnetic calorimeter, Di-muon spectrometer	E_t, Muon pair, J/ψ
WA80	ZDC, Mid-rapidity calorimeter (MIRAC), Mid-rapidity multiplicity detector (MIRAM), Large angle multiplicity detector (LAM) Pb-glass photon detector (SAPHIR)	E_{ZD}, E_t, Multiplicity of charged particles (n_{ch}), $\rho(\eta)$, γ, π^0
WA85	Ω-spectrometer Butterfly MWPC	K^+, K^0, Λ, $\bar{\Lambda}$, $\Xi^{\pm}$

The NA38 Experiment: The NA38 experiment consists essentially of a multiple active target made of 10 thin subtargets surrounded by cylindrical scintillators, an electromagnetic calorimeter made of scintillator fibers embedded in lead and divided into 30 cells, and a multi-muon spectrometer. The spectrometer has a beam dump to absorb hadrons, consisting of a Carbon part in which the muons propagate and a Tungsten-Uranium central core to kill the part of the beam which dose not interact in the target. There are

magnets for the measurement of the particle momentum and sign of the charge, four scintillator hodoscopes for the trigger, and eight multiwire proportional chambers for the measurement of trajectories, four placed before the magnet and four after. There is no arrangement for particle identification and multiplicity measurement. By definition a muon is a particle which leaves the target and reaches one of the hodoscope at the far end.

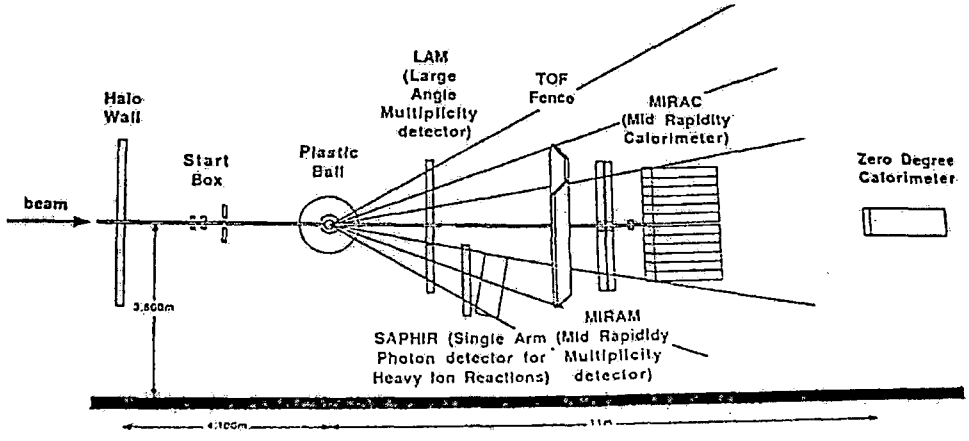

Figure 1.10: Layout of the WA80 detector.

The WA80 Experiment: The lay out of the detector used in WA80 Experiment is shown in Fig. 1.10. It consists of an array of 665 plastic scintillators (plastic ball). Three calorimeters, (a) Uranium-scintillators Zero-Degree Calorimeter (ZDC), (b) Electromagnetic Calorimeter (SAPHIR) and (c) Midrapidity Calorimeter (MIRAC) are used to measure the different energy. All the plastic ball scintillators are used to identify baryons and to measure their energy in the target fragmentation region of $-1.7 \leq \eta \leq 1.3$. The ZDC detector is placed at the end of the detector along the beam line and it is used to decide whether the collisions are central or peripheral. In case of central collisions a small portion of the beam reaches the calorimeter that measures a small energy. To measure the energy and direction of the direct photons the SAPHIR detector is used. This detector consists of 1280 Lead-glass modules. MIRAC is a hadron calorimeter and is very useful to measure the transverse energy flux with a large coverage. Multiplicity of charge particles are measured by the sets of Iarocci streamer tubes called LAM (Large Angle Multiplicity

detector), SAM (Single Arm Multiplicity detector), and MIRAM (Mid-rapidity Multiplicity detector), which cover a wide range of η ($-1.7 \leq \eta \leq 4.4$).

The WA85 Experiment: In this experiment an Ω spectrometer is installed. The Target T is placed inside the Ω magnetic field. Seven multiwire proportional chamber (MWPC) are placed within the magnetic field and four other chambers outside the magnetic field are used to trace the tracks. Two hodoscope HZ0 and HZ1 and the sensitive region of the chambers are matched to detect the charged particles with their transverse momentum above a certain minimum value chosen as $\sim$ 0.6 GeV/c. There is a good detector of multiplicities consisting of two arrays of 50μm pitch silicon microstrips, each with 512 channels, placed above and below the beam 15 cm downstream from the target. They measure multiplicities in the η range $2.1 \leq \eta \leq 3.4$. A hadron calorimeter placed along the beam line 25 meter downstream of the target defines central and peripheral collisions (a zero-degree calorimeter).

The NA49 Experiment: NA49 has a large acceptance magnetic and tracking spectrometer, detecting about 70% of all created charged particles simultaneously in each event. It is associated with a large volume gas-filled high-resolution time projection chambers (TPC). Two vertex TPC's are placed inside huge dipole magnets with superconducting coils. From the bending of the trajectories in the magnetic field one derives the particle momentum. Two larger TPC's are placed behind the magnets to measure very accurately the ionization energy loss of the particles in the chamber gas and therefrom deduce the particle velocity. The time-of-flight (TOF) measurement between the target and two walls of scintillation counters tiles provides another independent determination of the velocity for a significant fraction of the particles. The combined knowledge of the momentum and the velocity allows us to identify the mass of the particles. The tracking of charged particles is performed by time projection chambers (TPC). Each main TPC has a readout surface at the top of 3.9×3.9 m^2, and a depth of the field cage of about 1.1 m. It is filled with a gas mixture of Argon/Carbon Dioxide/Methane in the proportion 91/4.5/4.5. The track signals are read out by 25 proportional chambers providing up to 90 measured points and ionization samples on each particle trajectory. The accuracy of the measurement of the average ionization energy loss for a particle is about 4%. Downstream of the TPC's NA49 has a Ring Calorimeter and a Veto Calorimeter. The Ring Calorimeter is of

sampling type composed of sandwiched layers of Lead or Iron absorbers and scintillator plates. The summed light signal from the scintillator plates is proportional to the energy of the particles absorbed in the calorimeter. The device has a cylindrical structure, coaxial with the incident beam, and its sensitive area is circular with an outer diameter of 3.0 m and a 56 cm central hole. It is segmented into 240 cells, 24 sectors in azimuth and 10 rings radially. The Ring Calorimeter was used to measure the energy flow due to the particles produced in Pb+Pb collisions. The Veto Calorimeter is also of similar type. It is placed behind an iron collimator with a hole around the beam line designed to let pass only those fragments of the beam nuclei which have not interacted in the target foil. The recorded energy tells us which part of the beam nucleus interacted and thus how close the centers of the colliding nuclei approached during the collision.

1.5. Lead age experiments at CERN SPS: 1994 - present

Experiment	Detector	Particles	y_{lab}	p_t(GeV/c)
NA44	Focusing Spectrometer, TOF	K^+	$2.5-3.5$	$0.0-1.6$
NA49	TPC	$\phi, K^+, K^0, \Lambda, \bar{\Lambda}, \Xi$	$3.0-5.0$	>0.5
NA50	Dimuon spectrometer	ϕ	$3.0-4.0$	>1.0
NA52	Beam spectrometer	K^+	$1.4-6.0$	≈ 0
WA97	Silicon telescope	$K^+, K^0, \Lambda, \bar{\Lambda}, \Xi^-, \bar{\Xi}^+, \Omega^-, \bar{\Omega}^+$	$2.4-3.4$	>0.5

The NA45/CERES Experiment: CERES is one of the second generation heavy-ion experiments at the CERN SPS. It is dedicated to the study of e^+e^- pairs in relativistic nuclear collisions. CERES has taken data for about 10 years. The CERES spectrometer is optimized to measure electron pairs from 50 MeV/c up to 2 GeV/c at mid-rapidity $2.1 < \eta < 2.63$ with 2π azimuthal coverage. NA45 consists of two ring imaging Cherenkov detectors (RICH) with methane gas radiator ($\gamma_{th} \sim 32$, which makes it blind to most of the hadrons) to identify electrons. A pad chamber (PC) behind the two RICH detectors, in conjunction with all other detectors, is used to track the particles. Furthermore a Silicon Drift chamber (SiDC) before the first RICH allows particle tracking to the interaction point and hence determine the vertex (interaction point)of a collision. A Silicon Pad

detector is used for a coarse multiplicity evaluation, which is the bases for the centrality trigger.

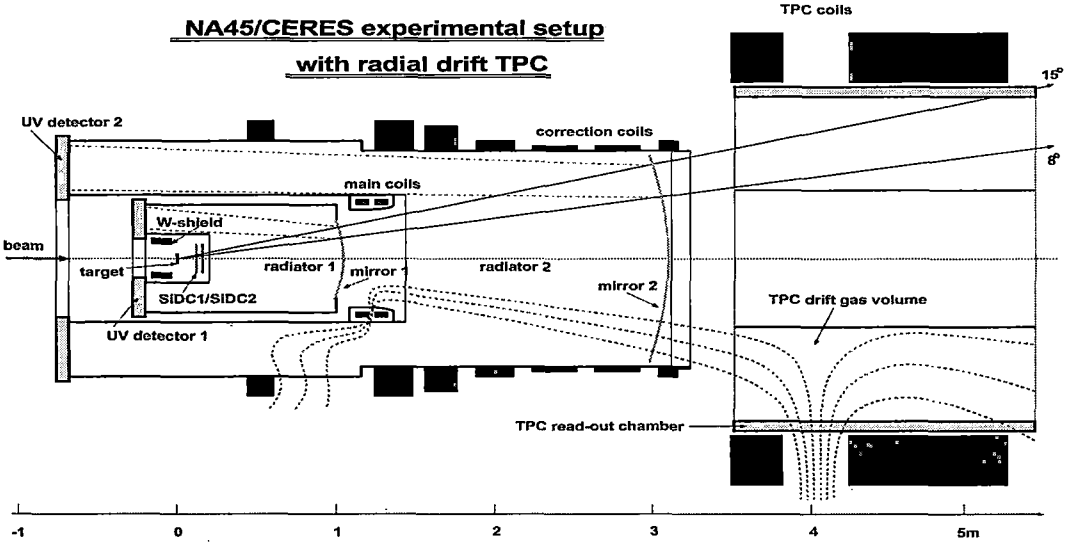

Figure 1.11: CERES detector system has been schematically depicted.

The CERES spectrometer has been upgraded by the addition of radial-drift time projection chamber (TPC) with an additional magnetic field behind the RICH detectors. The TPC was added to CERES in 1998. The new experimental setup is shown in Fig. 1.11. The TPC has a cylindrical geometry as all the other detectors in the experiment and covers the same angular acceptance in θ. Electrons produced by ionization due to the passage of charged particles in the TPC are drifted in a radial electric field defined by an inner cylindrical electrode and 16 read-out chambers at out side. The read-out chambers are multiwire proportional chambers with cathode pad read-out. There are 20 pad-rows in the beam direction with 16×48 pads in azimuthal direction, each sampling the radial (drift) direction in 256$\times$ bins. A magnetic field is provided by two large coils surrounding the TPC with currents running in opposite direction. The measurement of track curving through the magnetic field will provide momentum of the track. The TPC in conjunction with the two SDC's will significantly improve the dielectron mass resolution less than 2%

of the ω mass.

The NA50 Experiment: A dimuon spectrometer designed for the study of the production of J/ψ and high mass lepton pairs. The target is followed by the multiplicity detector and the transverse energy calorimeter, providing information on the centrality of the events, and by an absorber where all the particles except the muons are stopped. A "zero degree" hadron calorimeter for the measurement of the beam spectators is embedded in the absorber. The muons emerging from the absorber pass through a spectrometer that allows the measurement of their momentum. The spectrometer consists of a series of Multi-Wire Proportional Chambers (MWPC) placed before and after a magnet. Scintillator hodoscopes placed between the spectrometer chambers and behind an iron wall at the end of the layout provide the information used to define the dimuon trigger.

The NA57 Experiment: The NA57 setup is designed to measure the decays of strange baryons and antibaryons in the high ultrarelativistic AB collisions at the SPS. The principal aim of NA57 experiment is to investigate of strangeness enhancement effect at the variation of the energy and centrality i.e. the number of participants, of the nucleus-nucleus collisions. NA57 took the data with a Pb beam both at 158A GeV/c and at 40A GeV/c. In such a high-energy a huge number of particles are produced. To reconstruct the decay of Λ, Ξ, Ω,and K in such an environment NA57 used granularity telescope in silicon pixel plane. This detector had the capability to collect a large statistics. The main features of the telescope are:

(a) The telescope is made of 13 silicon pixel detector planes, for a total of about 1.1×10^6 channels. Seven planes of them use Omega2 front end chip with a pixel size of $75 \times 500 \mu m^2$ and the rest six planes use Omega3 front end chip with a pixel size of $50 \times 500 \mu m^2$.

(b) an array of six scintillator petals, placed 10 cm downstream of the target covering the η range $1 < \eta < 2$, used to trigger on the centrality of the collisions.

(c) A set of silicon multiplicity detectors sampling the charged multiplicity produced in the region $2 < \eta < 4$, in order to measure the centrality of the nucleus-nucleus collisions. The telescope is placed above the beam line, inclined and aligned with the lower edge of the detector on a line pointing to the target. The centrality of the collision is measured by sampling the charge multiplicity at central rapidity, with two stations of Multiplicity Strip Detectors (MSD).

1.5.3 Experiments at BNL RHIC

The Relativistic Heavy-Ion Collider (RHIC) at BNL is the first machine in the world capable of colliding heavy-ions. RHIC primarily uses ions of ^{197}Au one of the heaviest common elements, because its nucleus is densely packed with particles. RHIC's 2.4 mile ring has six intersection points where its two rings of accelerating magnets cross, allowing the particle beams to collide. The collisions produce the fleeting signals that are captured by one of RHIC's experimental detectors. If RHIC's ring is thought of as a clock face, the four current experiments are at 6 o'clock (STAR), 8 o'clock (PHENIX), 10 o'clock (PHOBOS) and 2 o'clock (BRAHMS). There are two additional intersection points at 12 and 4 o'clock where future experiments may be placed. The main components of the RHIC are:

1. A Tandem Van de Graaff generator that uses static electricity to accelerate atoms removing some of their electrons, The Tandem gives billions of these ions a boost of energy, sending them on their way toward the Booster.

2. Tandem-to-Booster line (TTB) - From the Tandem, the bunches of ions enter the Tandem-to-Booster beam line, which carries them through a vacuum via a magnetic field to the Booster. At this point, they're traveling at about 5% the speed of light.

3. The Booster synchrotron - The Booster synchrotron is a powerful and compact circular accelerator that provides the ions more energy, by having them surf ride on the downhill slope of radio frequency electromagnetic waves. The ions are propelled forward at higher and higher speeds, getting closer and closer to the speed of light. The Booster then feeds the beam into the Alternating Gradient Synchrotron (AGS).

4. AGS - As the ions enter the AGS from the Booster, they are traveling at $\sim$ 37% the speed of light. As they whirl around the AGS and are accelerated, until they are traveling at 99.7% the speed of light.

5. ATR - When the ion beam is traveling at top speed in the AGS, it is taken down another beam line called the AGS-To-RHIC (ATR) transfer line. At the end of this line, there is a fork in the road, where a switching magnet sends the ion bunches down one of two beam lines. Bunches are directed either left to the clockwise RHIC ring or right to travel counter-clockwise in the second RHIC ring. From here on, the counter-rotating beams are accelerated, as in the Booster and AGS, and then circulate in RHIC where

they will be collided into one another at as many as six interaction points.

The BRAHMS Experiment: One of the RHIC's two smaller detectors is the Broad Range Hadron Magnetic Spectrometer, or "BRAHMS". This device studies charged hadrons as they pass through its spectrometers. BRAHMS measures only a small number of particles emerging from a specific set of angles during each collision. The momentum, energy and other characteristics of the particles are measured very precisely.

The PHOBOS Experiment:

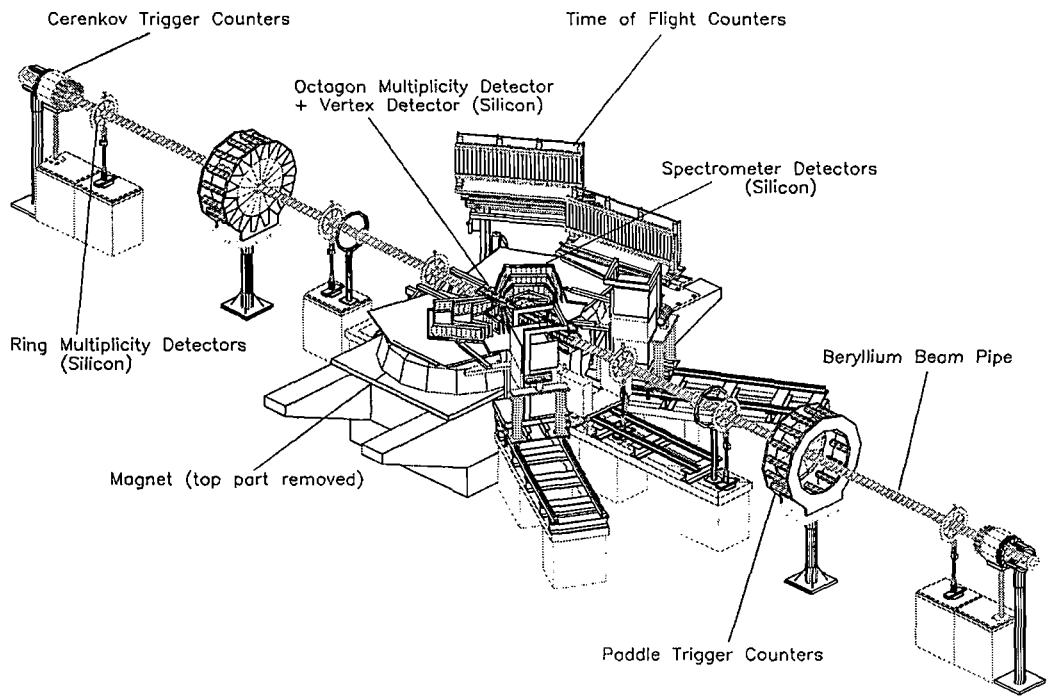

Figure 1.12: Layout of the PHOBOS experimental setup at RHIC.

The PHOBOS detector is comprised primarily of silicon pad sensors used in two separate detector subsystems, as illustrated in Fig. 1.12. The multiplicity array is a single layer of silicon that provides almost 4π coverage. This subsystem is used to measure the number of charged particles emitted from the collisions over a large pseudo-rapidity range $|\eta| \leq 5.4$. Two central double-layered sections of finer granularity Si pads above and below the Be beam pipe serve as a vertex detector. The second subsystem has two

spectrometer arms located near mid-rapidity, each consisting of a total of 16 layers of silicon. The spectrometer arms are used to track a fraction ($\sim$ 2%) of the total charged particles emitted in a 2 T magnetic field and to identify these particles by their specific energy loss (dE/dx). Scintillator time-of-flight (TOF) walls extend the particle identification capabilities to higher momenta in one arm.A minimum-bias event trigger is provided by a coincidence registered between two sets of 16 scintillator paddle counters located at $\pm$3.21 m from the nominal interaction point along the beam axis. The measured time difference is required to be consistent with the primary event vertex occurring between the paddle sets. The paddle counters, which cover $3 < |\eta| < 4.5$, are also used to estimate event centrality, by correlating the sum of their measured signals with the simulated event multiplicity within their acceptance. Each of the four RHIC experiments has zero-degree calorimeters (ZDCs) located $\pm$18.5 m from the nominal interaction points. The ZDCs provide a common means to measure luminosity and centrality using the beam-velocity neutrons from fragmentation and/or evaporation of the colliding nuclei. The event centrality determined with the paddle counters monotonically correlates with the estimated centrality from the ZDCs, providing an independent cross check of both methods. All the Si sensors in PHOBOS are AC-coupled single-sided, double-metal pad sensors with pad areas varying from 1 to 30 mm^2. Using this technology, all signals appear on bonding pads at one or two edges of the sensor, where the read-out chips are connected. The Si sensors are read out with VA-HDR-1 chips, providing an analog measurement with large dynamic range (up to 100 MIP) of the ionization charge deposited in each pad. The analog signals are multiplexed out for digitization by 12-bit ADCs. Integrated into the read-out chain is a gain calibration system, which is used to calibrate each individual channel. Latch-up circuitry that interlocks during single-event upset was included to protect against chip radiation damage.

The PHENIX Experiment: The PHENIX detector records many different particles emerging from RHIC collisions, including photons, electrons, muons, and hadrons. PHENIX weighs 4,000 tons and has a dozen detector subsystems. Three large steel magnets produce high magnetic fields to bend charged particles along curved paths. Tracking chambers record hits along the flight path to measure the curvature and thus determine each particle's momentum. Other detectors identify the particle type and/or measure the

particle's energy. Still others record where the collision occurred and determine whether each collision was "head-on" (central), a "near-miss" (peripheral), or something in between. The PHENIX detector is located at the 8 o'clock position on the RHIC ring. The PHENIX Experiment consists of a collection of detectors, each of which perform a specific role in the measurement of the results of a heavy-ion collision. The detectors are grouped into two central arms, which are capable of measuring a variety of particles including pions, protons, kaons, deuterons, photons, and electrons, and two muon arms which focus on the measurement of muon particles. There are also additional event characterization detectors that provide additional information about a collision.

The STAR Experiment: The Solenoidal Tracker at RHIC (STAR) is a detector which specializes in tracking the thousands of particles produced by each ion collision at RHIC. Weighing 1,200 tons and as large as a house, STAR is a massive detector. It is used to search for signatures of the form of matter that RHIC was designed to create: the quark-gluon plasma. It is also used to investigate the behaviour of matter at high-energy densities by making measurements over a large area. STAR's "heart" is the Time Projection Chamber, made of many electronic systems, which tracks and identifies particles emerging from heavy-ion collisions. As each collision occurs, STAR measures many parameters simultaneously to look for signs of the quark-gluon plasma. By using powerful computers to reconstruct the sub-atomic interactions which produce the particles emerging from each collision, the detector can, in a sense, run time backwards. This process can be compared to examining the final products which come out of a factory and trying to determine what kinds of machines produced them. The goal of STAR is to obtain a fundamental understanding of the structure of interactions between particles called hadrons, which are made of quarks and gluons. STAR is located at the 6 o'clock position on the RHIC ring.

1.6 Signatures of QGP in Heavy-ion Interactions

Relativistic heavy-ion collisions are dynamical processes characterized by typical length scale of $\sim$ 10 fm and time scale $\sim$ 10 fm/c. Even if the QGP or a QGP like state is created at any stage of the collision, it is an extremely difficult task to detect it. The

central region with high-energy density cools down very rapidly, and the outcome is only a large number of colour neutral hadrons in the final state. As it is the case for present day ultra-relativistic collisions between two heavy nuclei, from a debris of $\sim 10^2 - 10^3$ particles per collision it therefore, requires a high degree of theoretical insight as well as experimental skill to identify correct signals and trace back for the production of any exotic state like the QGP. As a result of the research efforts during last few decades several signatures for QGP production have been identified. Most of them have already been put to experimental test undertaken by small and big collaborations. While still none of them can claim to be an unambiguous candidate for the QGP, it is worthwhile to know where do we stand at present. A list of some of these signatures is furnished below,

(i) Enhancement of thermal dileptons and photons

(ii) Modification in the properties of heavy mesons such as J/ψ due to colour screening

(iii) Measurement of the particle producing source size through boson interferometry

(iv) Enhancement in heavier flavours such as, strangeness and charm production

(v) Elliptic flow of hadrons and modification in the jet structure

(vi) Suppression of event-by-event fluctuation of conserved charges.

In the following subsections qualitative arguments as to why a particular phenomenon among those listed above, can be treated as a probable QGP signature will be given within the limited scope of the present thesis. The probable physical processes involved in each case have been emphasized. As far as possible, mathematical intricacies, which are beyond the scope of the present thesis, have been avoided [1, 8].

Besides the above signatures, dynamical fluctuation in the phase-space density distributions of produced particles have also been extensively studied in many small and big experiments. Such fluctuations are guided by certain scaling laws, that have been examined by analyzing multiparticle production data as well as through numerical simulations. The origin of dynamical fluctuations is being debated, and it still remains an open issue whether or not such fluctuations are a result of some kind of phase transition. Efforts have been made to correlate the fluctuations with definite geometrical patterns such as fractals. In the present investigation, we too have examined several issues related to the dynamical fluctuation of produced charged particles in ^{32}S-Ag/Br interaction at an incident momentum of 200A GeV/c. No distinction in terms of charge sign or mass of the

particles have been made. While in chapters III to V these issues have been discussed in the perspective of present experimental investigation, in section 1.7 a brief review of other experimental results on dynamical fluctuation have been made.

1.6.1 Dilepton Production

A dilepton is simply a system of lepton-antilepton pair. Inside a volume where deconfined quarks and antiquarks are freely moving, a quark can interact with an antiquark to form a virtual photon (γ^*), that can subsequently decay into a lepton (l^-) and an antilepton (l^+). A dilepton may be characterized by a dilepton four momentum $p = p^- + p^+$, its invariant mass squared $M^2 = p^\mu p_\mu$, and a dilepton transverse momentum $p_t = p_t^- + p_t^+$, where $p^-(p^+)$ is the four momentum of $l^-(l^+)$.

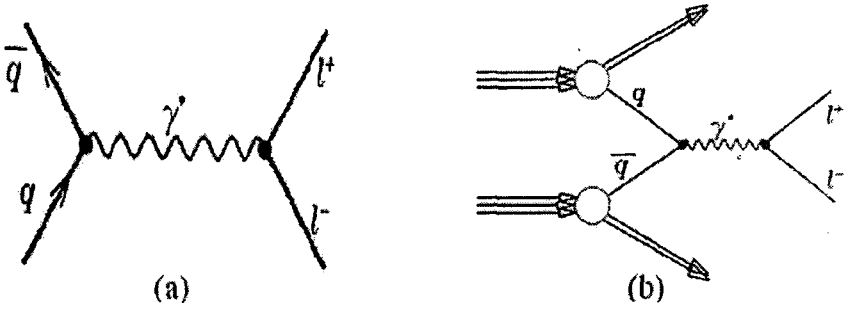

Figure 1.13: (a) Feynman diagram for $q\bar{q} \rightarrow l^-l^+$ process; (b) l^-l^+ production in the Drell-Yan process.

Leptons can be produced during the entire evolution of an AB collision. But they can be observed only when they can come out of the collision region to reach the detectors. Leptons can interact predominantly through electromagnetic and/or weak interactions. The interaction cross section of a lepton with another charged particle is $\sim (\alpha_e^2/s)$, where $\alpha_e(\approx 1/137)$ is the electromagnetic coupling constant, and $\sqrt{s}$ is the center of mass energy of the lepton-charge particle system. In comparison with the reaction volume corresponding electromagnetic/weak mean free path is sufficiently large, so that the leptons are able to come out of the collision region suffering little interaction. Hence they are considered to carry information of all stages of the evolution of the collision. The production rate and

the momentum distribution of the produced dileptons should depend on the distributions of the quarks and the antiquarks inside the QGP, that are dictated by the thermodynamic conditions of the plasma. Therefore, dileptons coming out from the collision region can carry information about the thermodynamical state of the medium from which they originate [19, 20]. The dilepton number density distribution can be shown to approximately follow a relation like,

$$\frac{dN_{l^-l^+}(QGP)}{dM\,dy} \sim T_0^3 \left(\frac{M}{T_0}\right)^{1/2} \exp(-M/T_0).$$

The relation can be parametrized to obtain the initial temperature (T_0) of the plasma. The problem is solved by using the usual Feynman diagram technique of the perturbative quantum electrodynamics (QED). However, it has to be remembered that, in high-energy nucleus-nucleus interaction QGP formation is not the only source of l^-l^+ pairs. Other processes such as the Drell-Yan process, hadronic interactions, decay of resonances etc. also contribute to the dilepton production. The contribution from a possible QGP formation can be filtered out only when the contributions from other sources are properly accounted for.

Dilepton Production From Other Sources

A. Drell-Yan process: In a nucleus-nucleus interaction a valance quark of a nucleon of one of the nuclei may interact with a sea antiquark of a nucleon of the other nucleus and they annihilate. Due to this reaction a virtual photon comes out that subsequently decays into an l^-l^+ pair. This is the Drell-Yan (DY) process [21], and the dominant non-QGP contribution of dilepton production actually comes from the DY process. The calculation is based on a Glauber type of probability distribution with respect to the impact parameter between the colliding nuclei [22]. The DY cross-section for the NN system is determined with a suitable choice of functional representation of the parton distribution functions for a particular flavour,

$$x\,q(x,Q) = A_0\,x^{A_1}(1-x)^{A_2}\,P(x)$$

corresponding to each nucleon. The choice of the smoothly varying function $P(x)$ differs considerably. For the heavy-ion collisions it can be assumed that, the net DY contribution comes from the DY contributions of a collection of independent nucleon-nucleon (NN)

interactions. In particular, for a head-on collision between two equal mass nuclei the number of l^-l^+ pairs coming from the DY process can be shown to scale with the mass number of colliding nuclei in the following way,

$$\frac{dN_{l^-l^+}(DY)}{dM\,dy} \sim A^{4/3}\frac{d\sigma_{DY}^{NN}}{dM\,dy}.$$

B. Hadronic decays: Hadrons and hadronic resonances are produced in nucleus-nucleus interactions. Dileptons may also come from hadronic interactions such as, $\pi + \pi \rightarrow l^-l^+$, and from the so called 'hadronic decay cocktail' consisting of the Dalitz decay of π^0 ($\pi^0 \rightarrow \gamma e^-e^+$), decay of hadron resonances e.g., ρ, ω, ϕ, and J/ψ particles. The contribution to dilepton production rate from known hadronic states can once again be estimated following Feynman diagram technique. The decays of hadron resonances show up as sharp peaks in the invariant mass spectrum of the l^-l^+ pairs. Charm mesons such as the $D^-(D^+)$ particle which are composite particles consisting of a charm quark (antiquark) and up, down or strange antiquarks (quarks), may also be produced by the interaction of a constituent of one nucleon with a constituent of the other. According to the lowest order QCD theory, particularly a quark of one nucleon interacts with the sea antiquark of other nucleon to form a virtual gluon which decays into a $c\bar{c}$ pair. The $c\bar{c}$ pair may also be produced as a result of the interaction of a gluon of one nucleon with a gluon of the other nucleon. Following the production of the $c\bar{c}$ pair in a NN hard scattering, the fragmentation of the c quark into a D^+ meson and the fragmentation of the $\bar{c}$ antiquark into a D^- meson result in the production of a D^+D^- pair. D^+D^- pair decays subsequently through the interaction $D^{\mp} \rightarrow l^{\mp}\bar{K}^0\bar{\nu}_l(\nu_l)$ and give rise to an l^-l^+ pair.

Some experimental observations on dilepton production

The NA45/CERES collaboration has studied the invariant mass spectra of low-mass e^-e^+ pairs in p+Be, p+Au interactions at 450 GeV/c, in S+Au interactions at 200A GeV/c, and also in Pb+Au interaction at 158A GeV/c [23]. For the proton induced interactions exclusive measurement of π^0 and η^0, was compared with the inclusive $M_{e^-e^+}$ spectra. The observed spectra were well explained by the known decays of vector mesons and Dalitz decay of neutral mesons. However, considerable excesses in the e^-e^+ yield was observed both in the S+Au and Pb+Au interactions in the low mass region between π^0-Dalitz and $\rho - \omega$ peaks ($M_{e^-e^+} \approx 0.4$ GeV). The yield was enhanced by a factor of $\sim$ 5(3)

in S(Pb) -induced interaction, and in both cases the enhancements were quite similar in shape. Beside the low M region significant excesses were also observed above $M_{e^-e^+} \approx 1.0$ GeV. Such excess production could not be explained in terms of known hadronic sources. Annihilation of thermal pions ($\pi + \pi \rightarrow e^-e^+$), which itself is an indication of creation of hot and dense matter during the collision, can to a certain extent account for the excess production of e^-e^+ pairs, though not entirely.

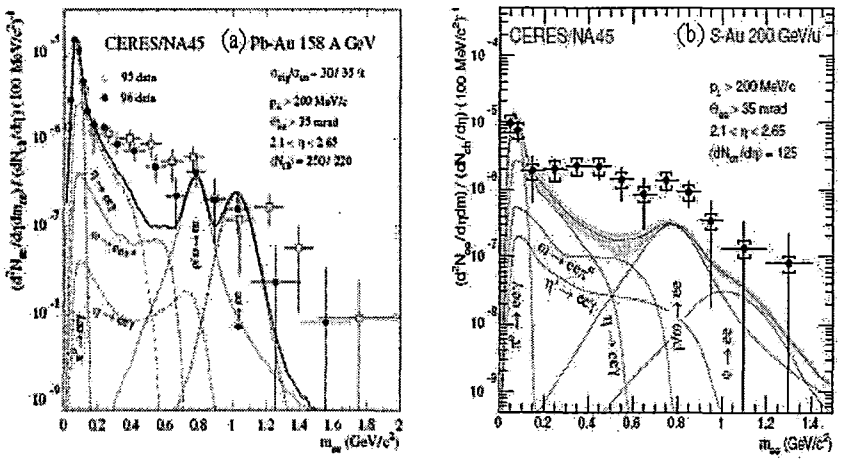

Figure 1.14: NA45/CERES result on excess e^-e^+ production in (a) Pb+Au interactions at 158A GeV/c, and (b) S+Au interactions at 200A GeV/c. The $M_{e^-e^+}c^2 = 0.2 - 0.8$ GeV region is to be noted.

In a similar analysis, data on dimuon invariant mass spectra from p+U interactions at 200 GeV/c collected by the NA38 group could be explained by lepton pairs from charm production and the DY mechanism. While the spectra obtained from S+U interaction at 200A GeV/c by the NA38 Collaboration [24], and from Pb+Pb interaction at 158A GeV/c by the NA50 Collaboration [25], showed excess $\mu^-\mu^+$ production around $M_{\mu^-\mu^+} \approx$ 2.0 GeV and below the J/ψ mass region. The effects were pronounced more in the central than in the peripheral events. The observed discrepancies in dilepton yields have been interpreted in terms of modified meson properties within a hot/dense medium of interacting particles, thereby indicating an onset of chiral symmetry restoration at the phase boundary between hadronic matter and QGP.

1.6.2 Production of Direct Photons

In a QGP like state the different possible ways of photon production are, (i) annihilation process - a quark interacting with an antiquark to produce a photon and a gluon, ($q\bar{q} \rightarrow \gamma g$), (ii) Compton process - a gluon interacting with a quark (antiquark) to produce a photon, ($gq \rightarrow \gamma q$) and/or ($g\bar{q} \rightarrow \gamma \bar{q}$). Besides these two, a quark can annihilate with an antiquark also to produce a pair of photons, ($q\bar{q} \rightarrow \gamma\gamma$). However, the probability of occurrence for annihilation into 2γ is less by a factor of (α_e/α_s), which is only a few percent of the other two, and therefore, can be easily neglected. Production of only a single photon in a $q\bar{q}$ annihilation is prohibited by the kinematic considerations. After a photon is produced, it must come out from the collision region in order to be detected. The photons interact only through electromagnetic interaction, and the corresponding mean free path is larger than the dimensions of the reaction volume. Therefore, the photons may not suffer any interaction as they make an exit from the collision zone, and hence they are considered to be clean signal for the state of the matter produced during the collision. The photon production rate and the photon momentum distribution will depend on the momentum distribution of the quarks, antiquarks and gluons present in the medium, which are governed by the thermodynamical conditions of the state. Therefore, photons produced inside the interaction region should carry information about the thermodynamical state of the medium at the moment at its production [26]. Kinematic differences between a sample of selected inclusive photons originating from high-energy AB interactions, and the photons that originate from known hadronic decays may serve as one of the possible tools to search for a QGP like state. It should however be remembered that, besides emission from the QGP photons can also be emitted through two other ways, e.g., from the hot hadron gas through hadronic decays, and through production by parton collisions. It is therefore, necessary to identify the contribution from different sources so as to extract the information on photon emission from the QGP. IF the net baryon density in the QGP is taken to be zero, the energy-momentum distribution of the quarks $f_q(p_q)$ will then be same as that of the antiquarks $f_{\bar{q}}(p_{\bar{q}})$. Both these distributions are of Fermi-Dirac type whereas, the gluons are guided by the Bose-Einstein type of distribution function. Using Feynman calculus, it is possible to find out the the invariant differential photon number distribution $\left(E_\gamma \frac{dN_\gamma}{dp_\gamma\, d^4x}\right)$ both for the annihilation and the Compton processes.

It is observed that the photons pick up the quark (antiquark) momentum distributions $f_q(p_q)$, and following Kapusta et al. [27] a relation for the differential number

$$E_\gamma \frac{dN_\gamma(QGP)}{dp_\gamma\, d^4x} \sim f_q(p_\gamma)\, T^2 \left\{ \ln\left(\frac{3.74\, E_\gamma}{g^2 T} \right) \right\}$$

is obtained.

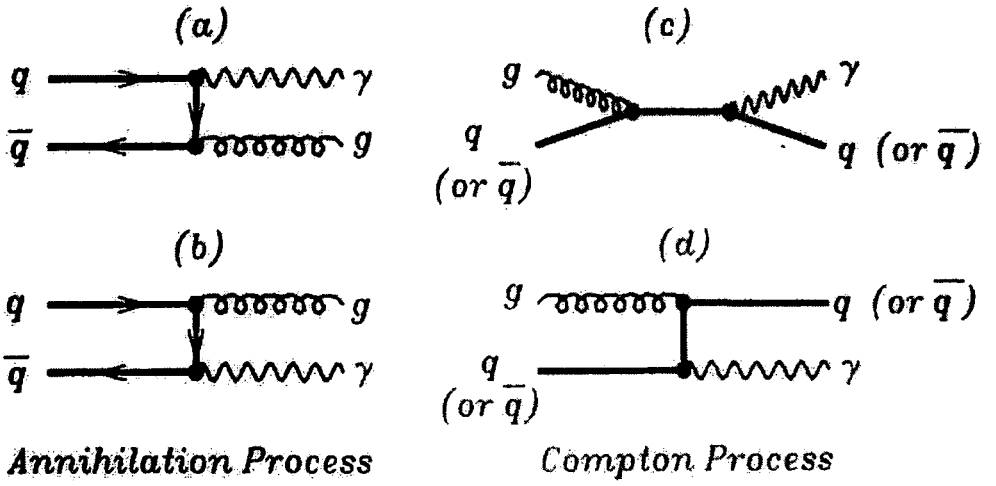

Figure 1.15: (a) and (b) Feynman diagram for photon production in annihilation process $q + \bar{q} \rightarrow g + \gamma$; (c) and (d) the same in Compton scattering process $q(\bar{q}) + g \rightarrow \gamma + q(\bar{q})$.

Photon Production From Other Sources

A. Hadronic interactions: Besides the QGP photons can be emitted by the hot hadronic gas following the annihilation of π mesons $\pi^+\pi^- \rightarrow \gamma\rho^0$, or through the interaction $\pi^\pm\pi^0 \rightarrow \gamma\rho^\pm$. Other possible interactions that may lead to photon production are, (i) $\pi^\pm\rho^0 \rightarrow \gamma\pi^\pm$, (ii) $\pi^\pm\rho^\mp \rightarrow \gamma\pi^0$, and (iii) $\pi^0 + \rho^\pm \rightarrow \gamma\pi^\pm$. Following the same procedure as that for the QGP photons one can determine the invariant differential number for the photons from hadronic decays, which has the following form,

$$E_\gamma \frac{dN_\gamma(\pi^i\pi^j \rightarrow \gamma\rho^k)}{dp_\gamma\, d^4x} \sim f_{\pi^i}(p_\gamma)\, \{\ln E_\gamma + C\}\,,$$

where C is a constant. Since $(\ln E_\gamma + C)$ is a slowly varying function of E_γ, the photon distribution from hadronic decays approximately follow the shape of the hadron distribution $f_\pi(p_\pi)$, and for high hadron energies this has a form $\sim exp(-E/T_h)$, where T_h

is the temperature of the hadron gas. On the other hand, for photons from the QGP the distribution will be characterized dominantly by a function like $\sim T^2 f_q(p_\gamma)$, where $f_q(p_\gamma) \sim exp(-E/T_q)$ and T_q is the characteristic temperature of the QGP. As $T_q > T_h$, it is expected that the two distributions for photon production will behave differently, and this difference can be utilized to distinguish between the sources of photon production.

B. Parton collisions: Photons may also be emitted by the initial state (much before a QGP like state is produced) collision of a constituent of one nucleon, with the constituent of other nucleon. For example, a quark of one nucleon can interact with a sea antiquark of the other nucleon to produce a photon and a gluon by the annihilation process and/or a gluon of one nucleon can interact with a quark or a sea antiquark of the other nucleon to produce a photon by the Compton process. Production of photons due to these parton collisions is similar to the production of photons from the QGP. The only significant difference between the two processes is the following. In the case of QGP the photons pick up the distribution function of the quark, antiquark and the gluons, whereas, in the case of parton collisions it is the structure functions, which play a similar role. Assuming same functional representation of the parton distribution as in the case of dilepton production, the characteristic temperature at which photons are produced from parton collisions comes out to be much larger than the characteristic QGP temperature It is also observed that the effective photon temperature at $\sqrt{s} = 200$ GeV will be large in the case of parton collisions than in the case of QGP. This signify that at large energies the photon yield from parton collision will be greater than the photon yield from the QGP. Besides the above photons may also be produced by the heavy-ion bremsstrahlung and decay of neutral mesons produced in the interaction such as the π^0 and ρ^0 mesons.

Some experimental observations on direct photon production

It is a difficult task to separate out the contributions from each source of photon production. Enhancement in direct photon production due to thermalization of QGP, considered as a signal, is likely to be shadowed behind a huge background of decaying hadrons such as $\pi^0 \rightarrow \gamma\gamma$ and $\eta \rightarrow \gamma\gamma$. Only a precise comparison of the inclusive photon spectra with contribution from all other known sources of photon production can provide the required information. The NA34 collaboration studied inclusive photon production in p+W, O+W, S+W and S+Pt interactions at 200A GeV/c within a rapidity range of

$1.0 < y < 1.9$ [28]. The photons were converted to e^-e^+ pairs by allowing them to pass through an iron plate, and drift chambers were used to measure their momenta. The sample size of reconstructed photons for each type of interactions was not very large. The major conclusions of this experiment were that, the p_t distribution of photons could be reproduced from known mesonic decays, and no significant difference in the inclusive spectra of photons produced in different types of interactions were observed. It was also observed that the ratio of number of γ's to the number of π^0's did not vary with the transverse energy E_t of the photons. The NA45 Collaboration once again measured the photon yields by the conversion method. The measurement covers a η range of $2.03 < \eta < 2.64$. Momenta of the e^-e^+ pairs were measured with a Cerenkov ring imaging spectrometer. Contribution to photon production from the $\pi^0 \rightarrow 2\gamma$ process was estimated from the measured distribution of the charged mesons. Results for central collision of S+Au at 200A GeV showed that, within a systematic error of 11%, there is no evidence of excess photons above the meson decay background.

The WA80 Collaboration studied inclusive photon spectra, $(\frac{1}{N_{ev}}\frac{dN}{dp_t})$ against p_t, covering a η range of $2.1 \leq \eta \leq 2.9$, in p+Au, O+C and O+Au central interactions at 60A and 200A GeV/c in 1986, and later in 1990 in S+Au interaction at 200A GeV/c [29]. Energy measured by a ZDC was used to classify the centrality of interactions. For all types of interactions the inclusive photon spectra were fitted with an analytical function like, $\sim \exp(-p_t/T_{eff})$. The resulting values of T_{eff} came out within a range of $\sim 200 - 235$ MeV. The WA80 experiment also studied the average $< p_t >$ of the inclusive photons as a function of centrality as well as the entropy density $\left(\propto \frac{1}{A_{part}^{2/3}}\frac{dn}{d\eta}\right)$, of the collisions. The $< p_t >$ value increases with both centrality and entropy density of the collisions. The WA80 experiment was later upgraded to WA93 experiment with Pb-glass calorimeter arrays and photon multiplicity detector. Data on inclusive photons covering a region $3.3 < \eta < 4.3$ in S+Au interaction at 200A GeV/c were collected. While for peripheral events there did not seem to be any excess photon yield over and above that obtained from the normal mesonic decays, a non-significant excess of direct photon production was observed in the most central collisions. However the scenario was consistent with or without a phase transition being taken into account. Thus none of the above mentioned experiments observed any significant excess in direct photon production. The experimen-

tal results could be reproduced by using hadron and string cascading models without invoking the formation of QGP.

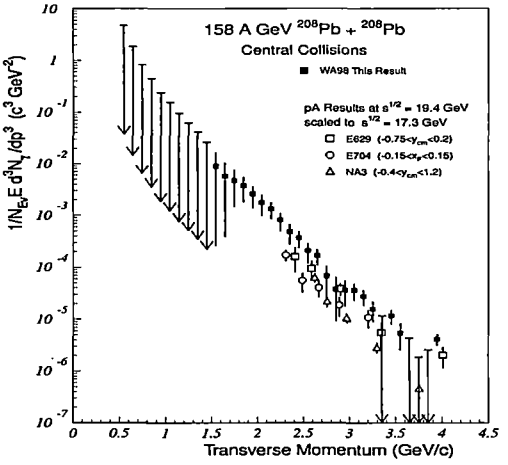

Figure 1.16: WA98 results on direct photon production in ^{208}Pb-^{208}Pb interaction at 200A GeV/c.

The WA98 experiment at CERN SPS performed a high precision search for inclusive photons in Pb+Pb interaction at 158A GeV covering a range $2.3 \leq \eta \leq 2.95$ and $0.3 \leq p_t \leq 4.0$ GeV/c [30]. For the same data sample neutral meson yield, that forms the basis for background calculation, were extracted. A significant photon excess over the background was observed in the central collisions for $p_t > 1.5$ GeV/c. No significant excess was however found in the peripheral collisions. When WA98 results in photon spectra were scaled by those from fixed target proton induced interactions at similar $\sqrt{s}$ value, the shape of the spectra did exhibit similarity, but the yield was enhanced in Pb+Pb collision. Even the model predictions that could successfully describe the Sulfur age results on inclusive photon yield, failed short by a factor $\sim 1-2$ in magnitude for the Pb+Pb collision. However, the global trend of the experimental γ-spectrum of WA98 could be reproduced by model calculations. Subsequent analysis showed that depending on the model assumptions, the initial temperature characterizing the photon spectrum can vary over a wide range ($205 \leq T \leq 270$ MeV), and the agreement between theory and experiment has always been reasonably good. Hence, while WA98 data can naturally be explained in a QGP scenario, it does not necessarily provide a concrete evidence for such

a phase transition.

The PHENIX experiment at RHIC made use of highly segmented electromagnetic calorimeters (Pb-scintillator type and Pb-glass Cherenkov type) to detect photons in high p_t region (upto $\approx$ 12 GeV/c), coming from Au+Au collisions at $\sqrt{s_{NN}}$ = 200 GeV [31]. Ratio of measured inclusive photon spectrum and the expected photon spectrum from mesonic decays for central collisions did exhibit a clear signal beyond p_t = 4 GeV/c. When compared with the photon yield from pp collision at $\sqrt{s}$ = 200 GeV, this ratio follows the expected scaling with respect to the number of binary collisions involved in Au+Au interactions. Calculation based on photon production due to interaction between partons from hard scattering with thermalized partons of the QGP shows that high p_t photons are not particularly suppressed.

1.6.3 Suppression of J/ψ Production

The evolution of QGP may be described in terms of four stages namely (i)pre-equilibrium, (ii) equilibrium, (iii) cooling, and (iv) hadronization. In the equilibrium state one actually studies the thermalized QGP. It is expected that within a thermalized QGP there would be enough energy density for the formation of heavier quarks and antiquarks in pairs (to conserve flavour) like for example the charm $(c, \bar{c})$ and strange $(s, \bar{s})$. It is also expected that while in most of the cases the quark and the antiquark fly apart in opposite directions, some of the quarks and antiquarks may form a quarkonium $(q\bar{q})$ bound state like for example the charmonium $(c\bar{c})$. Such heavy quarks can only be produced at an early stage of the collision when enough energy is available to the colliding partons. In a later stage, as and when the energy is distributed among hundreds of particles, no collision can provide sufficient energy to produce heavy quark flavours. The J/ψ meson is one such charmonium bound state with a mass of 3.1GeV. The potential $V(r)$ between c and $\bar{c}$ can phenomenologically be assumed as a linear combination of a Coulomb part and a confining linear part given by,

$$V(r) = \frac{q_c}{4\pi r} + \kappa r,$$

where q_c is the colour charge of the quark and κ is the $c-\bar{c}$ string tension coefficient. The presence of other quarks, antiquarks and gluons in the QGP, screen the colour charge of the c and $\bar{c}$, thereby reducing the effect of the attractive Coulomb part of the potential.

The process is similar to the Debye screening in an ordinary electron plasma, and due to this effect the Coulomb potential is modified to a Yukawa type of potential given by

$$\frac{q_c \exp(-r/r_D)}{4\pi r}.$$

The range of this potential is given by the corresponding Debye screening length r_D. On the other hand, the string tension coefficient κ depends on temperature. If a deconfined state like the QGP is formed then $\kappa \to 0$, at the high temperature that characterizes the QGP formation ($\sim$ a few hundred MeV), and the only way by which a $c\bar{c}$ bound system can be formed is through the Yukawa type of potential mentioned above. Moreover, as r_D changes inversely with temperature, the range of the attractive Yukawa type of force may be small compared to the Bohr radius of the $c\bar{c}$ system, and the formation of a $c\bar{c}$ bound state may not at all be possible. It should also be mentioned at this point that formation of similar quarkonium bound states for up, down and strange quarks are even less possible, simply because the corresponding Bohr radii are even more larger than r_D at characteristic QGP temperature. If any J/ψ state is formed in the initial stage of the AB collision, then in a QGP environment it should dissociate, and the charm quarks and antiquarks can only form open charm systems with lighter quarks such as, $D(c\bar{u}, c\bar{d})$, $\bar{D}(\bar{c}u, \bar{c}d)$, $D_s(c\bar{s})$ and $\bar{D}_s(\bar{c}s)$ mesons. Therefore, if a QGP like state is formed production of J/ψ particle will be highly suppressed, as was first suggested by Matsui and Satz [32] even before any experimental indication in this regard was available. This suppression of J/ψ production compared to the case when there is no possibility of creation of a QGP may, therefore, be used as a signature for the presence of QGP.

Some experimental observations on J/ψ production

The NA38 and NA51 collaborations at CERN carried out experimental investigation to study $\mu^-\mu^+$ production from the continuum, from vector meson decays and from the DY-process in several high-energy pA and AB interactions [33]. The experimental set up basically consisted of scintillators, an electromagnetic calorimeter and a multi-muon spectrometer. The J/ψ is detected via its decay $J/\psi \to \mu^-\mu^+$. The apparatus is triggered on by muon pairs and measures the electromagnetic energy released in the interaction. In this experiment the muon spectrometer is designed to accept $\mu^-\mu^+$ pairs within a rapidity range $2.8 < y_{lab} < 4.0$. The dimuon mass spectrum showed a continuum along

with a peak at 3.1 GeV that corresponds to the rest mass of J/ψ. One can obtain the number of J/ψ particles in the resonance peak region ($N_{J/\psi}$) and the number of $\mu^-\mu^+$ pairs in the continuum (N_{cont}) under the resonance peak. From pp to S+U, in all types of interactions studied, it has been found that the J/ψ production is suppressed and the ratio $N_{J/\psi}/N_{cont}$ decreases with increasing centrality. The centrality is measured either in terms of the transverse energy deposited, or in terms of number of participating nucleons in a particular interaction. However, in such early experiments induced by proton and light nuclei, the suppression of J/ψ was attributed to absorption of J/ψ in the nuclear matter, they had to traverse after production, and a simple absorption model can explain data up to central S+U collision at 200A GeV/c [34].

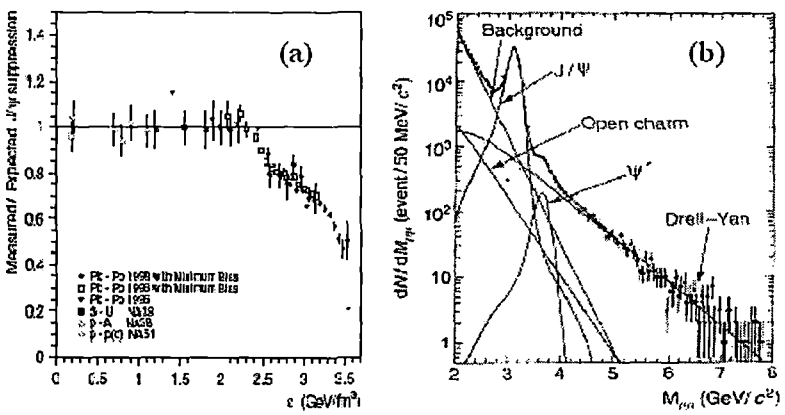

Figure 1.17: (a) Suppression of J/ψ production with increasing centrality (measured in terms of energy density); (b) The dimuon invariant mass spectrum showing the J/ψ peak at $M_{\mu\mu}c^2 = 3.1$ GeV [25].

Using a muon spectrometer, the NA50 collaboration studied the dimuon invariant mass spectrum at CERN SPS for various light ion induced interactions and also in Pb-Pb interaction at 200A GeV/c [25]. A diagram in this respect is given in Fig. 1.17(b). The continuous background of $\mu^-\mu^+$ pairs as well as those originating from different vector meson decays, were studied. Since the rate of DY process was found to remain same in all AB interactions, contribution of the DY process in AB interaction can be estimated from the corresponding value in pp interaction as,

$$\sigma_{DY}^{AB} = A\,B\,\sigma_{DY}^{pp}.$$

When the ratio $\sigma_{J/\psi}/\sigma_{DY}$ is normalized by the corresponding value expected from normal nuclear absorption, and the normalized ratio is plotted against the energy density ϵ achieved (Bjorken's formula), a clear suppression in J/ψ production is observed in Fig. 1.17(a) beyond $\epsilon = 2.3$ GeV/fm^3. However, it remains to be seen, whether or not the observed suppression does necessarily require formation a colour deconfined medium, to effect a screening in the colour $c\bar{c}$ binding potential.

1.6.4 Bose-Einstein Interferometry

The interference phenomenon associated with detecting two bosons in coincidence at two different space-time / energy-momentum points, is called intensity interferometry. The probability of coincident detection depends on the transverse separation of the detectors, as well as on the angular separation of the emitting source [35]. This method has been applied in radio-astronomy to measure the angular diameter of a distant star, and is called the Hanbury-Brown-Twiss (HBT) effect [36]. In particle physics also the HBT effect can therefore, be used to estimate the size of the particle emitting source [37]. There is however, a difference in the interference process for photons in astronomy and for mesons in AB interaction. While in the former case the interference takes place near the detector (say telescopes), in the latter case the interference takes place near the source. Assume that two identical bosons are produced with a small momentum difference $(p, p + \Delta p)$ at a short time interval $(t, t + \Delta t)$ with random relative phases. Let (a, b) be the points of emission separated by a distance R of the two bosons from an extended source, and (A, B) be the positions of the detectors separated by a distance D as shown in Fig. 1.18. Let the distance between the source and the detector be r. Let us denote the angles D/r and R/r, respectively, by Θ and Φ, and the distances (aA, bA, bB, aB), respectively by (x_1, x_2, y_1, y_2). The probability amplitude for the boson to start at $(\mathbf{x}, \mathbf{t})$ and detected at $(\mathbf{x}', \mathbf{t}')$ is given by,

$$\psi(k, x \rightarrow x') = \sum_{\text{all paths}} e^{iS(\text{path})},$$

the dominant contribution coming from the classical trajectory. It is therefore, reasonable to replace the sum by a single term like $\exp\{iS(\text{classical path})\}$. By simple algebraic maneuvering, it can be shown that, both for the nonrelativistic $\left(S = \int L dt\right)$ and the

relativistic $\left(S = -m\int\sqrt{dt^2 - d\mathbf{x}'^2}\right)$ cases,

$$S(\text{classical path}) \approx p.(x - x').$$

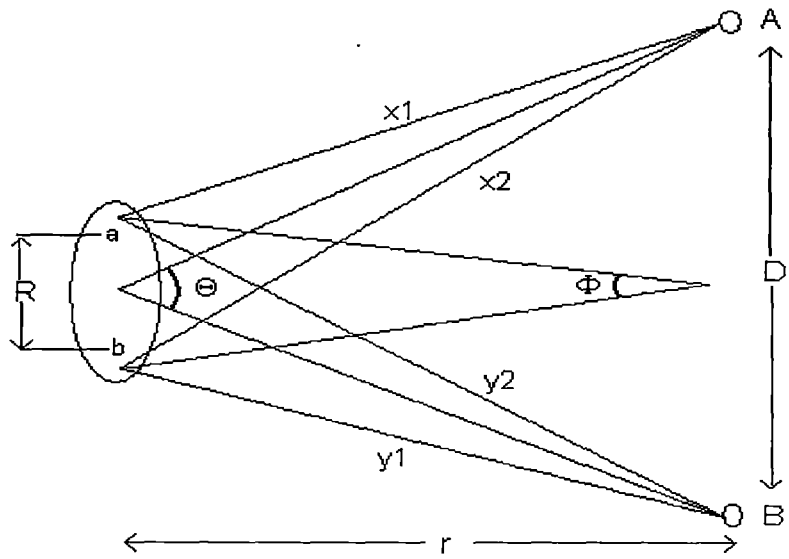

Figure 1.18: Schematic description of source size determination through Bose-Einstein correlation study.

There can be two distinct coincidence possibilities,

(i) A detects a particle coming from a and B detects a particle coming from b: the amplitude for this is given by, $\sim e^{ip.x_1}\, e^{ip.y_1}$ and

(ii) A detects a particle coming from b and B detects a particle coming from a: the amplitude for this is, $\sim e^{ip.x_2}\, e^{ip.y_2}$. The amplitude for coincidence is proportional to the sum of the above two amplitudes, which is,

$$\sim e^{ip.(x_1+y_1)} + e^{ip.(x_2+y_2)}.$$

The rate of coincidence is $\propto |\text{amplitude}|^2$, and is therefore,

$$\sim [2 + e^{ip.\{(x_2-x_1)+(y_2-y_1)\}} + e^{-ip.\{(x_2-x_1)+(y_2-y_1)\}}].$$

Note that, $(x_2 - x_1) + (y_2 - y_1) = \Phi D$, and the rate of coincidence is therefore, $\propto 2(1 + \cos pR\Theta)$. As the coincidence rate is measured as a function of Θ, from successive maxima occurring at $pR\Theta = 0, 1, 2 \cdots$ one estimates R, the dimension of the source. The criterion for path ambiguity is decided by the uncertainty relation $\Delta p \Delta x \leq \hbar \approx 197$ MeV fm. This means that to achieve a simultaneous detection of two identical mesons within $\Delta t \sim 1$ fm/c, the mesons must not exceed each other in their momentum values by more than a few hundred MeV. Experimentally this condition may be achieved,

(i) by studying the interference as a function of difference of a suitable phase-space variable, say momentum magnitudes of two identical mesons $\Delta\,|\mathbf{p}| = ||\mathbf{p_1}| - |\mathbf{p_2}||$,

(ii) by studying the interference as functions of magnitudes of difference of transverse and longitudinal components of the mesons, $q_t = ||\mathbf{p_{1t}}| - |\mathbf{p_{2t}}||$, and $q_l = ||\mathbf{p_{1l}}| - |\mathbf{p_{2l}}||$,

(iii) by studying the interference as function of four-momentum transfered squared, $q^2 = -(q_1 - q_2)^2$.

For a coherent source of particle emission, the production probabilities for individual mesons $P(\mathbf{p_1})$ and $P(\mathbf{p_2})$ are independent of each other. Whereas, for a chaotic source these probabilities are correlated, and the degree of correlation is measured by a two-particle correlation coefficient defined by,

$$R_2(\mathbf{p_1}, \mathbf{p_2}) = C_2(\mathbf{p_1}, \mathbf{p_2}) - 1 = \frac{P(\mathbf{p_1}, \mathbf{p_2})}{P(\mathbf{p_1})P(\mathbf{p_2})} - 1.$$

$R_2(\mathbf{p_1}, \mathbf{p_2}) = 0$ for a perfectly coherent source, and $R_2(\mathbf{p_1}, \mathbf{p_2}) = 1$ for a fully chaotic source. Experimentally (i) R_2 or C_2 is measured as a function of phase-space variable as mentioned above, (ii) an analytical expression for C_2 is chosen that depends on source dimension R and freeze-out time τ, and (iii) experimental values of C_2 are fitted with that analytical expression. One choice for the analytic form for C_2 is,

$$C_2 = A\left[1 + \lambda e^{-q^2R^2}\right],$$

where λ is called the chaoticity parameter: $\lambda = 0$ means coherent emission while $\lambda = 1$ signifies a chaotic emission of mesons. To extract the three dimensional information about the source size, multidimensional Gaussian fit has been made to the relative momentum correlations in the sideward, outward and longitudinal directions with corresponding radii (R_{side}, R_{out}, R_{long}) serving the role of fit parameters, the choice for C_2 being,

$$C_2 = A\left[1 + \lambda e^{-(q.R)^2}\right].$$

There are however, other choices for C_2 that appropriately incorporate the dynamics of relativistic AB collision.

Some experimental observations on Interferometry

Interferometric measurements on pions and kaons were carried out both at BNL-AGS and CERN-SPS. Experimentally the correlation coefficient C_2 is measured by normalizing the two particle probability function $P(\mathbf{p_1}, \mathbf{p_2})$, not with respect to single particle probabilities like $P(\mathbf{p_1})$, $P(\mathbf{p_1})$. Instead, a two particle probability function that does not contain any BE-correlation, is used. Such an uncorrelated function is obtained by looking at the production probability of two charged mesons with unlike charges, or by detecting two neutral mesons coming from two different events. Results on three dimensional analysis obtained by the WA80 and NA35 collaborations [38] showed that, (i) transverse radii at mid-rapidity increase with centrality of the collision, (ii) source radii for kaons are consistently smaller than those for pions, (iii) larger radii are obtained for larger collision systems, and (iv) the source radii depend on the sum of pair momentum defined by, $p_t = p_{1t} + p_{2t}$. In central Pb+Pb collisions at 158A GeV incident energy, $5 - 7$ fm large transverse root mean square (rms) radii of pion source were observed [39]. This is almost twice the geometrical transverse rms dimension of the colliding nuclei. This indicates that the interferometric dimensions represent a later stage of the collision that has undergone an expansion process. Smaller source radii for kaons (in comparison with pions) indicate that kaons probably freeze out of the collision region earlier than the pions. The p_t dependence of source radii indicates the existence of a collective expansion before the freeze out period. At RHIC large source size and longer duration time for particle production are expected to be achieved. Two particle correlations were measured by the STAR and the PHENIX collaborations [40]. Once again in Au+Au collisions at $\sqrt{s_{NN}} = 200$ GeV the pion source size was of the same order of magnitude as the Pb+Pb collisions. The ratio R_{out}/R_{side} is expected to be significantly different from unity for a prolonged source lifetime. But the observations show that $R_{out}/R_{side} \sim 1$. Interferometric results in general are in conformity with an expanding fireball scenario, where local thermal equilibrium and independent longitudinal and transverse motion are assumed.

1.6.5 Strangeness Production

An enhancement in the number of strange quarks and antiquarks can be treated as one of the signals for QGP formation [41]. As one moves from the pre-equilibrium stage to a thermalized plasma which is also chemically equilibrated, interactions among the constituents belonging to different species of particles present within the system take place. For a thermally equilibrated system the energy-momentum gained by one of the constituent particle is compensated by a corresponding loss of the other, so that the overall distribution remains unaltered. For a chemically equilibrated system gain in the number density of one species is balanced by a corresponding loss through some other (reverse, pair production/annihilation processes etc.), so that the number density of each species remains same. Such a thermally and chemically equilibrated state is characterized, respectively, by a temperature T and chemical potential μ. The occupation probabilities for the quarks (antiquarks) are guided by the Fermi-Dirac type of functions, whereas, the same for the gluons are governed by the Bose-Einstein type of distributions. In an early stage of the AB interaction, where the strangeness content is negligibly small, the system is dominated mainly by lighter quarks (u, d), antiquarks $(\bar{u}, \bar{d})$ and gluons. As thermal and chemical equilibriums are gradually established through interactions among these particles, strange quarks and antiquarks are copiously formed through processes like, (i) $u\bar{u} \rightarrow s\bar{s}$, (ii) $d\bar{d} \rightarrow s\bar{s}$, and (iii) $gg \rightarrow s\bar{s}$, resulting in a change in the overall strangeness content of the plasma. At high collision energy, where the colliding nuclei are substantially transparent to each other, the nuclear fragmentation regions will be well separated from the central baryon free gluonic plasma region, where the net baryon density can be taken as zero, $\left(\mu_{u,\bar{u}} = mu_{d,\bar{d}} = \mu_{s,\bar{s}} = 0\right)$. With the help of perturbative QCD, one can estimate the number density of each quark (antiquark) species provided the QGP is sufficiently long lived to reach thermal and chemical equilibrium. It is possible to show that the density of all quarks and antiquarks are nearly same when a temperature T equivalent to the same order of the strange quark effective mass (m_s) is achieved. Under such circumstances enhancement of strange matter is manifested through production of strange mesons $(K^{\pm}, K^0, \bar{K^0})$, strange hyperons $(\Lambda, \Sigma, \Xi, \Omega)$, and strange antihyperons $(\bar{\Lambda}, \bar{\Sigma}, \bar{\Xi}, \bar{\Omega})$. On the other hand at comparatively lower collision energy (typical of the BNL-AGS energy), there will be enough stopping between the colliding nuclei, leading

to a baryon rich quark matter having nonzero chemical potential for each of its quark constituents restricted by the condition $\mu_{u,d} > \mu_{s,\bar{s}} > \mu_{\bar{u},\bar{d}}$ near the transition temperature. In a baryon rich system strangeness production is enhanced due to Pauli blocking of light quark production. It's known that, the volume swept out by the cross-section of interaction times the relative velocity between two particles gives us the rate of a particular interaction. One can use this fact to determine the chemical equilibration time (τ) to reach from an initial zero strange quark density to a finite equilibrium density say, n_s. The typical time scale within which a heavy-ion interaction takes place is about $\sim$ 10 fm/c. The estimated value of τ is about 10 fm/c if a temperature of 200 MeV is to be reached. Therefore, it may be concluded that the chemical equilibrium may not be achieved at a plasma temperature $\sim$ 200 MeV, but probably at a higher temperature e.g, $\sim 300 - 400$ MeV.

Some experimental observations on strangeness production

Strange quarks and antiquarks produced pairwise, hadronize either through associated production $NN \rightarrow N\Lambda K^+$ or through production of kaon pairs $NN \rightarrow NNK^+K^-$. If the net baryon density is high associated production of Λ is favored, which in comparison to production of kaon pairs also has a lower threshold energy. Thus the K^+/K^- ratio within the mid-rapidity region can be considered as a signature for strangeness enhancement. Large values of K^+/K^- ratio have been reported by the E802 collaboration in Si+Si, Si+Au and Au+Au collisions, respectively, at 14.6, 14.6, 11.7A GeV incident beam energies [42]. The measured K^+/K^- ratio varied between $5 - 7$ with little dependence on the number of participating nucleons. There was however variation in the ratio with the beam energy. In a quark clustering scenario a $\bar{u}d$ di-quark in an environment of high baryon content, is more likely to find an $\bar{s}$ and form a $\bar{\Lambda}$, than to find another $\bar{u}$ and form a $\bar{p}$. Hence the $\bar{\Lambda}/\bar{p}$ abundance ratio can also serve as a sensitive parameter to study strangeness enhancement. The E864 and E878 experiments [43] measured this ratio around $p_t \sim 0$. The ratio was found to be significantly above unity for the most central Au+Pb collisions at 11.5A GeV incident energy. A ratio greater than unity was also obtained in the E917 experiment [44].

At SPS enhanced production of hyperons (Λ, Ξ, Ω) and antihyperons ($\bar{\Lambda}$, $\bar{\Xi}$, $\bar{\Omega}$, was observed and the ratio of each strange baryon and its antibaryon was analyzed by the NA36,

WA85 and WA97 collaborations. The enhancement in strange baryon production was found to be larger than antibaryons. This asymmetry is probably due to large net baryon content at the central rapidity region. The WA97 and NA57 experiments were designed to study the production of strange and multistrange particles in Pb+Pb collisions at the SPS. WA97 collected data from p+Be, p+Pb and Pb+Pb collisions at a beam momentum of 158A GeV at the SPS [45]. The Pb+Pb data have been divided into four centrality classes according to the multiplicity of charged particles (n_{ch}). The yield (multiplicity per event) per unit rapidity of the various particles is determined by integrating the invariant cross section over the full p_t range and over one unit of central rapidity centered around the midrapidity ($y_{cms} = 0$). All yields including those of negative particles (mostly π^-) are enhanced. This is the pattern expected for QGP formation.

The STAR Collaboration studied the production of strange and multistrange baryons in Au+Au collisions and pp interactions at $\sqrt{s_{NN}} = 200$ GeV [46]. The Au+Au event sample consisted of 1.5×10^6 central collision triggers and 1.6×10^6 minimum bias triggers. The pp results were obtained from 6×10^6 minimum bias events. Particles were identified through reconstruction of charged daughter decay particles in a TPC. After suitable cuts the mid-rapidity yield, enhancements for Λ, $\bar{\Lambda}$, Ξ^-, $\bar{\Xi}^+$, Ω^-, $\bar{\Omega}^+$ and inclusive p, as a function of participating nucleon number were plotted. A definite enhancement in the yields over that expected from participating nucleon number scaling, was observed for all the particles mentioned. In SPS the difference in the scale of enhancements in baryon and anti-baryon was due to the existence of a net nonzero baryon number. However, at SPS the ratio of anti-baryon yield to baryon yield varied as a function of participating nucleon number. This possibly indicates different production / annihilation mechanisms for (anti)particles at SPS and at RHIC.

1.6.6 Elliptic flow of hadrons

When two nuclei interact centrally there is a cylindrical symmetry in the colliding system. As a result the azimuthal emission of the hadrons produced exhibit more or less a cylindrically symmetric radial flow. For finite impact parameter ($b \neq 0$) this cylindrical symmetry is destroyed and it is reflected in the emission pattern of the final state hadrons. The elastic collisions between the nucleons change the direction of the particles. If these

collisions are sufficiently frequent, pressure builds up and a collective flow occurs preferentially along the direction of the largest pressure gradient. To determine any preferential emission one has to first define a reaction plane constructed by the beam axis and the impact parameter for a particular interaction. At lower energies (a few GeV per nucleon) the centrally produced matter and the participating nucleons try to escape preferentially in an orthogonal direction to the reaction plane, while the spectator nucleons from both the projectile and the target block their path, leading to a so called "squeeze out" effect. At higher energies the passage time of the spectator nucleons is shrunk by the Lorentz factor given approximately by $2R/\gamma_c$, where R is the radius of individual nuclei, and γ_c is the Lorentz factor in the *cms*. The particle production process takes such a time, that the passage time is not completely irrelevant. As a result the centrally produced matter is initially squeezed-out orthogonal to the reaction plane. But with the spectator nucleons escaping from the reaction zone, the block disappears, and the almond shaped geometry of the overlap region (due to finite b) favors central flow parallel to the impact parameter. The orientation of the flow of this matter is decided by the relative strength of the initial compression and the subsequent expansion time. The anisotropic flow is measured by expanding the particles' azimuthal momentum distribution with respect to the reaction plane in terms of a Fourier series, the coefficients v_n of each term in the expansion characterizing the flow. For each event these Fourier coefficients v_n for different harmonics n are calculated as,

$$v_n = < \cos n.(\phi - \psi_n) >$$

where φ denotes the transverse momentum emission angle of one particle,

$$\phi = \tan^{-1} \frac{p_y}{p_x},$$

and the reaction plane angle ψ_n is estimated on the event-by-event basis. A nonvanishing coefficient of the first harmonic with respect to this plane essentially reflects the directed transverse flow (the so called "bounce-off" effect invented at the Bevalac), and this can be used to determine the reaction plane. Whereas, the second coefficient v_2 of the second harmonic quantifies the elliptic flow [47]. The ellipticity in spatial coordinates comes about because of the asymmetric overlap of the two colliding nuclei in a non-central collision, and from the pressure gradient developed in the almond shaped collision zone. The initial transverse coordinate space anisotropy of the collision zone or eccentricity

$e =< (y^2 - x^2)/(y^2 + x^2) >$ is converted, via hadronic or partonic interactions into an azimuthal momentum space anisotropy. Because of a large amount of rescattering, elliptic flow self-quenches during the expansion period of the collision zone. Therefore, in order to achieve relatively large v_2 a fast thermalization is required. Thus elliptic flow carries information about the pressure and hence about the equation of the state as well as the degree of thermalization achieved by the system. Detailed calculations show however that the dependence on the equation of state is rather weak. It has been argued that it is necessary for the pressure to build up at early times to have a maximal effect. What is meant by "early" time however is not immediately obvious. One should keep in mind that the flow takes time to develop, a time typically of the order of the size of the system. Furthermore, it is easy to see that as one decreases the time at which the hydrodynamical motions starts, the pressure increases but that does not lead necessarily to an increase of the flow; indeed the inertia of the hydrodynamical equation increases proportionally to the pressure. In fact detailed calculation shows that no visible variation of v_2 follows when the initial time is changed from 1 to 2 fm/c. Hydrodynamics appears to explain nicely the variation of v_2 with p_t at small p_t ($p_t < 1$ GeV/c) as well as the mass dependence of the effect, provided it takes into account a phase transition from partonic to hadronic degrees of freedom. This sensitivity to the equation of state underlies the importance of elliptic flow for the understanding of hot and dense nuclear matter, including a possible creation of QGP. It has also to be noted that, the flow of heavier particles is less sensitive to the freeze-out temperature, and therefore, in comparison with the lighter particles it directly reflects conditions at the early stage of the collisions.

A distinctively new feature for azimuthal anisotropy stems from the high p_t results offered by the hard scattering AA collisions at RHIC. A colour charge propagating through a colour charged medium suffers induced radiative energy loss in the same way an electrically charged particle looses energy as it traverses an extended electrically charged medium. Due to interference effects the net energy loss within the medium is proportional to the traversed path length square. However, AB collisions do not offer an infinite homogeneous medium, and the above square law has to be modified due to finiteness of medium size as well as fluctuating local energy density. Partons fragment into hadronic jets as the central high-energy density region expands and reaches freeze out temperature.

If now a jet is created near the periphery of the central region, one of the leading partons may escape the colour charged central fireball into free space without much interaction with the medium. Whereas, its opposite side counterpart will have to travel almost the entire extent of the central fireball, thus loosing much of its energy which results into the quenching of the associated hadronic jet. Since the energy loss increases with the length of traversed material, one expects this effect to soften the p_t distribution in the direction perpendicular to the collision plane.

Some experimental observations on elliptic flow

The STAR collaboration [48] observed elliptic flows in pion, kaon, proton and lambda spectra. They found that v_2 values are large and are in good agreement with hydrodynamic models for ultra-relativistic heavy-ion collisions. Surprisingly their data also showed that the elliptic flow persists to high momentum and then it saturates. This applies to $\sqrt{s_{NN}} = 130$ GeV as well as for 200 GeV and to all centralities. The flow pattern follows the predictions of hydrodynamics up to about $p_t \approx 2$ GeV/c. Beyond this point hydrodynamics predicts that the curves should continue to rise. In contrast the elliptic flow was found to saturate. Thus, there is some mechanism at high p_t that allows the asymmetry in the emission pattern to persist to the highest measured transverse momenta. This mechanism may be due to partonic energy loss or some other exotic process. However, at $p_t > 6$ GeV/c non-flow effects could have a considerable contribution to the observed v_2 values.

Study of elliptic flow was also performed by the PHENIX Collaboration [49]. The measurements were made at $\sqrt{s_{NN}} = 200$ GeV with the PHENIX detector at the RHIC. Approximately 6.5×10^8 Au+Au and 8.0×10^7 Cu+Cu minimum-bias collisions were analyzed. The differential elliptic flow measurements for charged hadrons were obtained with the reaction plane method. The value of v_2 against p_t was plotted in both Au+Au and Cu+Cu collisions for different centralities. The v_2 values increased as the collisions become more peripheral and as the p_t increased. For each centrality selections these data were tested for the eccentricity scaling by dividing the differential values of v_2 by the v_2 integrated over a p_t range $0.3 - 2.5$ GeV/c. The hydrodynamic model predicts that this ratio should be constant with centrality and should be independent of the colliding

system. These scaled values are found to be independent of the colliding system size and show essentially perfect scaling for the full range of centralities. The v_2 are also in accord with the scale invariance of perfect fluid hydrodynamics, which suggests that rapid local thermalization is achieved.

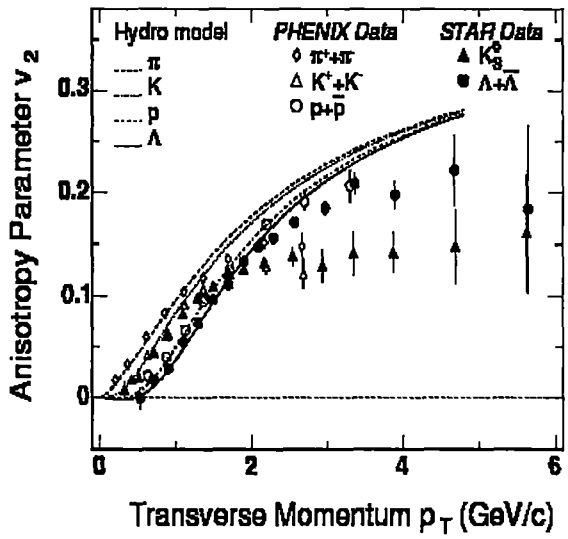

Figure 1.19: Anisotropy parameter v_2 measured in RHIC experiments as a function of transverse momentum p_t.

The elliptic flow of Λ hyperons has been measured by the NA49 experiment in semicentral Pb+Pb collisions at 158A GeV/c [50]. The analyzed sample consists of 3×10^6 semicentral Pb+Pb events with on line trigger selection of the 23.5% most central collisions. The acceptance of Λ hyperons covers the range $p_t \approx 0.4 - 4$ GeV/c and $y \approx -1.5 - +1.0$. The final statistics in Pb+Pb collisions consists of about 10^6 Λs. The plot of azimuthal distribution of Λ particles with respect to the estimated event plane for real and mixed events and fits of the function in the form of a Fourier series with two parameters v_2 and v_4. The distributions exhibit a strong correlation for real events and no correlation for mixed events. The correlation significantly increases with transverse momentum and also with impact parameter. The p_t integrated Λ elliptic flow exhibits no significant dependence on rapidity and a weak dependence for protons. The pronounced flatness of $v_2(y)$ suggests that event samples can be directly compared even in different rapidity

ranges as long as Λ-s are measured near midrapidity. The collaboration also measured the p_t dependence of rapidity integrated elliptic flow of Λ-s for two centrality ranges (for $\sigma/\sigma_{tot} = 12.5-23.5\%$ and $5.0-12.5\%$). They observed that the v_2 parameter significantly increases with transverse momentum - the rise is stronger for more peripheral events. For mid-central collisions NA49 elliptic flow grows linearly with p_t up to $\sim$ 2 GeV/c. The elliptic flow for pions, Λ hyperons and protons are also measured by the NA49 experiment. The elliptic flow grows linearly with p_t for all species but the rise for pions starts from $p_t = 0$ while for protons and Λs it starts from $p_t = 0.5$ GeV/c. All features observed by the NA49 collaboration are well reproduced by the blast wave parametrization and the hydrodynamic model. The increase of v_2 with p_t is weaker at SPS than at RHIC energy and is significantly overpredicted by the hydrodynamical calculations.

The CERES collaboration [51] measured elliptic flow as a function of p_t of $\pi^{\pm}$ and low-p_t protons and Λ and K^0_S particles from Pb+Au collisions at 158A GeV/c. For the flow analysis, they used 30×10^6 Pb+Au events at 158A GeV/c collected in the year of 2000 data taking period. Of these, 91.2% were triggered on $\sigma/\sigma_{tot} \leq 7\%$, and 8.3% events with $\sigma/\sigma_{tot} \leq 20\%$. Due to small statistics of strange particles, the differential elliptic flow analysis was performed for only two centrality classes. The huge statistics of $\pi^{\pm}$ allowed to perform the differential elliptic flow analysis in six centrality bins. They studied the p_t dependences of v_2 for three particle species. An increase of the elliptic flow magnitude vs p_t for all three particle species were observed. The elliptic flow results are compared with the hydrodynamical calculations. The model prediction with the lower freeze-out temperature of $T_f = 120$ MeV overpredicts the data, while rather good agreement can be achieved with a higher freeze-out temperature of $T_f = 160$ MeV (this is however not the preferred value considering the proton p_t spectra). A comparison of the CERES data to results from NA49 at same energy ($\sqrt{s_{NN}} = 17$ GeV) and to STAR results at $\sqrt{s_{NN}} = 200$ GeV is also performed. The NA49 and CERES data are in very good agreement. After rescaling the STAR results to the centrality used in the CERES experiment, the v_2 values measured at RHIC are $15-20\%$ higher due to the higher beam energy. From the comparison of the elliptic flow magnitude of the $p^{\pm}$, K^0_S, low momentum protons, and Λ measured by CERES a mass ordering effect is observed. At small p_t up to $p_t \approx 1.5$ GeV/c, $v_2(\Lambda) < v_2(K^0_S) < v_2(p^{\pm})$. In high p_t region (above ≈ 2 GeV/c) the

tendency was opposite.

1.6.7 Charged Particle Ratio Fluctuations

According to Jeon and Koch the event by event fluctuations of the ratio of the positively charged and the negatively charged pions $\left(\frac{h^-}{h^+}\right)$ provides a signal of the QGP. The arguments and the methodology are given in their pioneering paper [52], that is summarized below. The idea comes from the fact that in order to detect the colour degree of freedom one generally measures

$$R_{e^-e^+} \equiv \frac{e^-e^+ \rightarrow \text{hadrons}}{e^-e^+ \rightarrow \mu^-\mu^+}.$$

If the fundamental degrees of freedom are hadrons the value of $R_{e^-e^+}$ would have been very different from the simple counting given by,

$$R_{e^-e^+} = n_c \sum_q Q_q^2,$$

where n_c is the number of colour degrees of freedom and Q_q is the charge of each quark flavour. Jeon and Koch suggested that the event-by-event fluctuations of hadron number belonging to different charge signs $(\frac{h^-}{h^+})$ can in a similar manner determine whether the underlying degrees of freedom are quarks and gluons or hadrons. They argued that the fluctuation in the net charge depends on the square of the charges of the constituent particles (1/3 for quarks, 0 for gluons, and 1 for hadrons), and hence depends on the phase the hadrons originate from. It is obvious that the ratio $F = Q/N_{ch}$ is a natural choice to measure the net charge fluctuation, where $Q = N_+ - N_-$ is the net charge and $N_{ch} = N_+ + N_-$ is the total charge multiplicity. Here $N_\pm$ denotes the positive (negative) multiplicity. However, instead of using F Jeon and Koch used the charge ratio R given by,

$$R = N_+/N_- = \frac{1+F}{1-F}.$$

When $\langle N_{ch} \rangle \gg \langle Q \rangle$ one can say that $\mid F \mid \ll 1$, as it is the case for high multiplicity AB events. Expanding R in terms of F yields

$$R \approx 1 + 2F + 2F^2,$$

and one can then write

$$\left\langle \delta R^2 \right\rangle = \left\langle R^2 \right\rangle - \langle R \rangle^2 \approx 4 \left\langle \delta F^2 \right\rangle.$$

Using the definition of F one can see that,

$$\langle \delta F^2 \rangle = \frac{\langle Q \rangle^2}{\langle N_{ch} \rangle^2} \left\langle \left(\frac{\delta Q}{\langle Q \rangle} - \frac{\delta N_{ch}}{\langle N \rangle_{ch}} \right)^2 \right\rangle.$$

When the average ratio is very much different from 1, the fluctuation is dominated mainly by the fluctuation in the smaller quantity. In case of relativistic heavy-ion collision it is expected that the fluctuation in F will therefore, be dominated by the fluctuation in Q. Hence

$$\langle \delta F^2 \rangle \approx \frac{\langle \delta Q \rangle^2}{\langle N_{ch} \rangle^2},$$

and the quantity

$$\langle N_{ch} \rangle \langle \delta R^2 \rangle = 4 \langle N_{ch} \rangle \langle \delta F^2 \rangle \approx 4 \frac{\langle \delta Q \rangle^2}{\langle N_{ch} \rangle^2}$$

has therefore, been considered as the main observable. If the fundamental degree of freedom is a pion gas the value of $\langle \delta Q \rangle^2 / \langle N_{ch} \rangle^2$ is slightly greater than unity and hence the ratio

$$D_{had} \equiv \langle N_{ch} \rangle \langle \delta R^2 \rangle \big|_{hadron} \approx 4.$$

On the other hand for a QGP the ratio

$$D_{QGP} \equiv \langle N_{ch} \rangle \langle \delta R^2 \rangle \big|_{QGP} \approx 0.75.$$

It is found that the value D_{QGP} is less than almost by a factor 5 than the value of D_{had}, which one may consider as a suitable signal of QGP formation. Due to several factors the extent of charge fluctuation may either increase or decrease. As for example, hadronization and phase-space cut enhance the ratio D_{had}/D_{QGP} whereas, resonance contributions lower the value of D_{had}.

Some experimental observations on charge fluctuation

STAR Collaboration [53] investigated the charged particle fluctuations in Au+Au collisions at $\sqrt{s_{NN}} = 130$ GeV. Measurements on dynamical fluctuations were performed for inclusive charged particle multiplicities, as well as for identified charged pions, kaons, and protons. They study event-by-event fluctuations of conserved quantities at near-zero rapidity in the center-of-mass rest frame (midrapidity). The data used are from minimum bias and central trigger samples of Au+Au at $\sqrt{s_{NN}} = 130$ GeV acquired by the STAR experiment during the first operation of the relativistic heavy-ion collider. About 1.8×10^5

minimum bias and 8×10^4 central trigger events were used in this analysis. The centrality of the collisions is estimated from the total charged particle track multiplicity detected within the TPC in the η range $\eta \leq 0.75$. Eight contiguous centrality bins based on the fraction of triggered events were used. Specifically, fluctuations in the difference in the number of positively and negatively charged particles (multiplicities) measured within a fixed rapidity range were analyzed. The parameter used for the purpose was,

$$\nu_{\pm} = \left\langle \left(\frac{N_+}{\langle N_+ \rangle} - \frac{N_-}{\langle N_- \rangle} \right)^2 \right\rangle,$$

where N_+ and N_- are multiplicities of positive and negative particles, respectively. The magnitude of the variance ($N_{\pm}$) is determined by both statistical and dynamical fluctuations. Statistical fluctuations arise due to the finite number of particles measured, and can be readily calculated based on expectation values for Poisson distributions. The intrinsic or dynamical fluctuations are defined and evaluated as the difference between the measured fluctuations and the statistical limit,

$$\nu_{\pm,dyn} = \nu_{\pm} - \nu_{\pm,st}.$$

STAR Collaboration studied the dynamical fluctuations $\nu_{\pm,dyn}$ of the net charge measured in the η range $|\eta| \leq 0.5$, as a function of the total multiplicity M measured in the η range $|\eta| \leq 0.75$. They obtained the value of dynamical fluctuations of the 5% most central collisions as to $\nu_{\pm,dyn} = -0.00236 \pm 0.00006(st) \pm 0.00012(sys)$. It is found that the dynamical fluctuations are finite and negative which is a clear indication that positive and negative particle production are correlated within the η range considered. One may also observe that the strength of the dynamical fluctuations decreases monotonically with increasing collision centrality. This can be understood from the fact that more central Au+Au collisions involve an increasing number of NN sub-collisions. The two-particle correlations are thus increasingly diluted and the magnitude of $\nu_{\pm,dyn}$ is effectively reduced. The results shows a good agreement with the PHENIX measurements [54]. The results indicate that the dynamical fluctuations for pions are approximately of the same magnitude as for inclusive non-identified charged particles. The dynamical fluctuations of the charged kaons and p, $\bar{p}$ are also finite. Their sizes (absolute value) are in fact larger than the dynamical fluctuations measured for pions and for inclusive non-identified charged particles.

1.7 Particle Density Fluctuations

History shows that the study of fluctuation has often triggered significant advances in physics. Investigation of dynamical fluctuation in the density distributions of particles coming out of high-energy interactions has till date remained one of the most popular tools to study the mechanism of multiparticle production. Efforts have been made to interpret these fluctuations observed within narrow phase-space intervals in AB collisions, in terms of conventional processes like the Bose-Einstein correlation, intranuclear cascading, jet structure, resonances etc., or more exotic process like thermal phase transition. It has been observed that often the produced particles prefer correlated emission. The reason may be a trivial matter of chance, it may be due to the conservation laws associated with kinematic variables, it may be due to some other nontrivial dynamical reason, or it may be a combination of any two and/or all three of the above. Various methods have been devised to separate out the statistical noise arising out of finite number of particles per event from the nontrivial fluctuations arising due to unknown dynamics, if there is any. It would be interesting to identify the origin of the dynamical part of the fluctuation (even through that is speculative in nature), either in terms of any known dynamics or from the perspective of a possible new state such as the QGP. Many particle correlation leads to clustering of particles within narrow regions of a particular phase-space, that would ultimately manifest itself as large fluctuations in the corresponding distribution. The fluctuations may appear either as sharp peaks often called spikes, or as sharp minima called the voids, in the distribution. The existence of spikes may provide crucial information about the substructure in space-time of collision region like, formation of hot spots of hadronic matter. The study of fluctuation is generally carried out in the central particle producing region, because this region carries more information regarding the dynamics of particle production than the other fragmentation regions. In chapter three to five different phenomenological and experimental issues related to the dynamical fluctuation in particle density distribution will be discussed in details. In the following subsections however, a brief review of some of the experimental facts related to this particular topic have been furnished. As far as experimental facts are concerned the discussion is restricted only to some of the AB interactions.

1.7.1 Intermittency

The factorial moment of order q defined for the multiplicity n as

$$f_q = n(n-1)\cdots(n-q+1),$$

is capable of suppressing the Poisson type of statistical noise. Factorial moments of the observed distribution (that contains both a dynamical part and a Poisson type statistical part) are actually equivalent to the ordinary moments of the underlying dynamical part of the distribution, irrespective of its exact analytic form. The importance of factorial moments in analyzing particle distributions with diminishing phase-space interval size was first recognized by Bialas and Peschanski. The technique was then applied to a few very high multiplicity JACEE [55] events initiated by cosmic ray nuclei of extremely high-energy. Bialas and Peschanski [56] also observed that the factorial moments defined for a particular bin (phase-space interval) multiplicity n_m, and normalized by the average bin multiplicity $< n_m >$ actually scale with the bin size δX following a power law like,

$$F_q \sim (\delta X)^{-\phi_q},$$

where the exponent $\phi_q (> 0)$ is called the "intermittency index". Normalized factorial moments F_q are particularly sensitive to large density fluctuations at various scales of phase-space interval (bin) size, and they have been found to be very useful to detect large nonstatistical fluctuations as well as the pattern of such fluctuations.

Experimental Results on Intermittency

An analysis on event-to-event fluctuations in hh collisions comparing rapidity distributions of single events with the corresponding sample averaged distribution was performed by Ludlam and Slansky [57]. They observed that the clustering effects in longitudinal phase-space indicate a structured density. After this a series of results confirmed large concentration of particle number in small rapidity regions for single events in cosmic ray experiments, in pp and in pA collisions. The JACEE collaboration [55], the NA22 collaboration [58], the UA5 collaboration [59] have reported high density "spikes" in rapidity space at different resolutions. Using the JACEE data of a single high multiplicity cosmic ray interaction (Si+Ag/Br), the first analysis on intermittency was performed by

Bialas and Peschanski. They were able to show that $\ln < F_5 >$ linearly increased with $-\ln \delta\eta$, thus confirming the scaling law. Thereafter, the intermittency analysis had been repeated in different hadronic, leptonic, hA and AB collisions [60]. All experiments confirmed increase in F_q values with diminishing phase-space interval size, though not necessarily always guided by the strict power law propsoed by Bialas and Peschanski. The phenomenon is often loosely called 'intermittency', that in case of high-energy interactions is related to an intermittent type dynamical distribution of produced particles.

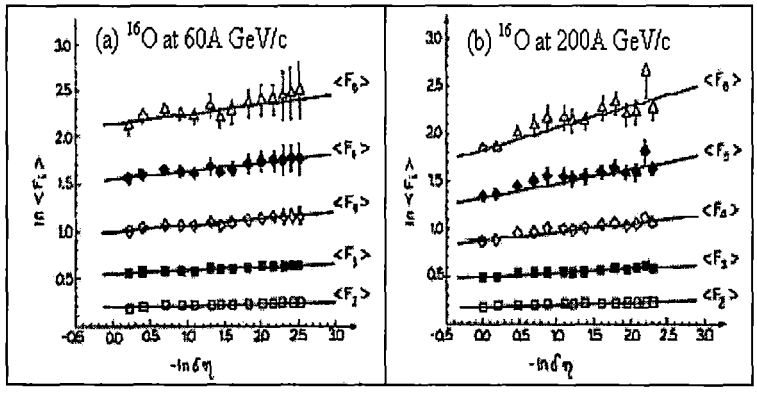

Figure 1.20: First accelerator results on intermittency obtained by the KLM group [61].

The Krakow-Louisiana-Minnesota (KLM) collaboration [61] presented the first experimental evidence for intermittency using accelerator data. The collaboration used nuclear emulsion technique to collect the data. Emulsion pellicles were irradiated by ^{16}O ions at 60A and 200A GeV/c from the CERN-SPS. Fig. 1.20 shows their experimental results, where $\ln < F_q >$ values for $q = 2$ to 6 are found to linearly rise with $-\ln \delta\eta$, instead of a flat behaviour that is expected for independent emission. The intermittency indexes increase with increasing order q, and ϕ_q values are larger in 200A GeV/c interactions than those in 60A GeV/c interactions. The EMU01 collaboration [62, 63] also investigated nonstatistical fluctuations in nuclear interactions in terms of intermittency and scaled factorial moment analysis. For this purpose they used emulsion data on ^{16}O and ^{32}S induced interactions at 200A GeV/c from CERN-SPS. Horizontally exposed emulsion pellicles and vertically exposed emulsion chambers were used to collect the data. For all sets of interactions their analysis was confined mainly to the central η-region. The EMU01

collaboration observed that, small intermittency effects were present in one dimensional (η-space) analysis of their AB data. The Monte Carlo code FRITIOF [64], based on a string fragmentation model, could not reproduce the experimentally observed intermittency results. The EMU01 results were also consistent with the relation, $\phi_q = {}^qC_2\ \phi_2$, which was another requirement of the scaling law introduced by Bialas and Peschanski. A scaling law like $\phi_2 \sim< \rho >^{-1}$ as proposed by Seibert and others [65] was also verified by the EMU01 group for their AB data. The collaboration extended their intermittency analysis to two dimensional (η, φ) space. Though in this case the intermittency effect was found to be stronger, their result on ^{32}S induced interactions was strongly influenced by the γ-conversion [63]. The two dimensional procedure seems to work as a filter for the electron pairs. They concluded that the correlations which gave the largest contributions to the one dimensional moments were not necessarily the same as the one that were contributing to the two dimensional moments.

The WA80 collaboration [66] studied the intermittency phenomenon in very large samples of ^{16}O+C and ^{16}O+Au interactions at 200A GeV/c. The data were collected by using Iarocci type streamer tubes, and the analysis were confined to the central *eta*-region ($2.4 < \eta < 4.0$). Centrality of the collision was decided by using a ZDC. Major observations of this experiment were, observation of intermittency effect for produced particles in AB interactions under consideration, higher intermittency indexes for event samples with intermediate value of impact parameter than in the most central collisisons, and constancy of $\phi_q/[q(q-1)]$ as required by the scaling law of Bialas and Peschanski.

Sarkisyan et al. [67] used streamer chamber data to study the intermittency effect in C+Cu interactions at 4.5A GeV/c obtained from the JINR Synchrophasotron (Dubna). F_q values for $q = 2 - 8$ were determined. From their analysis on ϕ_q and related fractal parameters, they conjectured occurrence of a nonthermal phase transition during the space-time evolution of the AB collision process. According to their study a transition took place from a 'spin glass' phase where the events are dominated by a few dense particle producing regions, to the normal phase that is populated by a large number of not so dense regions.

Using the EMU01 data on Pb + Pb collision at 158A GeV/c (CERN SPS), Tawfik [68] performed an intermittency analysis in 1-d (η/φ) and 2-d (η, φ) spaces. SFM of order

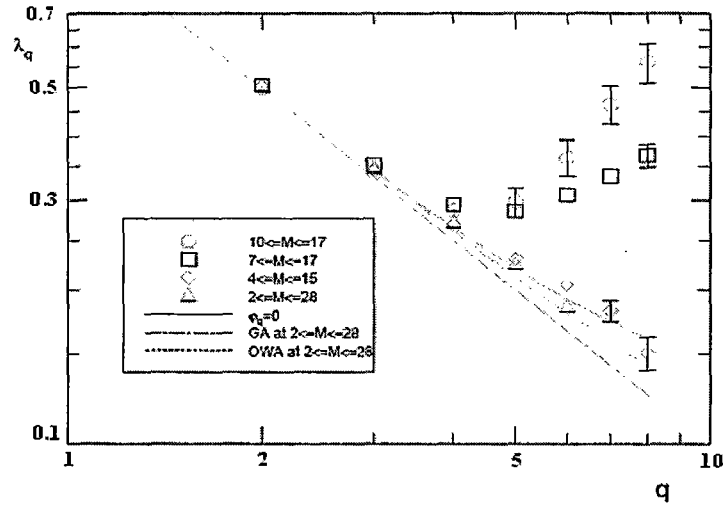

Figure 1.21: Results indicating existence of a mixture of two phases $\lambda < \lambda_c$: normal phase, and $\lambda > \lambda_c$: spin glass phase [67].

$q = 2$ to 6 were obtained as functions of respective phase-space partition numbers M_η, M_φ and $(M_\eta.M_\varphi)$. While in 1-d $2 \leq M_\eta$, $M_\varphi \leq 30$ in 2-d $2 \leq M_\eta$, $M_\varphi \leq 11$. F_q values in 2-d analysis increased faster with certain degree of nonlinearity than in the 1-d analysis. Intermittency exponents obtained from 2-d analysis provided a hint of possible thermal phase transition indicating an onset of QGP formation. The indication of such thermal phase transitions however, was not unambiguous. Tawfik and Ganssauge [69] extended the intermittency analysis to a subsample of very high multiplicity events ($n > 1200$) from the same set of Pb+Pb data and compared the experimental results with the FRITIOF [70], VENUS [71] and RQMD [72] predictions. The 1-d $\eta(\varphi)$-space was partitioned by a large number $M_\eta(M_\varphi) \sim 10^3$, and an upward exponential bending in the variation of F_q was observed. The simulated values of F_q are consistently lower than the experimental values. However, at the largest partition numbers, the same upward bending could be observed in all three simulated samples, though with varying degree.

1.7.2 Self-affinity

Most of the analysis of factorial moments are generally performed for one dimensional distribution of produced particles, while the real process occurs in a three dimensional

space. In a lower dimensional projection of the actual event an implicit averaging process reduces the extent of fluctuation. In a two dimensional α-model Ochs [73] actually showed that, the effects of intermittency were more prominent in higher dimensions. It was also observed in various experiments that, the power law is not exact in higher dimensions. Moreover, in most of the cases the effect of intermittency has been studied by equally dividing different dimensions of phase-space. But the distributions of particles are not isotropic in each dimension, and hence the scaling should be different in different directions. The scaling behaviour incorporating this kind of unequal partitioning in different directions is known as self-affine rather than self-similar scaling. The self-affine structure of phase-space is characterized by a parameter called the Hurst exponent (H), that connects the partition number in a particular dimension with that in the other. The parameter can be obtained from the observed saturation curves of one dimensional $\ln F_q$ distributions. Only a few works have been reported so far, where evidence of self-affinity in multiparticle production is indicated by the data.

Experimental Results on Self-affinity

The anomalous scaling behaviour of 2-d scaled factorial moments for shower particles produced in AB collisions was studied in detail by the EMU01 collaboration [74], using both minimum bias and central interactions of ^{16}O+emulsion at 60 and 200A GeV/c, ^{32}S+emulsion at 200A GeV/c - both from CERN SPS, and ^{197}Au+emulsion at 11A GeV/c collisions from BNL AGS. They analyzed the experimentally obtained second order SFM with different values of Hurst exponent ($H = 0.8, 1.0, 2.0, 3.0$) in the (η, φ) plane. The variation of $\ln < F_2 >$ with respect to $\ln M$ were studied, where M is the 2-d partition number. It can be seen from there investigation that when $H = 1$, the curves bends upward strongly and with increasing value of H this upward bending is weakened. Thus, in order to recover the anomalous scaling of SFM, the phase-space should be divided finer in the longitudinal (η) direction than in the transverse (φ) direction.

Haq et al. [75] investigated the anomalous scaling behaviour of F_2 in (η, φ) plane for shower particles produced in ^{28}Si+emulsion collisions at 14.6A GeV (BNL AGS). The experimental result was compared with the UrQMD generated data. Variation of $\ln < F_2 >$ with respect to $\ln M$ was studied with in the region $H = 1.0$ to 3.0. Their investigation

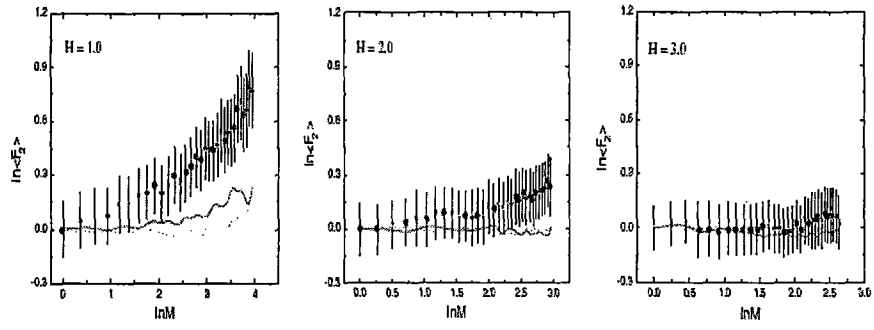

Figure 1.22: Results showing self-affine nature of 2-d intermittency in Si-emulsion interaction at 14.6A GeV/c [75].

shows that, $\ln < F_2 >$ versus $\ln M$ plots for the events simulated using UrQMD model consistently lie below the corresponding experimental plots for $H = 1$, 1.5 and 2.0. For $H = 2.5$ or 3.0 the corresponding separation was not very significant. In order to find out whether the observed behaviour of 2-d second order factorial moment for shower particles is due to interparticle correlation or not, they generated a sample of mixed events of same size and same multiplicity distribution as the experimental one, but without having any interparticle correlation. It was observed that the sample of mixed events also failed to replicate the experimental results. The study on 2-d F_2 for shower particles produced in different AB experiments at CERN SPS and BNL AGS energies showed an upward bending in the variation of $\ln < F_2 >$ as a function of $\ln M$. The bending is stronger for heavier colliding system. An AB interaction can be treated as a superposition of many NN collisions. The observations are consistent with the fact that the number of elementary NN collisions is more for heavier colliding nuclei. This upward bending could, however, be removed by choosing different partition along the longitudinal and transverse directions, i.e., the right value of Hurst exponent.

1.7.3 Factorial Correlators

The study of correlation effect provides information on the dynamics of particle production beyond that obtained from single particle inclusive spectra. While the SFM can be used as a measure of local density fluctuations in phase-space, additional information contained in

the correlation between these fluctuations within an event can be extracted by studying the factorial correlators. These correlators are calculated for a particular phase-space interval size and for a pair of nonoverlapping phase-space regions separated by a distance, say D. The normalized correlator is defined as [56],

$$F_{pq} = \frac{< n_m^{[p]} n_{m'}^{[q]} >}{< n_m^{[p]} >< n_{m'}^{[q]} >}.$$

Here n_m and n'_m are the number of particles respectively, in the m-th and m'-th intervals each of width $\delta\eta$, and $n_m^{[p]} = n_m(n_m - 1)\cdots(n_m - p + 1)$. According to a simple intermittency model (α-model), F_{pq} depends on D but not on $\delta\eta$ and follows a power law like,

$$F_{pq} \propto D^{-\phi_{pq}},$$

while the exponent ϕ_{pq} follows the relation $\phi_{pq} = pq\phi_{11}$.

Experimental Results on Factorial Correlators

Factorial correlators have been studies in the EMU01 experiment [63] using ^{32}S+emulsion data at 200A GeV/c. Growing correlation with decreasing value of D was observed from their plot of $\ln < F_{pq} >$ against $-\ln D$. Islam and Hasan [76]studied the factorial correlators for ^{28}Si+Ag/Br collisions at 14.6A GeV. Their experimental results were compared with the UrQMD generated events. The power-law dependence of $< F_{pq} >$ on the correlation length D was established in their data. The slopes (ϕ_{pq}) were observed to increase with the order (p, q) of correlation. In the region $D < 0.5$ the $< F_{pq} >$ values were also found to be independent of the phase-space interval size. Such features of the data are in agreement with the random cascading α-model. When UrQMD generated event sample was in terms of $< F_{pq} >$, it was found that the model reproduced the bin width independence, but it failed to reproduce the power-law dependence of $< F_{pq} >$ on the correlation length D. Finally in this investigation, the validity of the projection independent scaling relation proposed by Peschanski and Seixas [77] confirmed the presence of intermittent type fluctuations in the data without going into higher dimensional analysis.

Ghosh et al. [78] reported a systematic analysis on correlators for charged particles produced in ^{32}S+Ag/Br interactions at 200A GeV/c. They found a linear relationship between $\ln < F_{pq} >$ and $-\ln D$ at large D, and concluded that the behaviour of correlated

moments at large D was largely controlled by the long range correlations. The exponents ϕ_{pq} obtained from the linear fit of $\ln < F_{pq} >$ and $-\ln D$ with different $\delta\eta$ registered a

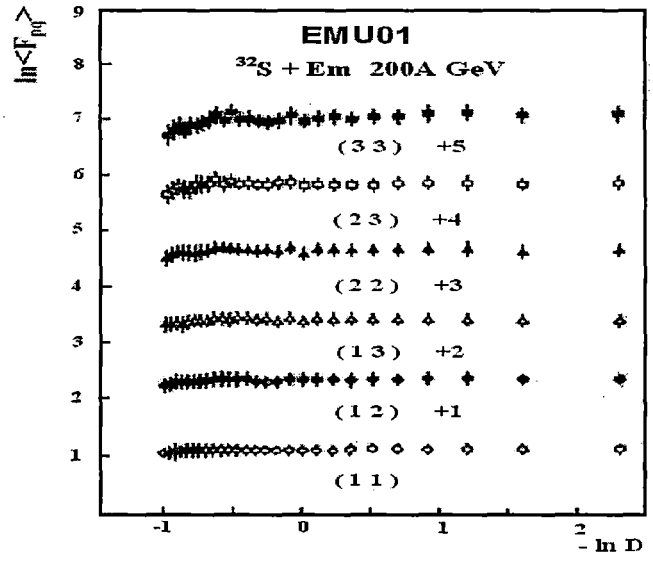

Figure 1.23: EMU01 results on factorial correlators in ^{32}S-Emulsion interaction at 200A GeV/c. For clarity each higher order of F_{pq} has been shifted above the lower one by unit magnitude.

decrease in the exponent value with the decreasing $\delta\eta$. From their measured values of the exponents it was also obvious that for a given bin width $\delta\eta$, the slope values increases with the increase in the product $(p \times q)$. As predicted by the α model they also reported the bin size $(\delta\eta)$ independence of the correlators for a fixed D in the region where power law is obeyed. The exponents are expected to follow the relation $\phi_{pq} = \phi_{p+q} - \phi_p - \phi_q = pq\phi_2$, where the first equality sign is due to the α model. This was also confirmed in the investigation. Validity of the dimension independent scaling relation $F_{11}(D) = 2F_2(2D) - F_2(D)$ confirmed the intermittent nature of particle production of their data sample.

1.7.4 Multifractality

With the help of fractal geometry it is possible to mathematically characterize systems that are intrinsically irregular at all scales. The unique property of the fractal structure

is that if a a small portion of it is magnified, same complexity or regularity as in the whole system is observed. Fractals fall into two categories - geometrically self-similar or uniform fractals, and nonuniform fractals also called multifractals. The fundamental characteristic of multifractality is that the scaling properties are different in different regions of the system. The idea is therefore to construct a formalism that is able to describe systems with local properties of self-similarity. Unlike geometrical or statistical systems, multiparticle production processes poses a special problem due to finiteness of particle multiplicity in an event. Self-similarity, if existent, therefore, cannot persist indefinitely to finer and finer scales of resolution. For a single event of multiplicity n and for a given $\delta\eta$ one can construct a frequency distribution, which approaches the probability distribution $P(\rho, \delta\eta)$ as $n \to \infty$. For finite n the frequency distribution and its moments will be subjected to large statistical fluctuations. Event average is therefore recommended. Multifractality concept is understood only to be one probable cause of the observed density fluctuations. The analysis is based on determining the fractal moments also known as frequency moments (G_q) [79, 80]. The moment of order q for an event is defined as,

$$G_q = \sum_{j=1}^{M} \left[\frac{n_{ij}}{n_i}\right]^q \Theta(n_{ij} - q). \tag{1.8}$$

Here M is the number of intervals into which the entire phase-space has been divided, n_{ij} is the number of particles in the jth bin of ith event, n_i is the total number of particles in the ith event, $\left[n_i = \sum_{j=1}^{M} n_{ij}\right]$, and Θ is a step function which is equal to 1 for $n_{ij} \geq q$ and is equal to 0 for $n_{ij} \leq q$. Inspired by the theory of intermittency, one can also look into the scaling behaviour of the G-moments in the form,

$$G_q(\delta\eta) \propto (\delta\eta)^{-\tau_q} : (\delta\eta \to 0).$$

Such a power law dependence typical for fractals cannot be achieved in experiments, as the limit ($\delta\eta \to 0$) is admissible only mathematically. One cannot therefore, extract the fractal behaviour in its strict sense. However, significant results can still be obtained around the region of experimental resolution. The multifractal index $\tau(q) = -\partial(\ln G_q)/\partial(\ln M)$, the Lipschitz-Holder exponent $\alpha_q = \partial\tau(q)/\partial q$, and the multifractal spectrum function $f(\alpha_q) = q\,\alpha_q - \tau(q)$ are some such parameters relevant to multifractal analysis. The generalized fractal dimensions $D_q = \tau(q)^{dyn}/(q-1) = [q\alpha_q - f(\alpha_q)]\,/\,[q-1]$ for $q > 2$

can also be extracted experimentally.

Experimental Results On Multifractality

Several experiments have been performed to investigate different aspects of multifractal structure of the underlying dynamical distribution of particle densities. Jain et al. [81] performed their multifractal analysis on the η and φ distributions of charged particles produced in several AB interactions induced by ^{32}S at 200A GeV/c, ^{16}O at 60 and 200A GeV/c, ^{28}Si at 14.5A GeV/c, ^{4}He at $\sim$ 140 and $\sim$ 11A GeV, and a proton beam of 800 GeV/c. The experimental results were compared with the VENUS model [71]. Plotting

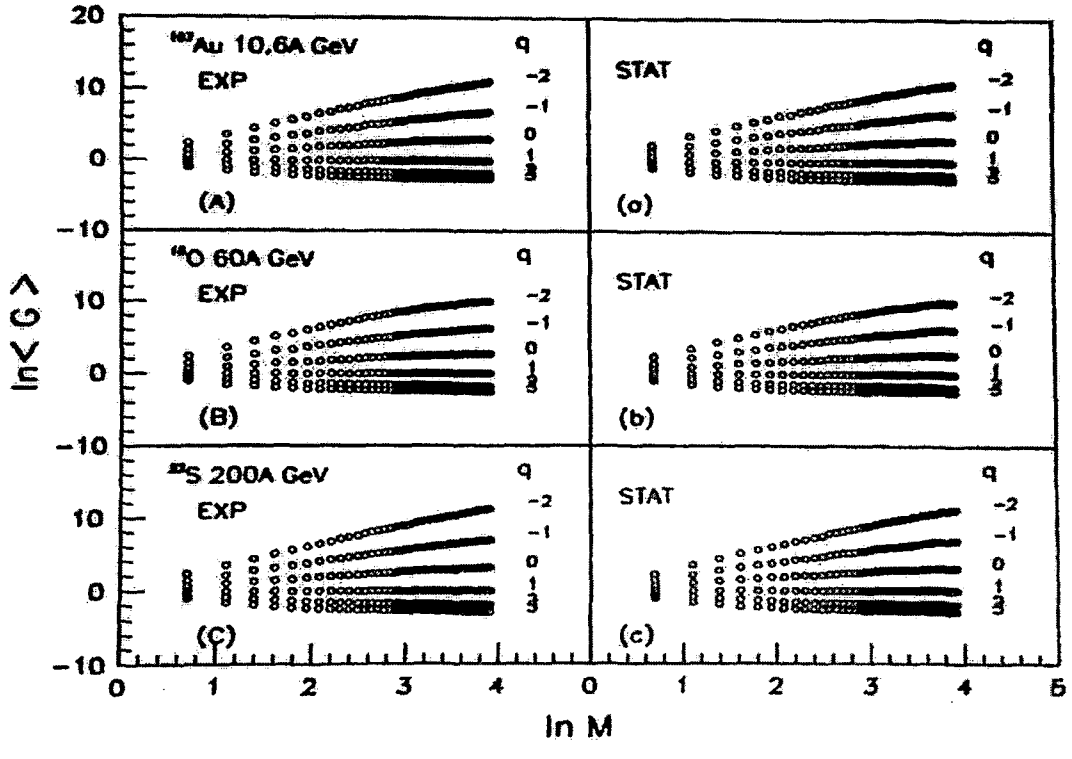

Figure 1.24: Results on multifractal moments obtained by the EMU01 Collaboration [82] on different interactions at SPS energies. Corresponding plots for Monte Carlo generated event sample are also shown.

$< \ln G_q >$ against $-\ln \delta\eta$ and $-\ln \delta\varphi$ the power law scaling was verified for all sets of data, and the fractal parameters obtained therefrom showed expected behaviour consistent with the multifractal theory. The multifractal spectrum was wider for the larger

colliding system, while none of them collapsed to a delta function that confirmed the multifractal structure of the dynamical fluctuation. In terms of multifractal analysis no significant difference between the experiment and the VENUS model. Using ^{197}Au, ^{32}S and ^{16}O induced interactions with emulsion nuclei, respectively, at 10.7A GeV, 200A GeV and 60A GeV, the multifractal analysis was performed by the EMU01 collaboration [82]. They also compared their results with Monte Carlo generated samples. They observed that the experimental $< G_q >$ and generated $< G_q >$ both had very similar forms but still had some differences. They also showed that the behaviour of $< \ln G_q >$ and $\ln < G_q >$ are different. From their analysis one could see that $< G_q >$ did not seem to come only from the contribution of the statistical noise. Their analysis demanded that, the so-called "characteristics for multifractal structure" were obtained for all real data and also for MC data. The behaviour may be described in terms of a purely stochastic model and furthermore the results obtained from real data and MC data were qualitatively same. Thus no definite conclusions on the multifractal structure of particle production in high-energy heavy-ion collisions could be drawn from their analysis.

Sarkisyan et al. [83] reported a fractal analysis of nonstatistical fluctuation in the distribution of produced particles in 4.5A GeV/c C+Ne(Cu) interactions. They used streamer chamber films to collect the data and the exposure was obtained from the JINR at Dubna (Moscow). Both the SFM and the G_q were analyzed to extract fractal parameters and the generalized fractal dimensions D_q. The experimental results on D_q were compared with the predictions of Gaussian approximation, with the assumption of Negative Binomial distribution of multiplicity and prediction of scale invariant branching. As observed in other experiments D_q decreased with increasing q. Multifractal nature of nonstatistical fluctuation was established beyond statistical noise. The authors concluded that their observation was a consequence of nonthermal phase transition in particle production process.

A study of the fractal structure of η distributions of relativistic shower particles produced in ^{28}Si-Ag/Br and ^{12}C-Ag/Br interactions at 4.5A GeV/c was performed by Ahmad and Ahmad [84]. The experimental result was compared with that from events generated by uncorrelated random numbers. While the power law scaling could be verified for both experimental and simulated data, the corresponding fractal parameters behaved differently

in their investigation. Among other parameters the generalized dimensions D_q, which characterize the fractal behaviour, were determined from $< G_q >$ values following the relation $D_q = \tau_q/(q-1)$. It was observed that the D_q values decreased with increasing q and was always less than unity. According to the authors this decreasing trend of D_q indicated multifractality and gave an evidence for the self-similar cascade mechanism in multiparticle production. The measured value of $D_0 = 1$ for different targets implied that there was practically little contribution of empty bins to the analysis.

1.7.5 Takagi's Multifractal Moments

Due to the finiteness in charged particle multiplicity (n_s) of an event, the mathematical limit of phase-space partition number ($M \rightarrow \infty$) can not be realized in practice. Even the step function Θ introduced into the definition of the G_q moments, can not completely remove the saturation effects, particularly at higher $|q|$ values as has already been observed. In an alternative approach, Takagi [85] has suggested a new set of multiplicity moments for $q > 0$ as,

$$T_q(\delta X_\eta) = \ln \sum_{i=1}^{N_{ev}} \sum_{j=1}^{M} (p_{ij})^q, \tag{1.9}$$

that are not affected by the finiteness of n_s. Here, $p_{ij}(= n_{ij}/K)$ is the normalized density function, K is the total number of particles produced in N_{ev} interactions and n_{ij} is same as Eq. (1.8), when the entire η-space has been divided into M intervals. From the theory of multifractals, $T_q(\delta X_\eta)$ should be a linear function of the logarithm of the resolution $R(\delta X_\eta)$,

$$T_q(\delta X_\eta) = A_q + B_q \ln R(\delta X_\eta), \tag{1.10}$$

where A_q and B_q are constants independent of q. When a linear dependence is observed over a large range of $R(\delta X_\eta)$, following Takagi's method the generalized dimensions can once again be calculated.

Experimental Results On Takagi's Multifractal Moments

Recently Bershadskii suggested that the Bernoulli distribution appears in a natural way when transition from monofractality to multifractality is studied. The following relation for the multifractal Bernoulli function derived by Bershadskii [86] is given by,

$$D_q = D_\infty + C \ln q/(q-1)$$

where D_q is the generalized dimension of order q and C is a constant. The monofractality to multifractality phase transition corresponds to a gap $C = 0$ to finite nonzero value of C. He also determined the generalized dimensions spectra for ^{32}S-Em interactions at 200 A GeV/c, ^{12}C-Em interactions at 4.5 A GeV and ^{16}O-Em interactions at 60 A GeV [87] and finally obtained a universal value of multifractal specific heat $C \approx 0.25$.

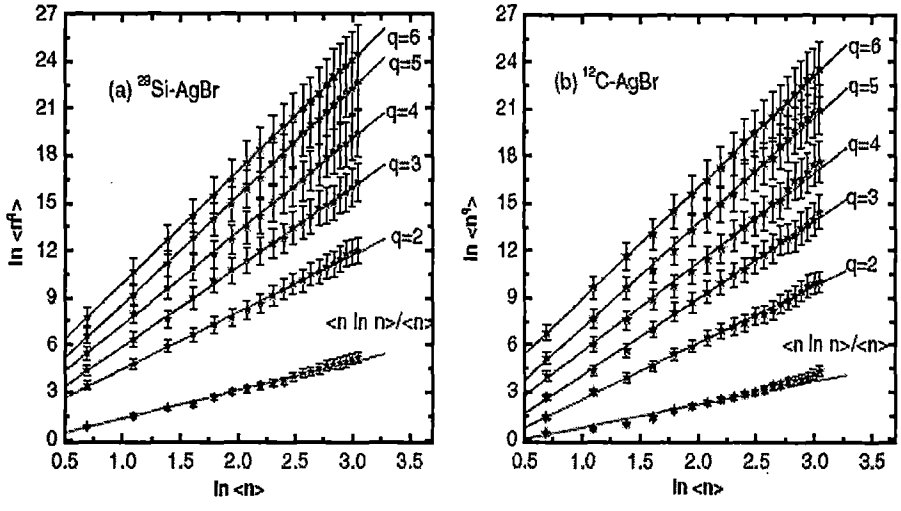

Figure 1.25: Plot of Takagi's multifractal moments in ^{12}C-Em and ^{28}Si-Em collisions at 4.5 A GeV/c [84].

Ahmad et al. [84] applied the Takagi methodology to study the multifractal behaviour of produced particle in ^{12}C-Em and ^{28}Si-Em collisions at 4.5 A GeV/c. Their analysis was confined to the central region ($\eta_{peak} - 1.5 < \eta < \eta_{peak} + 1.5$), which covers most of the produced particles. The values of $< n \ln n > / < n >$ and $< n^q >$ are calculated for each interval. The values of $\ln < n^q >$ as a function of $ln < n >$ for different q were plotted for ^{12}C-Em and ^{28}Si-Em collisions and observed that all points clearly follow an excellent linear relation for the whole range of $< n >$. The linear behaviour of $\ln < n^q >$ with $\ln < n >$ in their analysis gives an indication of the fractal structure in multiparticle production in η-space. The values of the slopes, K_q, for ^{12}C-Em and ^{28}Si-Em collisions were calculated. Using the values of K_q they estimates the generalized dimensions D_q, which characterize the fractal behaviour. The values of the generalized dimensions, D_q, for different values of q obtained from Takagi's moment decrease with the increasing order of the moments,

q, and is always less than 1 for all q. The decreasing trend of D_q with increasing q clearly gives an indication of multifractal characteristics, which supports an interpretation in terms of a cascade mechanism in multiparticle production. they also estimated the value of multifractal specific heat using the relation $D_q = D_\infty + C \ln q/(q-1)$. The observed linear behaviour of D_q with respect to $\ln q/(q-1)$ indicates good agreement between the experimental data and the multifractal Bernoulli representation.

1.7.6 Erraticity

The erraticity moments $C_{p,q}$ first introduced by Cao and Hwa [88], provide a new technique to investigate both the spatial density fluctuations as well as the event-to-event fluctuations. The method is free from some of the limitations of the scaled factorial moments. The moments $C_{p,q}$ are analytically connected with an entropy index μ_q, a parameter suitable for measuring the chaotic behaviour in the QCD branching process. The entropy index describes the degree of fluctuation of the scaled factorial moments in event space as well as the spatial pattern of the distribution of particles in final states. It also characterizes the degree of fluctuation of the parton multiplicity that initiates the QCD branching. The index μ_q has an added advantage in the sense that it can distinguish a branching process initiated by a quark from that initiated by a gluon. The erraticity moments $C_{p,q}$ is defined as the vertically averaged p-th order moments of the normalized qth order factorial moments i.e.,

$$C_{p,q} = < \phi_q^p >_v,$$

where,

$$< \phi_q^p > = \frac{F_q^e}{< F_q^e >_v},$$

and F_q^e is taken as the horizontally averaged factorial moment for a single event. It should be noted that unlike q, which is always a positive integer, p can be any positive number. If a power law dependence of $C_{p,q}$ on M

$$C_{p,q} \propto M^{\psi_q(p)}$$

is observed, the phenomenon is referred to as erraticity of nonstatistical fluctuation. The exponent $\psi_q(p)$ is called the erraticity index. The slope $\mu_q = \frac{d}{dp}\psi_q(p)|_{p=1}$ termed as the entropy index, is an efficient parameter to characterize erraticity. For low multiplicity

hh, hA events the erraticity analysis of gap distribution have also been proposed. In this regard till date very little result exist in the literature.

Experimental Results On Erraticity

Shaoshun and Zhaomin [89] measured the entropy index μ_q for different values of q in case of multiparticle production in pp collisions at 400 GeV/c. Due to nonflatness of the single particle density distribution they used the cumulant variable $\chi(\eta)$ where in $\chi(\eta)$ space the single particle density is uniformly distributed from 0 to 1. They divided the total sample region into M bins and calculate the moments $C_{p,q}(M)$ for $q = 2, 3, 4$, and $p = 0.5 - 2.0$, and $M = 1, 2, \cdots 40$, respectively. The linear fit is performed in a preferred region $M = 5 - 25$ and they estimate the values of μ_q for different values of q. They also compared the values of μ_q with that obtained from Monte Carlo - simulated values of a quark jet and a gluon jet separately at a fixed coupling constant $\alpha_s = 0.05$. It is found that the values of the entropy indexes are quite large and very close to the Monte Carlo simulated values of a quark jet at a fixed coupling constant $\alpha_s = 0.05$. However it is significantly greater than the simulated values of a gluon jet at the same coupling constant $\alpha_s = 0.05$. From the result one may assume that the original parton that initiates the parton shower in 400 GeV/c pp collision is a quark. They also calculated the entropy indexes for for different multiplicity region. They found that with increasing average multiplicity the entropy indexes decrease. The experimental results agree with the theoretical predictions. But the experimental results are still significantly larger than the corresponding simulated values based on the assumption of gluon jets. Hence, the reaction may not be dominated by QCD parton showering.

Hasan et al. [91] have studied the fluctuations in the special pattern of the final states of Si-Ag/Br collisions at 14.6A GeV/c by measuring the entropy indexes, as compared to the values from generated uncorrelated events which are also higher in magnitude. Ahmad et al. [92] examined event-by-event fluctuations in factorial moments in terms of erraticity measures are by analysing the experimental data on 4.5A and 14.5A GeV/c ^{28}Si-emulsion interactions. The findings are compared with the predictions of Lund Monte Carlo model, FRITIOF [64]. Values of $C_{p,q}$ moments are calculated for $p = 0.5 - 2.0$, $q = 2, 3, 4$ and $M = 2^k$ where $k = 0, 1, 2, \cdots$. The variation of $\ln C_{p,q}$ with $\ln M$ and dependence of Σ_q on $\ln M$ for the experimental data at the two incident energies are studied. It is seen that the

log-log plots of $C_{p,q}$ against M have similar shapes for two data sets under consideration. Trends of the variation of Σ_q with $\ln M$ are also found to be similar for the two data sets.

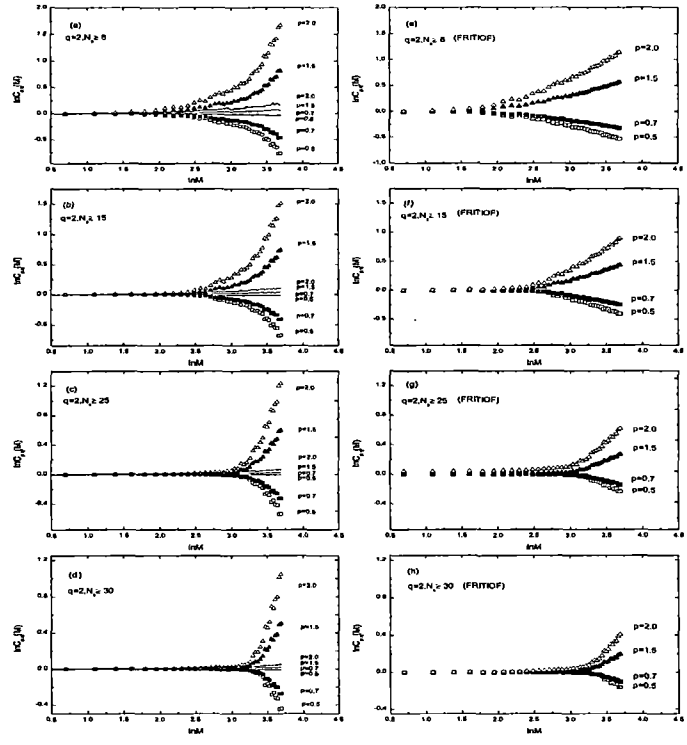

Figure 1.26: Results from erraticity analysis on shower track emission data from ^{28}Si-emulsion interaction at 14.6A GeV/c, along with corresponding FRITIOF prediction.

This, therefore, indicates that erraticity exists in all the cases but with different strength and is, therefore, characterized by different values of entropy index μ_q. As suggested in [89] the value of the entropy index μ_q is evaluated. For investigating the effect of multiplicity n_s on erraticity, $\ln C_{p,q}$ and μ_q are calculated by grouping the interactions on the basis of their n_s values. It is noted that μ_q decreases with increasing $\sqrt{n_s}$ irrespective of the beam energy. This is expected because the fluctuations in the event factorial moments would increase with decreasing particle multiplicity. Furthermore, all the analysis were compared with FRITIOF generated data and noticed that all behaviour are essentially similar. These results, therefore, suggest that the erraticity behaviour observed in Si-emulsion collisions at 4.5 A and 14.5 A GeV/c are in excellent agreement with the corresponding values predicted by the Lund FRITIOF model. A comparison of the results

of the present study with those reported by other workers [93] suggests that the erratic fluctuations observed are rather due to the statistical reasons and there is no unambiguous evidence for the occurrence of dynamical fluctuations. These negative findings provide a positive indication that this approach would be sensitive in extracting the dynamical fluctuations arising due to some new kind of physical phenomena expected in heavy-ion experiments at higher energies with events of higher multiplicities.

Recently the chaotic behaviour of the multiparticle production in high-energy AB collision has been investigated with the help of erraticity analysis using the data of ^{32}S-Ag/Br interaction at 200A GeV/c by Ghosh et al. [90]. They measured the entropy index μ_q in η space for experimental data as well as for randomly generated data in two different process - one from the $C_{p,q}$ moments, and another from the $\Sigma_q =< \phi_q(M) \ln \phi_q(M) >$ moments. They also compared their results with the results obtained by Wang et al. [94] for pp collision at 400 GeV/c. Their values of entropy index from $C_{p,q}$ moments are greater for p-p collisions at 400 GeV/c than the ^{32}S-Ag/Br interaction at 200A GeV/c. The same trend is also followed by the entropy index obtained from Σ_q moments. They also reported that the entropy indexes are large signifying chaotic behaviour of the multipion production process in ultra relativistic nuclear interactions. The observed higher value of entropy index for experimental data compare to random data indicates true signals of chaos without any bias of statistical fluctuation. Moreover, it has been also observed that the VENUS [71] model is unable to reproduce such chaotic multiparticle production in ^{32}S-Ag/Br interactions at 200A GeV/c. They also studied the multiplicity dependence of the chaotic behaviour, and found that the chaoticity increased with increasing $< n_s >$. They also performed a 2-d erraticity analysis, and found that μ_q in 2-d is almost double of the corresponding 1-d value. They concluded that the 1-d analysis underestimates the fluctuations of spatial patterns, implying the importance of higher dimensional analysis.

1.8 Models of AB interaction

To describe a high-energy heavy-ion interaction many physical mechanisms have to be taken into account. Due to the intrinsic complexities associated with the QCD, nonperturbative effects are to be treated through model calculations. Unfortunately, so far we

do not have any standardized method for the purpose, that describes all stages of space-time evolution process in an AB interaction. A broad classification of the models can however, be made in terms of the emphasis given to a particular stage of the evolution. The hadronic models based on simple superposition of elementary NN interactions, try to simulate the entire history of the space-time evolution. Any deviation from the prediction of a hadronic model should therefore, be interpreted as a collective effect. Models based on parton shower cascade and/or string fragmentation mechanism(s) put emphasis on the initial pre-equilibrium stage of the interaction, where no subsequent equilibration is assumed. Hydrodynamical and/or statistical models on the other hand, mainly describe the thermal/chemical equilibrium stage, a prerequisite for QGP formation. The calculations can however, be extended also to the final freeze out stage. In the following we have briefly reviewed some of the models used to simulate AB interactions at high-energy. As will be seen, the boundary between two different categories is not always very distinct, and often there are cross-overs into each other's domain.

1.8.1 LEXUS

The Linear Extrapolation of Ultrarelativistic Scattering or the LEXUS model [95] belongs to the first category of hadronic models. The extrapolation is based on Glauber's formulation [22], where an AB interaction is looked upon as a superposition of many independent NN interactions in free space. In addition LEXUS also considers that, a collision at an impact parameter b is a sum of independent collisions between rows of nucleons belonging to the colliding nuclei. Two rows collide when the transverse position of the projectile row $w.r.t$ the projectile center of mass, and that of the target row $w.r.t$ the target center of mass are separated by b. The average number of nucleons in a row at a transverse position $\mathbf{s}$ is obtained from the NN cross section σ_{NN} as,

$$\nu_i = \sigma_{NN} \int dz \rho_i(\mathbf{s}, z) : \quad i = A,\ B$$

where z is the longitudinal coordinate, and ρ is the baryon density for which a Woods-Saxon type of distribution is used for heavy nuclei, whereas a three parameter Gaussian for light nuclei. Fluctuations in these numbers as well as fluctuations in the number of collisions suffered by any given nucleon in a row are taken into account. The probability

to have exactly m nucleons in a row is obtained by using a binomial distribution with a cut in the upper limit ($\sim$ 10 nucleons). Making use of a geometrical overlap function $f(\mathbf{b}) = \int \sigma_{NN}^{-1}\, d^2s_A\, \nu_A(\mathbf{s}_A)\nu_B(\mathbf{s}_B)$, the total AB cross section σ_{AB}^{tot} is computed as,

$$\sigma_{AB}^{tot} = \int d^2b\,\{1 - \exp\,[-f(\mathbf{b})]\}.$$

LEXUS could well describe global distributions like y and p_t of baryons and y, p_t and multiplicity of $(-)$ve hadrons at SPS energies. QGP probe like strange particle abundance is not reproduced so well by LEXUS. The treatment can be improved by taking into account the elastic and diffractive dissociation components of NN collision.

1.8.2 Lund Model - Fritiof

During the BNL-AGS and CERN-SPS era, the Lund Monte Carlo Model [96] has been one of the most popular models for AB collisions at high-energy. The computer code FRITIOF [64, 70] is the implementation of the Lund Model. Since the inception of its earliest version 1.6, the code has been modified a number of times, the latest being version 7.0. The model is an extension of the old multiperipheral model and it belongs to the category of string fragmentation, where an AB collision is considered as a superposition of many NN interactions. The model is meant for soft (low p_t) interactions, as bulk of the particles come out with small p_t values. It is assumed that the particle production via hadronic interaction is a two step process - (i) two interacting hadrons are first excited through soft gluon exchange, and (ii) constituents (valence quarks) of the excited hadrons exchange a string of quarks and anti-quarks, from which more hadrons are produced. A string is excited only between the constituents of the same hadron, and there is no net colour exchange between two interacting hadrons. The interacting hadrons (nucleons for AB collision) are assumed to be stretchable only in the longitudinal direction, and they are not excited transversely. The decay of the stretched hadrons may be analyzed in the same way as the fragmentation of a string stretched between a $q\bar{q}$ pair. Representing the energy-momentum of a hadron by its light-cone momenta it can be assumed that, collisions between the hadrons will lead to a flow of their light-cone momenta from one hadron to the other. After each collision a projectile hadron having forward light cone momentum b_+ will transfer an amount Q_+ to one target hadron, and in return the target hadron transfers an

amount Q_- of its backward light-cone momentum a_- to the projectile hadron. Following Feynman's wee parton spectrum the momentum transfer obeys a probability distribution,

$$d^2P \propto \frac{dQ_+}{(Q_+ + \frac{m_b^2}{b_+})} \frac{dQ_-}{(Q_- + \frac{m_a^2}{a_-})}$$

where the mass terms come from the lower limits of the momentum transfer.

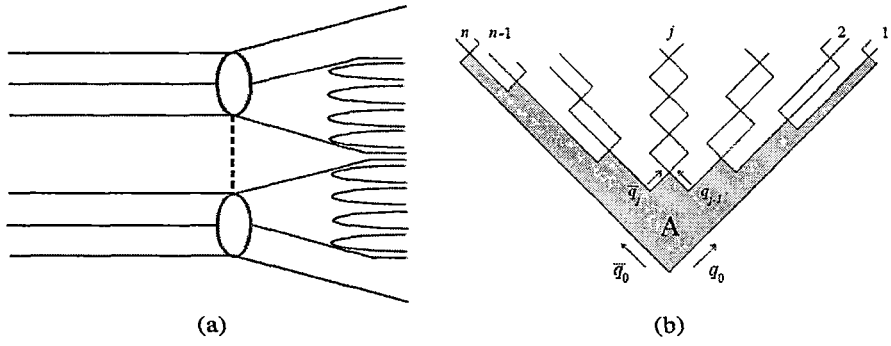

(a) (b)

Figure 1.27: The LUND string formation and fragmentation scheme. In (a) note the string being excited between partons of the same hadron. In (b) the space-time trajectories of q and $\bar{q}$ from a string fragmentation have been shown.

For AB collisions a generalization of the above idea is made. An AB interaction is considered as an incoherent combination of a set of many elementary collisions of nucleons of one nucleus with those belonging to the other. A straight line geometry is assumed between the projectile and target nuclei. An incident nucleon impinge upon target nucleons with randomly distributed impact parameter b, which is restricted by a nonzero minimum allowable value. For each NN interaction a Gaussian type of overlapping function $G(b)$ is used. Due to time dilation, fragmentation of an interacting nucleon into any intermediate state, and hence possibility of any intra nuclear cascade is ruled out. Thus a projectile nucleon interacting with ν nucleons inside a target nucleus, will form $\nu+1$ excited strings. These strings undergo bremsstrahlung radiation, and subsequently fragment into hadrons. The nucleons inside a nucleus (for $A > 16$) follow a Wood-Saxon type of distribution,

$$\rho(\vec{r}) = \frac{\rho_0}{1 + \exp\left(\frac{r - r_0 A^{1/3}}{C_d}\right)}.$$

The radius parameter r_0 has a small A dependence, C_d is the diffuseness parameter, and ρ_0 is a normalization constant. The Lund model has been successful in describing

several global characteristics of multiparticle final states of AB collision at AGS and SPS energies. However, as we shall later see, it fails to account for the small scale structure of phase-space distribution of produced hadrons. On different occasions the prediction of FRITIOF has been compared to our experimental results on ^{32}S induced interactions at 200A GeV/c.

1.8.3 Dual Parton Model

Like the Lund Model (FRITIOF), the Dual Parton Model (DPM) [97] is basically another string fragmentation model. The mechanism of particle production once again is based on the excitation of strings, and their subsequent fragmentation into final state hadrons.In DPM concepts like the Reggeon and the Pomeron are used. The main contribution to hadron production comes from two string events, and in principle multistrings are also feasible. Whereas, in the Lund Model only one string is formed. Moreover, in DPM a string is excited only between the constituents of two different (colliding) hadrons, and therefore, a colour exchange takes place. In this model, a nucleon is considered as composed of a quark and a diquark system. Except that the diquark cannot be annihilated by a quark, the former behaves like an antiquark ! The momentum fraction x_q of a valence quark in a nucleon follows a Field Feynman type of distribution [98],

$$\rho(x_q) \propto x_q^{-1/2}(1-x_q)^{1.5},$$

whereas that ($x_{qq} = 1 - x_q$) of the diquark system follows,

$$\rho(x_{qq}) \propto (1-x_{qq})^{-1/2} x_{qq}^{1.5}.$$

An AB collision can be decomposed into a Glauber type of many incoherent NN interactions [22]. A pair of chains (like strings in Lund model) are formed when a valence quark of the incident nucleon interacts with the diquark of the target nucleon, and vice versa. In a second collision the projectile diquark form a chain with the valence quark of the second nucleon, and another chain is formed between one projectile sea quark and the diquark of second target nucleon. Thus the projectile nucleon undergoes n Pomeron exchange in collision with n target nucleons. Each chain gives rise to an independent production of particle. The computer code VENUS [71] based on DPM includes the additional prob-

ability of finding out an antiquark, and its contribution to Pomeron exchange. VENUS made use of deep inelastic experimental data for the momentum distribution of partons.

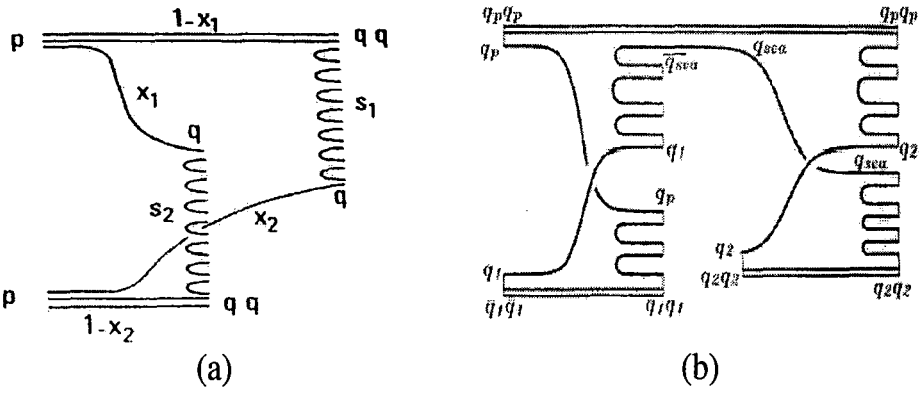

Figure 1.28: String fragmentation in DPM - (a) string formed between a valence quark of the incident nucleon and a diquark of the target nucleon; (b) projectile diquark forms a chain with a sea quark of 2nd target nucleon.

1.8.4 HIJING

The Heavy-Ion Jet Interaction Generator (HIJING) is another Monte Carlo event generator developed for pp, pA, and AB collisions [99]. Salient features of the model can be described in the following manner. HIJING treats an AB collision as a superposition of many binary NN collisions. The impact parameter of each NN interaction is determined by the transverse position of each nucleon generated by the Woods-Saxon density distribution. Diffuse nuclear geometry is used to calculate the impact parameter dependence of the number of inelastic processes. In this scheme multiple soft beam jets are modeled by diquark-quark string excitation and fragmentation along the lines of Lund FRITIOF and DPM. In the HIJING model a diquark is treated as a single entity, and this leads to an average rapidity shift of about one unit in the net baryon distribution. In addition, HIJING also incorporates perturbative QCD adopted in the PYTHIA model of hh interactions [100], and is therefore, capable of describing both soft and hard ($p_t > 2$ GeV/c) components of particle production. Hence unlike the Lund model and DPM, HIJING works at the RHIC energy and is expected to work also at the LHC energy. Nuclear

effects like jet quenching and parton shadowing have also been incorporated into this model. A QGP probe like the jet quenching is included to study the dependence of moderate and high p_t observables on an assumed energy loss dE/dx of partons traversing the produced dense matter. Mini jets from produced partons are quenched by losing energy to the wounded nucleons close to their straight line trajectories. An impact parameter dependent parton structure function is introduced to study the sensitivity of observables to nuclear shadowing, especially of the gluon structure functions. To generate the initial phase-space distribution for the parton cascade, the formation time for each parton is determined according to a Lorentzian distribution with a half width $t_f = E/{m_t}^2$, where E and m_t are the parton energy and transverse mass, respectively. Positions of formed partons are calculated from those of their parent nucleons using straight line trajectories. During the time of formation, partons are considered to be part of the coherent cloud of parent nucleons, and they thus do not suffer rescattering. Once the partons stop interacting, after an additional proper time of about 1.2 fm, they are converted into hadrons according to the HIJING fragmentation scheme.

1.8.5 UrQMD

High-energy nuclear collisions are also investigated in the Ultrarelativistic - Quantum - Molecular - Dynamics (UrQMD) approach [101]. Basically the UrQMD model is a convolution of two different schemes. On one hand, it is a microscopic transport theory of covariant propagation of all hadrons along their classical trajectories, combined with stochastic binary scattering, resonance decay and colour string formation. For this purpose a relativistic Boltzmann equation has to be solved for hadrons in the final stage of the collision. On the other, the model also considers a hydrodynamical evolution of all stages of interaction, formation of a QGP like state, and for that to happen a local thermodynamical equilibrium at the partonic level has to be assumed. The basic input to hadronic transport models is that, a hh interaction would occur if $b < \sqrt{\sigma_{tot}/\pi}$, where total cross-section σ_{tot} depends on isospin of interacting hadrons, their flavour and *cms* energy. Partial corss-sections are also used to compute the relative weights of different channels. The Fermi gas model is utilized to describe the projectile and target nuclei, the initial momentum of each nucleon being randomly distributed between 0 and the

local Thomas-Fermi momentum. Each nucleon is described by a Gaussian shaped density distribution, and the wave function for the nucleus is taken as a product of single nucleon Gaussian functions. In configuration space the centroids of Gaussian are randomly distributed within a sphere, and finite widths of the Gaussian result in a diffused surface region. At low and intermediate energies ($\sqrt{s} < 5$ GeV) the phenomenology of hadronic interactions is described in terms of interactions between known hadrons and their resonances. At higher energies, $\sqrt{s} > 5$ GeV, the excitation of colour strings and their subsequent fragmentation into hadrons dominates the multiple production of particles in the UrQMD model. For AB collisions the soft binary and ternary interactions between nucleons are described by a non-relativistic density-dependent Skyrme potential. In addition, Yukawa, Coulomb and Pauli (optional) potentials are implemented in the model. The potentials allow to calculate the equation of state of the interacting many body system, as long as it is dominated by nucleons. Note that these potential interactions are only used in the model for baryons/nucleons with relative momenta Δp of less than 2 GeV/c. The model should allow for subsequent rescatterings. The collision term in the UrQMD model includes more than fifty baryon species and five meson nonets (45 mesons). This framework allows to bridge with one concise model the entire available range of energies from the Bevalac energy region ($\sqrt{s_{NN}} \sim$ a few GeV) to the RHIC energy ($\sqrt{s_{NN}} = 200$ GeV).

Bibliography

[1] A comprehensive review of the AGS, SPS era experiments, and an excellent textbook on the subject has been written by C. Y. Wong, *Introduction to high-energy heavy-ion collisions* (World Scientifc, Singapore, 1994).

[2] *Quark matter formation and heavy-ion collisions, Proceedings of Bielefeld Workshop*, ed. M. Jacob and H. Satz (World Scientific, Singapore 1982).

[3] W. Busza and A. Goldhaber, *Phys. Lett.* **B 139,** 235 (1984).

[4] G. D. Westfall *et al.*, *Phys. Rev. Lett.* **37,** 1202 (1976).

[5] T. D. Lee, *Rev. Mod. Phys.* **47,** 267 (1975).

[6] E. Shuryak, *Phys. Rep.* **61,** 71 (1979).

[7] G. Bertsch and J. Cugnon, *Phys. Rev.* **C 24,** 2514 (1981).

[8] Many aspects of QGP and a review of SPS and RHIC experiments can be found in K. Yagi, T. Hatsuda and Y. Make, *Quark-Gluon Plasma* (Cambridge University Press, New York, 2005).

[9] A. Chodos, R. L. Jaffe, K. Johnson, C. B. Thorn and V. F. Weisskopf, *Phys. Rev.* **D 9,** 3471 (1974)
L. Wilets, *Bag Model of Nucleus* (World Scientifc, Singapore, 1989).

[10] Several basic features of high-energy interaction have been lucidly explained by R. A. Salmeron, *Quark-Gluon Plasma,* ed. B. Sinha, S. Paul. and S. Raha (Springer-Verlag, Berlin, 1990).

[11] I. Otterlund, *Central Heavy-ion Interaction at 15 and 200 GeV - A Comparison: Cosmic and Subatomic Physics Report,* **LUIP 9012,** *Invited talk at the International High-density Nuclear Matter* (1990).

[12] B. Andersson *et al.*, *Phys. Scr.* **34,** 451 (1986).

[13] Y. Nambu, *Phys. Rev. Lett.* **4,** 380 (1960)
Y. Nambu and G. Jona-Lasinio, *Phys. Rev.* **122,** 345 (1961).

[14] R. Anishetty, P. Koehler and L. McLerran *Phys. Rev.* **D 22,** 2793 (1980).

[15] G. Baym and S. A. Chin, *Phys. Lett.* **B 62,** 241 (1976)
H. Satz, *Ann. Rev. Nucl. Part. Sci.* **35,** 245 (1985)
H. Satz *et al.*, *Z. Phys.* **C 38,** 1 (1988).

[16] S. Z. Belenski and L. D. Landau, *Ups. Fiz. Nauk.* **56,** 309 (1955); *Nuov. Cim. Suppl. II* **3,** 15 (1956).

[17] J. D. Bjorken, *Phys. Rev.* **D 27,** 140 (1983).

[18] Review of experiments in AGS and SPS era on high-energy heavy-ion collisions can be found in, I. Otterlund, *Ultrarelativistic Nucleus-Nucleus Collisions,* Lectures given at 3rd Hellenic School on Elementary Particle Physics, (Corfu, Greece, 1989).
Physics and Astrophysics of Quark-Gluon Plasma, ed. B. Sinha, D. K. Srivastava and Y. P. Viyogi, (Narosa, New Delhi, 1998).

[19] P. V. Ruuskanen, *Nucl. Phys.* **A 522,** 255c (1991); *Nucl. Phys.* **A 544,** 169c (1992).

[20] K. Kajantie, J. Kapusta, L. McLerran and A. Mekjian, *Phys. Rev.* **D 34,** 2746 (1986).

[21] S. D. Drell and T. M. Yan, *Phys. Rev. Lett.* **25,** 316 (1970).

[22] R. J. Galuber, *Lectures on Theoretical Physics,* vol.I, (Interscience, New York, 1959).

[23] CERES/NA45 Collaboration, G. Agakichiev *et al.*, *Phys. Rev. Lett.* **75,** 1272 (1995); *Nucl. Phys.* **A 610,** 317c (1996); *Phys. Lett* **B 422,** 405 (1998)
B. Lenkeit *et al.*, *Nucl. Phys.* **A 661,** 23c (1999).

[24] NA38 Collaboration, M. C. Abreu *et al.*, *Nucl. Phys.* **A 566,** 77c (1994).

[25] NA50 Collaboration, M. C. Abreu *et al.*, *Nucl. Phys.* **A 610,** 404c (1996); *Phys. Lett* **B 450,** 456 (1999); *Phys. Lett* **B 477,** 28 (2000).

[26] E. V. Shuryak, *Sov. J. Nucl. Phys.* **28,** 408 (1978)
R. C. Hwa and K. Kajantie, *Phys. Rev.* **D 32,** 1109 (1985)
S. Raha and B.Sinha, *Phys. Rev. Lett.* **58,** 101 (1987)
J. Kapusta, P. Lichard and D. Siebert, *Phys. Rev.* **D 44,** 2744 (1991)
J. Alam, D. K. Srivastava, B. Sinha and D. N. Basu, *Phys. Rev.* **D 48,** 1117 (1993).

[27] J. Kapusta, P. Lichard and D. Siebert, *Nucl. Phys.* **A 544,** 485c (1992).

[28] HELIOS/NA34 Collaboration, T. Akesson *et al.*, *Z. Phys.* **C 46,** 369 (1990).

[29] WA80 Collaboration, R. Albrecht *et al.*, *Z. Phys.* **C 51,** 1 (1991); *Phys. Rev.* **C 44,** 2736 (1991); *Nucl. Phys.* **A 566,** 61c (1994); *Phys. Rev. Lett.* **76,** 3506 (1996).

[30] WA98 Collaboration, M. M. Aggarwal *et al.*, *Phys. Rev. Lett.* **83,** 926 (1999); *Phys. Rev. Lett.* **85,** 3595 (2000).

[31] PHENIX Collaboration, S. S. Adler *et al.*, *Phys. Rev. Lett.* **94,** 232301 (2005).

[32] T. Matsui and H. Satz, *Phys. Lett.* **B 178,** 416 (1986)
T. Matsui, *Z. Phys.* **C 38,** 245 (1988).

[33] NA38 Collaboration, C. Baglin *et al.*, *Phys. Lett.* **B 255,** 459 (1991); *Phys. Lett.* **B 345,** 617 (1995).
NA51 Collaboration, A. Baldit *et al.*, *Phys. Lett.* **B 332,** 244 (1994).

[34] NA38 Collaboration, C. Baglin *et al.*, *Phys. Lett.* **B 262,** 362 (1991).

[35] G. Goldhaber, S. Goldhaber, W. Lee and A. Pais *Phys. Rev.* **120,** 300 (1960).

[36] R. Hanbury-Brown and R. Q. Twiss, *Phil. Mag.* **45,** 663 (1954); *Nature* **178,** 1046 (1956).

[37] G. Cocconi, *Phys. Lett.* **B 49,** 459 (1974).

[38] NA35 Collaboration, A. Bamberger *et al.*, *Phys. Lett.* **B 203,** 320 (1988); *Nucl. Phys.* **A 498,** 133c (1989).
WA80 Collaboration T. Peitzmann *et al.*, *Nucl. Phys.* **A 498,** 397c (1989).

[39] NA35 Collaboration, T. Alber *et al.*, *Nucl. Phys.* **A 590,** 453c (1995).
NA49 Collaboration, H. Appelshauser *et al.*, *Eur. Phys. J.* **C 2,** 661 (1998).

[40] STAR Collaboration, C. Adler *et al.*, *Phys. Rev. Lett.* **87,** 082301, (2001).
STAR Collaboration, J. Adams *et al.*, *Phys. Rev. Lett.* **93,** 012301, (2004).
PHENIX Cpllaboration, S. S. Adler *et al.*, *Phys. Rev. Lett.* **93,** 152302, (2004).

[41] J. Rafelski and B. Muller, *Phys. Rev. Lett.* **48,** 1066 (1982)
P. Koch, B. Muller and J. Rafelski, J. Rafelski, *Phys. Rep.* **142,** 167 (1986); *Phys. Rep.* **88,** 331 (1988); *Nucl. Phys.* **A 544,** 279c(1992).

[42] E802 Collaboration, T. Abbott *et al.*, *Phys. Rev. Lett.* **64,** 847 (1990)
L. Ahle *et al.*, *Phys. Rev.* **C 60,** 044904 (1999).

[43] E868 Collaboration, T. Amstrong *et al.*, *Phys. Rev.* **C 59,** 2699 (1999).
E878 Collaboration, M. Bennett *et al.*, *Phys. Rev.* **C 56,** 1521 (1997).

[44] E917 Collaboration, B. B. Back *et al.*, *Phys. Rev. Lett.* **87,** 242301 (2001).

[45] WA97/NA57 Collaboration, F. Antinori *et al.*, *J. Phys.* **G 28,** 1607 (2002).

[46] STAR Collaboration, C. Adler *et al.*, *Phys. Rev. Lett.* **89,** 092301 (2002).

[47] A. M. Poskanzer and S. A. Voloshin, *Phys. Rev.* **C 58,** 1671 (1998); textitPhys. Lett. **B 474,** 27 (2000).

[48] STAR Collaboration, J. Adams *et al.*, *Phys. Rev. Lett.* **92,** 052302 (2004).

[49] PHENIX Collaboration, S. S. Adler *et al.*, *Phys. Rev. Lett.* **91,** 182301, (2003).

[50] NA49 Collaboration, A. M. Poskanzer *et al.*, *Nucl. Phys.* **A 661,** 341c (1999).

[51] CERES Collaboration, J. Milosevic *et al.*, *J. Phys.* **G 32,** S97 (2006).

[52] S. Jeon and V. Koch, *Phys. Rev. Lett.* **85,** 2076, (2000).

[53] STAR Collaboration, G. D. Westfall *et al.*, *J. Phys.* **G 30,** S1389 (2004).
STAR Collaboration, J. Adams *et al.*, *Phys. Rev.* **C 68,** 044905 (2003).

[54] PHENIX Collaboration, K. Adcox *et al.*, *Phys. Rev. Lett* **89,** 082301 (2002).

[55] JACEE Collaboration, T. H. Burnett *et al.*, *Phys. Rev. Lett.* **50,** 2062 (1983).

[56] A. Bialas and R. Peschanski, *Nucl. Phys.* **B 273,** 703 (1986); *Nucl. Phys.* **B 308,** 857 (1988).

[57] T. Ludlam and R. Slansky, *Phys. Rev.* **D 8,** 1408 (1973).

[58] NA22 Collaboration, M. Adamus *et al.*, *Phys. Lett.* **B 185,** 200 (1987).

[59] UA5 Collaboration, G. J. Alner *et al.*, *Phys. Rep.* **154,** 247 (1987).

[60] An excellent review on dynamical fluctuation and scaling laws can be found in E. A. De Wolf, I. M. Dremin and W. Kittel, *Phys. Rep.* **270,** 1 (1996)
W. Kittel and E. A, De Wolf, *Soft Multihadron Dynamics* (World Scientific, Singapore, 2005).

[61] KLM Collaboration, R. Holynski *et al.*, *Phys. Rev. Lett.* **62,** 733 (1989); *Phys. Rev.* **C 40,** R2449 (1989).

[62] EMU01 Collaboration, M. I. Adamovich *et al.*, *Phys. Rev. Lett.* **65,** 412 (1990).

[63] EMU01 Collaboration, M. I. Adamovich *et al.*, *Nucl. Phys.* **B 388,** 3 (1992).

[64] B Nilsson-Almqvist and E. Stenlund, *Comp. Phys. Comm.* **43,** 387 (1987).

[65] D. Seibert, *Phys. Rev.* **D 41,** 3381 (1990).

[66] WA80 Collaboration, R. Albrecht *et al.*, *Phys. Lett.* **B 221,** 427 (1989)
C. R. Young *et al.*, *Nucl. Phys.* **A 498,** 53c (1989).

[67] E. K. Sarkisyan and G. G. Taran, *Phys. Lett.* **B 279,** 177 (1992)
E. K. Sarkisyan, L. K. Gelovani, G. L. Gogiberidze and G. G. Taran, *Phys. Lett.* **B 347,** 439 (1995).

[68] A. M. Tawfik, *J. Phys.* **G 27,** 2283 (2001).

[69] A. M. Tawfik and G. Ganssauge, arXiv:hep-ph/0012008 v1 (2000).

[70] H. Pi, *Comp. Phys. Comm.* **71,** 173 (1992)
B. Andersson, G. Gustafson and H. Pi, *Z. Phys.* **C 57,** 485 (1993).

[71] K. Werner, *Phys. Rev.* **D 39,** 780 (1989); *Phys. Rep.* **232,** 87 (1993).

[72] H. Sorge, *Phys. Rev.* **C 52,** 3291 (1995).

[73] W. Ochs *Phys. Lett.* **B 247,** 101(1990); *Z. Phys.* **C 50,** 339 (1991).

[74] EMU01 Collaboration, M. I. Adamovich *et al.*, *Z. Phys* **C 76,** 659 (1997).

[75] M. M. Haq, S. Islam and R. Hasan, *J. Phys.* **G 30,** 1959 (2004).

[76] S. Islam and R. Hassan, J. Phys. **G 34,** 779 (2007).

[77] R. Peschanski and J. Seixas Report No. CERN.TH 5903/90 unpublished (1990).

[78] D. Ghosh *et al*, *Phys. Rev.* **C 52,** 2092 (1995).

[79] R. C. Hwa, *Phys. Rev.* **D 41,** 1456 (1990).

[80] W. Florkowski and R. C. Hwa, *Phys. Rev.* **D 43,** 1548 (1991)
C. B. Chiu and R. C. Hwa, *Phys. Rev.* **D 43,** 100 (1991).

[81] P. L. Jain, G. Singh and A. Mukhopadhyay, *Phys. Rev.* **C 46,** 721 (1992).

[82] EMU01 Collaboration, M. I. Adamovich *et al.*, *Europhys. Lett.* **5,** 571 (1998).

[83] E. K. Sarkisyan, L. K. Gelovani, G. G. Taran and G. I. Sakharov *Phys. Lett.* **B 318,** 568 (1993).

[84] S. Ahmad and M. A. Ahmad, *J. Phys.* **G 32,** 1279 (2006).

[85] F. Takagi, *Phys. Rev. Lett.* **72,** 32 (1994).

[86] A. Bershadskii, *Phys. Rev.* **C 59,** 364 (1999).

[87] D. Ghosh *et al*, *Z. Phys.* **C 73,** 269 (1997); *Nuov. Cim.* **A 110,** 1289 (1997); *Europhys. Lett.* **41,** 371 (1998).

[88] Z. Cao and R. C. Hwa, *Phys. Rev. Lett.* **75,** 1268 (1995); *Phys. Rev.* **D 53,** 6608 (1996); *Phys. Rev.* **E 56,** 326 (1997).

[89] W. Shaoshun and W. Zhaomin, *Phys. Rev.* **D 57,** 3036 (1998).

[90] D. Ghosh, A. Deb, M. Mondal and J. Ghosh, *Phys. Lett.* **B 540,** 52 (2002).

[91] R. Hassan *et al*, *J. Phys.* **G 28,** 2939 (2002).

[92] S. Ahmad *et al*, *J. Phys.* **G 30,** 1145 (2004).

[93] J. Fu *et al*, *Phys. Lett.* **B 472,** 161 (2000)
F. Liu *et al*, *Phys. Lett.* **B 516,** 293 (2001)
Z. Yi-Fei *et al*, *Chin. Phys. Lett.* **18,** 1179 (2001).

[94] S. Wang *et al*, *Phys. Lett.* **B 458,** 505 (1999).

[95] S. Jeon and J. Kapusta, *Phys. Rev.* **C 56,** 468 (1997).

[96] B. Andersson, G. Gustafson and B Nilsson-Almqvist, *Nucl. Phys.* **B 281,** 289 (1987).

[97] A. Capella, U. Sukhatame, C-I. Tan and J. Tran Thanh Van, *Phys. Lett.* **B 81,** 68 (1979)
A. Capella, U. Sukhatame and J. Tran Thanh Van, *Z. Phys.* **C 3,** 329 (1980)
A. Capella and J. Tran Thanh Van, *Z. Phys.* **C 10,** 249 (1981).

[98] R. D. Field and R. P. Feynman, *Phys. Rev.* **D 15,** 2590 (1977);
Nucl. Phys. **B 136,** 1 (1978).

[99] X. N. Wang and M. Gyulassy, *Phys. Rev.* **D 50,** 3501 (1991).

[100] T. Sjostrand, *Comp. Phys. Comm.* **82,** 74 (1993).

[101] S. A. Bass, A. Dumitru, M. Bleicher, L. Bravina, E. Zabrodin, E. Stoecker and W. Greiner, *Phys. Rev.* **C 60,** 021902 (1999)
S. A. Bass *et al.*, *Prog. Part. Nucl. Phys.* **41,** 225 (1998).